Anisotropy in Near-Surface Formations and Shear-Wave Birefringence —Its Geotechnical Implications: A VSP Appraisal

Ranajit GHOSE and Masaki OSADA

Abstract

Anisotropy of seismic velocities has drawn the attention of researchers since early times. There are reports of observed seismic anisotropy in various scales in earth materials. However, the interest has significantly been revived in recent years because of the recognition of importance of the phenomenon of shear-wave birefringence or splitting. In a birefringent medium two shear waves traveling along the same path, but with different polarizations, possess different velocities; their polarization and velocities are determined by the local symmetry of the anisotropic medium. Compared to the volume of investigations on shear-wave birefringence carried out by earthquake seismologists and the geophysicists engaged in hydrocarbon exploration, there is very little systematic effort made so far for characterizing shear-wave birefringence in the surface weathering layers, which are of importance to the engineers.

This paper reports the results' of our concerted research on delineation of vertical shear-wave birefringence in shallow surface formations, and assesses its implications for engineering considerations. The focus of our research lies on actual field observation. The basic research strategy involved development of acquisition and processing techniques, carrying out careful field experiments, making interpretations based on correlation with other independent field data, and synthetic computations of seismic wavefield, as well as assessing realistically the effects of any observed birefringence in the engineering fields.

The important outcomes of our research are as follows. The new processing algorithm that we propose here has proved its efficiency on Vertical Seismic Profiling (VSP) data, to evaluate the vertical shear-wave birefringence in the very shallow layers. We present here the datasets and results of 4 different field experiments carried out in widely varying geological settings. Our results strongly suggest that shear waves are significantly affected by the presence of medium anisotropy in very shallow surface layers. When anisotropy is taken care of, the processed seismograms exhibit distinct improvement in shape and consistency. Of the 4 experiments, two (one each in hard, fractured rock and in soft subsoil) have produced very significant results proving anisotropy-induced birefringence or splitting on field shear-wave seismograms. Given our present level of acquisition (including hardware) and processing capabilities, the changes in shear-wave polarization as an expression of changes in the medium's anisotropic symmetry always prove to be a stable observation. In comparison, the corresponding velocity variations are often difficult to notice or to characterize with the required level of confidence, though some statistical trends in their distribution are generally visible. The magnitude of velocity variation, or the birefringence, can be significantly high (20%～25%, or more) at certain shallow depth regions. However, the absolute degree of it is a function of our observability in terms of both acquisition and processing. In a hard rock terrain, one of our datasets exhibits that the medium anisotropy, and hence the shear wavefield, are distinctly influenced by the presence of cracks oriented along the lithologic structures. The crack strike can be correlated to the deduced azimuth of the decoupled shear-waves (specifically the fast-split

shear wave) in scales of even a few meters. In soft subsoils, we detected high magnitudes of vertical shear-wave birefringence and systematic changes in shear-wave polarization directions that are well correlatable to changes in age (between say, alluvium and diluvium sediments), depositional environment, and in-situ stress distribution. Numerical computations of wave propagation in anisotropic media show the plausibility of our field observed birefringence, and relate it to the variation of effective stiffness of the medium with direction. We explain that the observed birefringence, caused by anisotropy in the effective rigidity or the shear modulus of the medium under consideration, can truly be important for the engineers. The impact is appreciable particularly in measuring large-scale mechanical and hydraulic properties, estimating the distribution of cracks and fractures in hard rocks, better estimating the shear-wave velocity structure in order to characterize the near-surface, evaluating the dynamic deformation characteristics of soft soil, anticipating the distribution of anisotropic horizontal stress in ground, and calculating the site response for an impending earthquake, which we discuss.

1 Introduction

From time to time seismology has witnessed a resurgence in interest concerning anisotropy of seismic velocities in earth materials. Velocity anisotropy in minerals and the associated phenomenon of shear-wave birefringence or splitting have been known for quite some time and are well documented (e.g., Waterman and Teutonico, 1957; Verma, 1960; Simmons and Wang, 1971). Exploration geophysicists have also started talking about seismic velocity anisotropy since the 1950s (e.g., White and Sengbush, 1953; Postma, 1955; Helbig, 1956; Jolly, 1956). Hess (1964) was first to discover seismic anisotropy in the oceanic lithosphere. Then in the early 1970s, a number of studies dealing with velocity anisotropy in rocks were reported (e.g., Nur and Simmons, 1969; Christensen and Ramananantoandro, 1971; Gupta, 1973a; Tilmann and Bennet, 1973; Todd et al., 1973; Bonner, 1974), most of which were on low-porosity crystalline igneous rocks and the motivation for many of them was derived from earthquake prediction studies. Then beginning in mid-1980s, the recent years have seen a flowering of unprecedented interest among both earthquake seismologists as well as exploration geophysicists in the observation and interpretation of seismic anisotropy (see for example, Nicolas and Christensen (1987), Leary et al. (1990), and Crampin and Lovell (1991), for reviews).

A primary contribution to this recent upsurge of interest has come from the recognition of the significance and the generality of the occurrence of the phenomenon of shear-wave birefringence. Since shear waves have vector polarization, both their velocity and polarization bear diagnostics of anisotropy; this causes shear waves to be more sensitive to the medium anisotropy than the compressional waves. When a medium is anisotropic, a shear wave propagating through it splits into two differently polarized waves (Crampin, 1978)—one parallel to the local "stiff" direction of the medium (for example, in a vertically cracked medium the "stiff" direction is parallel to the crack strike) and the other parallel to the local "weak" direction of the medium (generally perpendicular to the "stiff" direction, but not always), as illustrated in Figure 1. This is called shear-wave "birefringence" or "splitting", which is close to the concept of partial birefringence or partial double refraction referred in mineralogy and crystallography (Dana and Ford, 1947; Battey, 1972). Minerologists define birefringence as the maximum fractional difference in the speed of light rays through a given mineral specimen (i.e., the difference in refractive indices between 'ordinary' and 'extraordinary' rays, which are the two refracted rays completely polarized along mutually perpendicular planes); but partial birefringence is defined as the effect of birefringence

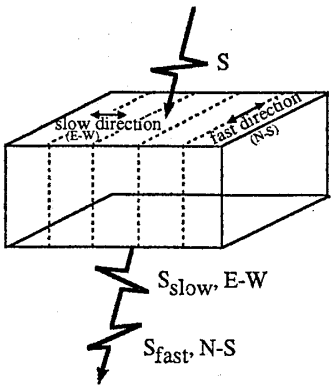

Figure 1. Schematic illustration of shear-wave birefringence or splitting. On incidence upon an anisotropic medium that is characterized by a "stiff" and a "weak" direction of rigidity in the horizontal plane (also called "fast" and "slow" directions, respectively), a vertically propagating shear-wave with any given polarization direction splits into two shear-wave phases that travel with different polarizations and velocities. The polarization directions are functions of the local symmetry of the medium anisotropy, and their velocity difference is proportional to the contrast between maximum and minimum effective rigidities.

observed in an arbitrary direction. The two split modes (S_{fast} and S_{slow} in Figure 1) travel with different velocities through the anisotropic medium. The phase with polarization parallel to the "stiff" direction meets less acoustic impedance and travels faster than the phase with polarization parallel to the "weak" direction. Note that splitting does not occur when the incident shear wave is polarized parallel or perpendicular to the "stiff" direction. Exploration seismologists have been particularly interested in shear-wave birefringence because of its potential to illuminate the symmetry structure of the medium or the reservoir along the raypath, particularly the aligned cracks, fractures and pores that trap circulating fluids and that contain the information of underground stress distribution.

Despite increasing number of reports on the presence of anisotropy and shear-wave birefringence in crust and upper mantle, in hydrocarbon and geothermal reservoirs, and in other exploration targets located in hard rocks at several hundreds of meters of depths, the very shallow near-surface zone, commonly known as weathering zone, has not yet received much attention. By 'near-surface', we mean the underground region up to a depth of several tens of meters that is of interest to the engineers. The lack of concern about anisotropy and shear-wave birefringence in the near-surface formations is primarily because of the lack of commercial prospecting interests at shallow depths, the logistic difficulties associated with the very short propagation distance of the waves through the surface layers, shallow heterogeneities and structural complexities, the limitations in the observable frequency and/or data quality, and the limited understanding of the cause of any observed anisotropy in the near-surface layers, particularly in soft subsoils.

However from civil or geotechnical engineering point of view, the near-surface demands substantial attention. The shear-wave velocity in the near-surface constitutes a basic essential parameter for any engineering consideration. In hard rock areas, the distribution of the microcracks and fractures in very shallow depths is an important consideration for any engineering project. Further, the dynamic elastic moduli of a deformable solid can be computed directly from measurements of compressional and shear velocities and density. Unlike compressional waves, shear waves are insensitive to the fluid content of the subsoil; shear waves, therefore, reflect more faithfully the shear strength of the rock matrix. To an earthquake engineer, the correct estimate of the shear-wave velocity (V_S) of the near-

surface is essential for computing the ground response for an incident earthquake wave. In fact, the seismic basement for an engineering construction is primarily defined by V_S. In soft subsoils, V_S exhibits better correlation with the N-value (that reflects the mechanical strength) than V_P (Imai and Tonouchi, 1982). All these justify the routine determination of the shear-wave velocity structure in all geotechnical surveys.

Vertical shear-wave birefringence, implying the dependence of the velocity of a vertically propagating shear wave on the shear-wave polarization azimuth, can be visualized as a result of azimuthally varying (anisotropic) effective rigidity or shear modulus (μ_e) of the medium ($V_S=\sqrt{\mu_e/\rho}$, ρ is density). In other words, the material is "stiff" or "resistant" to shear stress in one direction in the horizontal plane and "weak" or "pliant" in another direction in the same plane, and this difference in shear strength is sensed by a vertically propagating shear wave, resulting in velocity variation between waves polarized in "stiff" and "weak" directions. Figure 2 illustrates the variation of shear-wave velocity in a constant density medium as a function of effective shear modulus. A difference of 10% in shear-wave velocity means over 20% change in the effective shear modulus, which is very significant to the engineers. One important advantage of the approach of using field observed shear waves to understand the nature of anisotropy of the subsurface is that it can measure the true in-situ properties of the medium.

The motivation of our research, focused on actual field observations in shallow surface formations, derives from the scenario mentioned above. Its goal lies in geotechnical engineering applications. It is possible to summarize the three main objectives of our present research. (1) To make systematic observation (field observation and extraction of information by data processing) of seismic (shear wave) anisotropy in very shallow surface formations possible. This involves overcoming greatly the logistic difficulties in field acquisition of good quality data, by use of improved hardwares and field techniques befitting the scale of engineering prospectings, as well as by developing efficient algorithm to process

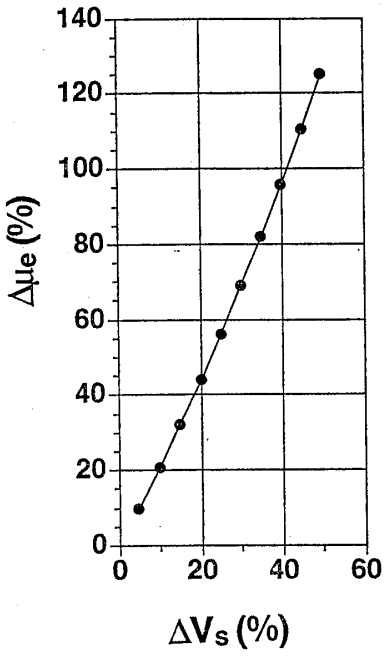

Figure 2. Difference in shear-wave velocity (V_S) as a function of difference in the effective rigidity of the medium. In case of vertical shear-wave birefringence, the velocity difference corresponds to that between the two vertically propagating shear waves with polarization directions parallel to maximum and minimum effective rigidity in the horizontal plane.

systematically the field-observed shear-wave seismograms for extracting the information of shear-wave birefringence and the anisotropy distribution. (2) To improve our understanding on the mechanism of occurrence of any observed shear-wave birefringence in the shallow surface formations, particularly in the soft subsoils. Correlation with other subsurface properties, independently measured at the same site, should serve as a realistic approach to such explanation. (3) To improve our understanding on the practical implications of the field-observed shear-wave birefringence for the problems of civil or geotechnical engineering.

In this paper, we shall present the results of our research on anisotropy in near-surface formations and the field-observed shear-wave birefringence. To provide a background for our research, we shall at first explain briefly some basic concepts on anisotropy, and then review some major recent progresses that have occurred in observing anisotropy in the earth in various scales. This will follow a discussion of our strategy of research involving developments of both hardware and software. A new algorithm to process the 3-component VSP data contaminated by the effects of medium anisotropy and thereby to extract the polarization azimuth of the propagating shear waves will be presented. We shall discuss the data and the results from 4 different field experiments, 2 each for hard and for soft surface formations; these experiments are carried out in Japan and the United States at varying geological conditions. In soft subsoil layers we could observe significant shear-wave birefringence at some restricted depth zones that apparently correlates well with changes in composition, age, depositional environment, and the subsurface stress distribution. In hard rock, we shall report a generally good correlation of the polarization azimuth of the fast-split shear wave with the orientation of the cracks, even in scale of a few meters. We shall then verify the plausibility of our observed velocity variation as a function of varying medium stiffness, by numerical simulation of wave propagation in anisotropic media in dimensions of engineering interest. We shall finally discuss the geotechnical implications of these findings and hint on some future research problems.

2 Anisotropy, inhomogeneity and symmetries: a brief recourse to the basic concepts

A medium is anisotropic in a broad sense if its properties, when measured at the same location, change with direction. A medium is inhomogeneous if its properties, when measured in the same direction, change with location. At some scale, no solid is homogeneous; so whether a change of properties with direction distinguishes a solid as anisotropic or merely inhomogeneous is a function of scale. Homogeneity and isotropy are, therefore, not absolute characteristics of matter, but are terms applicable to properties averaged over some suitable length or volume; if the choice of scale were entirely arbitrary, these terms would not be particularly useful (White, 1965). For elastic wave propagation, the reference length that serves as a scale of measurement is the wavelength. Anisotropy as a concept of geophysics cannot be applied to every heterogeneous material, but only to those that may be treated as homogeneous on the scale of the wavelengths used to probe them. Anisotropy therefore implies variation of properties of homogeneous media with direction. For seismic waves, the scale to define homogeneity may be several to several tens of meters; for well logs, decimeters; and for laboratory measurements, a few centimeters. It is possible for both the degree and the type of anisotropy to be quite different in the same solid at different scales.

The advantage of identifying a medium as anisotropic is that a large body of existing theory and concepts can then be used to model its behavior. Behavior includes responses to stresses that propagate as elastic waves. Much of the theory and concepts for behavior

of anisotropic solids have been developed and used by scientists interested in crystal properties. Single crystals with regular lattices are homogeneous on a scale much smaller than the scale on which sedimentary rocks are likely to be homogeneous; yet, at the scale of seismic waves, seismologists have had considerable success modeling sedimentary rocks as homogeneous and isotropic. However, geophysicists need not always hold rigidly to this constraint of homogeneity. Some earth materials, for practical purposes, are locally homogeneous and anisotropic but vary systematically on a larger scale. It is appropriate to label some of these as anisotropic. Inhomogeneous materials may be termed anisotropic provided that variations in properties are smooth and predictable on the scale of the wavelengths used to probe them, and that such variations do not change the symmetry properties (Winterstein, 1990).

Fundamentally, what makes a homogeneous solid anisotropic is the systematic directional variability in the way the solid is put together. There is a limited number of different ways a homogeneous solid can be put together to make it appear basically different to an external observer. Hooke's Law provides us with 81 theoretically possible elastic constants. But fortunately, the basic symmetry properties of elasticity theory reduce the number significantly. The symmetry of stress components, strain components, and strain energy function cut the number of elastic constant required to describe the most general type of anisotropy to 21. Further reductions are possible if Mother Nature helps out by introducing elastic symmetry into the rocks during deposition or subsequently. Solids with lattices like those of crystals can be constructed in only 32 distinct ways except possibly for quasi-crystalline materials. These 32 are called the 32 crystal symmetry classes which group theory arranges into seven symmetry systems, commonly known as triclinic, monoclinic, orthorhombic, tetragonal, trigonal, hexagonal, and cubic (Bhagavantam, 1966; Auld, 1973).

Symmetry properties of a solid result from both its physical constituents and geometrical arrangements of those constituents. Anisotropy may be simpler for seismologists than for crystallographers because seismologists focus on symmetries of elastic properties only and not on symmetries of the rock themselves. These two symmetries are or not the same, and in fact, symmetries of a given property of a solid will always be as high as or higher than symmetries of the solid itself—an empirical principle attributed to Newmann (1885); also Love (1944). And higher symmetry generally implies more simplicity.

3 Observation of shear-wave velocity anisotropy in various scales: recent progresses

Observation of shear-wave velocity anisotropy in the earth has been reported in various scales. Although the results of our own research presented in this paper are confined essentially to the evaluation of anisotropy in very shallow surface-layers, we intend to discuss here briefly the broad field of evaluation of seismic anisotropy in the earth media in order to outline the background research that has already been done in this field, and to justify the partly review nature of this paper. We shall summarize some of the important observations reported in recent years in the following four categories, in decreasing order of the depth of occurrence of anisotropy and the scale of the observation. We choose to refrain from discussing the reports of laboratory measurements, physical modeling, and the numerous studies based solely on synthetic computations.

3·1 Observation in the mantle

There have been many investigations of the upper mantle anisotropy below the ocean basins: measurements of P_n velocity from refraction surveys (e.g., Raitt et al., 1969; Shearer

and Orcutt, 1986; Keen and Barret, 1971), and both azimuthal and polarization anisotropy in long-period surface waves (e.g., Forsyth, 1975; Anderson and Dziewonski, 1982; Anderson and Regan, 1983; Nataf et al., 1984, 1986; Tanimoto and Anderson, 1985; Nishimura and Forsyth, 1985, 1988, 1989; Montagner, 1985; Montagner and Nataf, 1986; Montagner and Tanimoto, 1990, etc.). A number of regional investigations suggest that the depth of the azimuthal anisotropy observed for sub-moho extends up into the crust and down to the base of the seismic lithosphere (Fuchs, 1977; Shimamura and Asada, 1983; Shimamura, 1984; Regan and Anderson, 1984; Estey and Douglas, 1986). Nearly all of these observations of mantle anisotropy can be successfully interpreted as due to the strain induced by plate-motion processes: seafloor spreading at the mid-ocean ridges, the differential motion of the lithosphere and asthenosphere, or more generally the mantle flow induced by the motions of the plates. The steadily increasing evidence that mantle anisotropy is due to strain-induced lattice preferred orientation (LPO) of upper mantle minerals (see Nicolas and Christensen, 1987), an idea originally proposed by Hess (1964), has provided a means of inferring the modes of mantle deformation from observations of seismic anisotropy.

An equally successful characterization of subcontinental mantle deformation from anisotropic observations is yet to fully emerge. Not only is plate tectonics less successful in describing the features of the continents and in predicting deformation in the subcontinental mantle, but the much shorter horizontal length scales of coherent continental deformation make the study of anisotropy more difficult using the techniques typically applied to the oceans. Notable exceptions are the few Pn observations on the continents (Bamford, 1977; Bamford et al, 1979; Vetter and Minster, 1981; Beghoul and Barazangi, 1990). The problem of smaller scales can be addressed by the use of the phenomenon of shear-wave birefringence or splitting illustrated in Figure 1. Splitting in teleseismic shear waves such as SKS, ScS and S, with steep arrival angles beneath the receivers, provides excellent lateral resolution in the upper mantle, and thus allows for direct comparison of anisotropy with surface tectonic and geologic features possessing typical continental dimensions. Measurements of shear-wave splitting in waves sampling the upper mantle began less than a decade ago using S-waves from nearby events in the descending slab (Ando and Ishikawa, 1982; Ando et al., 1983; Bowman and Ando, 1987) and ScS (Ando, 1984; Fukao, 1984). To enhance the epicentral distance range further ($>30°$), Vinnik et al. (1984) first utilized teleseismic splitting on SKS, which followed an extensive use of this phase (Kind et al., 1985; Silver and Chan, 1988, 1991; Ansel and Nataf, 1989; Savage et al., 1990). One major advantage of using SKS is that the observed anisotropy can be localized to the receiver side of the path due to the P to S conversion at the core-mantle boundary (CMB). Also SKS has a nearly vertical raypath through the mantle, so that the propagation direction is essentially constant, thereby allowing for a simpler analysis scheme. Use of S, ScS and SKS phases together in interpreting mantle anisotropy has also been recently attempted (Kaneshima and Silver, 1990, 1992). Anisotropy is also suspected to be present in the core-mantle boundary. However, the large-scale anisotropy in the lower mantle is possibly very small. Overall for the mantle, the assumption of localized, homogeneous, anisotropic zones appears justified; the distribution of these zones might be associated with local disturbances in the asthenospheric flow.

Assuming that the observed seismic anisotropy in the mantle is caused by the strain-induced lattice preferred orientation (LPO), there have been numerous studies to find the relation between anisotropy and strain: theoretical studies (McKenzie, 1979; Ribe, 1989, 1992; Ribe and Yu, 1991), laboratory measurements (e.g., Karato, 1992), and observations of mantle xenoliths (e.g., Nicolas and Poirier, 1976; Gueguen and Nicolas, 1980; Christensen, 1984). There are also studies to relate strain to geologic/tectonic processes, though many of them have failed to address the implications for the seismic anisotropy.

3·2 Observation in the crust

During the last two decades, details of crustal structure have been revealed through seismic reflection studies, seismic refraction and wide-angle reflection profiling, and three-dimensional seismic tomography. These studies indicate the presence of strong lateral heterogeneities in seismic velocity and impedance, in shallowest regions. In most of these studies, crustal media have been assumed to be isotropic. But with the increased use of three-component seismometers and large arrays, seismic signal-to-noise ratios have improved to the point where anisotropic effects have often been visible in the data, especially in shear wave data. Anisotropic behavior of crustal materials may be inherent; that is, it may be due to the anisotropy of the crystals from which a crustal rock is formed, or it may be induced by thin layering, fractures, or cracks. By comparing rock fabric with the anisotropy of linear compressibility and of thermal expansion, Brace (1965) confirmed that the alignment of anisotropic mineral grains can truly produce the anisotropic elasticity in crustal rocks. It is often found that the preferred orientation of minerals occurs along flow structures for igneous rocks, along foliation for metamorphic rocks, and parallel to the bedding plane for sedimentary rocks. Besides such inherent causes for crustal anisotropy, Nur and Simmons (1969), Anderson et al. (1974), Hoenig (1979), Hudson (1981), and Crampin (1984a) have proved that oriented cracks and/or pores can be the other major cause for seismic anisotropy in the crust.

Flaws, fractures, cracks, microcracks, and microinclusions are pervasive features of crustal rocks associated with trapped or circulating fluids, stress history, thermal events, deformation, and faulting. In granitic rocks, oriented microcracks are typical (Dale, 1923), and these cracks may be associated with residual and/or external stresses (Nur and Simmons, 1969; Sprunt and Brace, 1974; Plumb et al., 1984; Kudo et al., 1987). The fabric of microcracks often correlates with the anisotropy of physical properties: for example, with Young's modulus and uniaxial compressive strength (Douglass and Voight, 1969), compressibility (Todd et al., 1973), tensile strength (Peng and Johnson, 1972), etc. The fabric also produces dilatancy anisotropy under compression (Scholz and Koczynski, 1979) and anisotropic growth rate of subcritical cracks (e.g., Sano et al., 1988). A salient feature of fracture-related rock structure is the effective seismic anisotropy (particularly for shear waves). Crustal fracture structures which may be monitored by polarized shear waves range in dimensions from 10-100 km scale of crustal stress orientation and preseismic stress build-up, through the 100-1000 m scale of fluid reservoir structure and characterization, and 1-10 m scale of mining and geoengineering rock strain monitoring, to millimeter and micrometer or possibly smaller fluid inclusions determining the elastic response of the intact rock mass (Leary et al., 1990).

Heterogeneity in shallow regions brings inevitable difficulties into P-wave investigations of seismic velocity anisotropy. One is faced with the question of how to separate the effects of velocity anisotropy from the effects of strong heterogeneity. The phenomenon of shear-wave birefringence or splitting provides a new approach to solve this problem. Since split shear waves propagate along almost identical raypaths in a weakly anisotropic medium, the phenomenon of shear-wave splitting is much less sensitive to lateral heterogeneities than other phenomena such as P-wave travel time anomalies (Crampin, 1987).

In last few years it has become quite a general observation that the polarizations of short-period shear wave arrivals from local earthquakes show preferred alignment at a particular seismograph station and that this alignment is independent of the earthquake source mechanism (e.g., Booth et al., 1985; Kaneshima et al., 1987, 1988a, 1988b, 1990; Peacock et al., 1988; Kaneshima and Ando, 1989; Shih et al., 1989; Zollo and Bernard, 1989; Shih and Meyer, 1990; Gledhill, 1990, 1991; Savage et al., 1990; Vázquez-Contreras et al., 1993, etc.).

This has been explained by shear-wave splitting caused by local anisotropy in the upper crust, located beneath the observation point. The polarization of the shear waves is fixed by the symmetry of the anisotropy. Measurement of the polarization of the split shear waves and the delay between them, therefore yields information about the degree and the symmetry of the observed anisotropy, and hence the structure of the region. Most often it is the polarization of the first shear-wave arrival which is the best determined observation. To avoid distortion caused by interaction with the earth's surface, crustal observation of shear-wave splitting must be restricted to waves which arrive steeply under the recording station (Nuttli, 1961; Evans, 1984). This criterion defines a "shear wave window", a conical volume (maximum angle 35° to 50° from vertical) beneath a seismograph station from which undistorted shear waves are expected.

The explanation for these crustal observations, i.e., alignment of cracks and microcracks by the current stress field (Crampin et al., 1980, 1984), is related to the hypothesis of dilatancy, a high stress process which is thought to occur in the earthquake preparation zone (Nur, 1972; Scholz et al., 1973). There are a few reports of temporal changes in the extent of shear-wave splitting associated with crustal earthquakes (Gupta, 1973b; Peacock et al., 1988; Booth et al., 1990; Crampin et al., 1990), though these observations are not conclusive. Dilatancy is the small volume increase observed in rocks under high pressure, which is caused by the opening of cracks. It has been suggested that at stresses much less than are required for dilatancy, a phenomenon known as extensive dilatancy anisotropy (EDA) occurs (Crampin et al., 1984). In this process, cracks perpendicular to the maximum horizontal stress (σ_H) are colsed, leaving a preferential crack alignment parallel to the maximum horizontal compressive stress direction. The validity of the EDA hypothesis and the proposal that the orientation of seismic anisotropy is the same as that of the in-situ stress have not yet been sufficiently verified, and so remain debatable. There is also suggestion that subcritical crack growth can occur (Atkinson, 1984) and that in most cases the cracks will be water-saturated. There are also other models for aligned cracks (e.g., Nur and Simmons, 1969; Nur, 1971). Whatever might be the cause for these aligned vertical to subvertical cracks, their effect is to modify the elastic behavior of the crust, making it effectively anisotropic at the wavelength of the shear waves, which is assumed to be large compared to the crack dimensions (Hudson, 1981).

It is usually assumed that the observed anisotropy in the crust is pervasive and that at least the top 20 km of the crust is anisotropic. However, Kaneshima et al. (1988a), Kaneshima and Ando (1989), and Kaneshima (1990) have shown in Japan that the anisotropy is most likely to be confined to the top 10~15 km of the crust. Other authors have published data which indicate that there are large changes in the alignment of the fast shear wave arrivals between relatively nearby stations, thus implying that the observed anisotropy must be quite shallow (e.g., Peacock et al., 1988; Savage et al., 1989).

3·3 Observation in hydrocarbon and geothermal reservoirs

A crucial need facing the reservoir engineers working in the hydrocarbon, geothermal, or hazardous waste isolation industries is a means for detecting and locating the internal structures within the reservoir, particularly the distribution of the dominant fractures. The internal heterogeneity of a petroleum reservoir has a critical influence on its production performance. Where facies changes and structural deformation divide the reservoir into a myriad of compartments, open fractures provide conduits for fluid flow. Fractures are often found related to the subsurface stress distribution, which itself is another important target parameter for the geophysicists and the reservoir engineers. The analyses of shear-wave VSPs provide direct geophysical information about the in-situ reservoir rock, which

can be related to preferred directions of flow and other properties of the reservoir. In addition to VSPs, three-dimensional seismic shear-wave surveys can also potentially map the distribution of anisotropic structures within the reservoir.

Since the recognition of the fact in mid-1980s that in a sedimentary basin, anisotropy is an ubiquitous feature in several hundreds of meter of the subsurface, a number of field observations of anisotropy-induced shear-wave splitting have been reported. In the 1986 Annual International Meeting of the Society of Exploration Geophysicists (SEG), a number of oil companies for the first time reported the observation shear-wave birefringence in various sedimentary basins (e.g., Alford, 1986; Lynn and Thomsen, 1986; Willis et al., 1986; Corrigan et al., 1986; Naville, 1986; Frasier and Winterstein, 1986; Johnston, 1986). Since then, the recent 5～6 years have witnessed a number of successful observation of vertical birefringence of shear waves in both hydrocarbon and geothermal reservoirs. Clear evidences in oil and gas fields include those of Lefeuvre et al. (1989, 1993), Cox et al. (1989), Becker et al. (1990), Liu et al. (1991), Winterstein and Meadows (1991a, 1991b), etc., all of which employ VSP or crosshole measurements. After 1986, there are also a number of reports of the delineation of subsurface anisotropy in oil fields from the surface seismic measurements, specifically by 3-component or 9-component (i. e., 3 orthogonal source directivities and 3 orthogonal receiver components) seismic reflection surveys (e. g., Martin and Davis, 1987; Lewis, 1989; Lewis et al., 1991; Squires et al., 1989; Davis and Lewis, 1990; Mueller, 1991). Significant developments in processing techniques and theoretical computations for wave propagation in anisotropic media have also taken place in last several years.

Shear waveforms, particularly in VSPs, can also yield estimates of orientations of microcracks and macrofractures in both wet and hot-dry-rock geothermal reservoirs (e.g., Roberts and Crampin, 1986; Majer et al., 1988; Campden et al., 1990; Crampin, 1990; Sachpazi and Hirn, 1991). However, the number of such field verifications is still small. Also, the effects of cleavage, jointing and complex geology need to be carefully investigated before interpreting the anisotropy in terms of the internal structure of the reservoir. Crampin (1987) has discussed the geological and industrial implications of crack-induced shear-wave birefringence in reservoirs.

3·4 Observation in very shallow surface-formations

Unlike the above three categories of field observation of shear-wave anisotropy, for very shallow surface-formations which are of interest to the civil/geotechnical engineers, there are, as yet, very few reports of in-situ systematic evaluation of shear-wave birefringence. Besides lacking the economic resource potential, as compared to hydrocarbon or geothermal reservoirs, the near-surface poses several unique challenges. Considering the wavelength of the shear-waves (several to several tens of meters) used for exploration, the propagation distance is generally too short, which causes the effects of anisotropy on shear wavetrains to manifest in a relatively subtle way. Strong heterogeneities, small-scale structural complexities, and highly attenuating nature are also inhibitive for clear observation of anisotropic effects. The biggest challenge arises from the absence of an existing satisfactory model (like the strain-induced lattice preferred orientation of minerals for mantle, or EDA cracks for crustal rocks) to explain any observed anisotropy in shear-wave velocity and polarization in the near-surface, particularly in soft subsoil materials. Needless to say, this inadequacy of understanding is closely related to the insufficiency in attempts made so far in fields and the assumed negligibility of the effects of anisotropy in shallow layers for practical purposes.

However in recent few years, a number of field studies involving seismic reflection

and vertical seismic profiling have suggested that the near-surface might actually be more vertically birefringent to a shear wave than most of the more homogeneous or consolidated rocks at depth (Squires et al., 1989; Cox et al., 1989; Winterstein and Meadows, 1991a, 1991b; Mueller, 1991). Based on laboratory experiments on sand samples, Roesler (1979) and Lee et al. (1986) have reported shear-wave birefringence of about 5%, caused by anisotropic stress. However, relevance of these laboratory results is strictly restricted to the extent to which their samples represent the subsoils considered. Redpath et al. (1982) and Redpath and Lee (1986) were first to report clear indication of minimum 5% shear-wave birefringence at a shallow, alluvial sand/silt site and in the San Francisco Bay Mud, both in California. Revisiting the same datasets/sites of Redpath and associates, Lynn (1991) has presented an exclusive evaluation of the shear-wave birefringence in soft surface-formations in these Californian sites and has discussed on the possible causes. Both Redpath and associates and Lynn have attributed the observed birefringence in soft subsoil mainly to the directional variation in horizontal stress.

4 Evaluating shear-wave birefringence in near-surface formations: strategy of our research

A real earth medium cannot simply be either isotropic or anisotropic, but it can only be somewhere in a continuum from very weakly anisotropic to strongly anisotropic, and the position of demarcation depends on our observability in terms of both acquisition and processing. To delineate systematically the near-surface anisotropy, we have adopted a broad approach of research involving hardware developments, improved data acquisition technique in the field, developing efficient processing algorithm, understanding from synthetic modeling of wave propagation, and evaluation and interpretation of the observed effects of the near-surface anisotropy by correlation with other independently determined properties and structures. We arrange here the different steps of our research in the following order.

(i) Field experiments and hardwares needed: basic considerations.
(ii) Instruments used in field data acquisition.
(iii) Technique of data acquisition in field.
(iv) Developing the data processing algorithm and extracting the parameters of shear-wave birefringence from the field data.
(v) Processing of field data to evaluate shear-wave birefringence in surface formations. Incorporation of other independent observations. Interpretations.
(vi) Understanding the medium behavior by numerical computation of seismograms.
(vii) Assessing the geotechnical implications.

We shall first present (i), (ii), (iii) and (iv). This will be followed by a discussion of (v), separately for each of the 4 different field datasets, where the main observational findings of our research will be presented. After that we shall discuss on (vi) and (vii).

5 Basic considerations in field experiments and hardware development

The important differences in waveforms bearing information of seismic anisotropy are often quite subtle, particularly in the small scale of observation like ours. Extreme care in data acquistion, data processing, and interpretation is thus essential for success.

One very important requirement is the hardware capabilities to obtain the necessary good quality data under the conditions of engineering or geotechnical field surveys.

We decided to carry out careful field experiments in near-offset VSP geometry for 4 major reasons as follows. (1) The free surface imposes its own anomalies (attenuation, phase and amplitude changes, generation of precursory and subsequent phases disturbing the incident wave, disturbance, even for vertical incidence, due to the presence of any thin low velocity layer at the surface or local irregularities in topography or interface within a wavelength or two, etc.) on the polarization of the incident shear wave. This makes the analysis of anisotropy-induced polarization particularly difficult at the free surface. Shear waves recorded in VSPs by 3-component sensors placed within boreholes are much easier to interpret. (2) Shear waves recorded at the surface also suffer severe distortion due to mode conversions in case the angle of incidence is greater than the critical angle — arcsin (V_S/V_P). (3) In VSPs since the sensors are located close to the target depths, they can receive the local effects of anisotropy much more faithfully. This is crucial particularly if features of anisotropy change with depth, and if we are interested to monitor and interpret that change. (4) For vertical or subvertical cracks in rocks, that are normally considered common in shallow crust, it is known that the velocity difference between the two split shear waves is maximum when the incidence angle is within about 0°～35° relative to the direction parallel to the cracks (i.e., 65°～90° from crack normals). Since the near-offset VSPs produce steeply incident shear waves that sense better the velocity anisotropy caused by subvertical features, they are preferred to far-offset VSPs.

The essential hardware requirements for such meticulous VSP experiments are as follows. (1) Since the diameter of the shallow boreholes drilled for engineering prospecting is generally much smaller (seldom exceeding 100 mm) than those drilled for hydrocarbon exploration or for large reservoir studies, we need light and slender yet efficient downhole probes. (2) The shallow surface-formations are normally highly attenuating for not only the magnitude of energy but also for higher frequencies. In order to receive higher frequency seismic waves, it is thus necessary to be able to clamp the downhole 3-component geophones strongly against the borehole wall. (3) It is very advantageous if the orientation of the inhole geophone components can be controlled from the surface and thereby be predetermined during data reception at all depths. (4) Good engineering seismographs with high data sampling rate and broad dynamic range are also essential for acquiring good quality data. (5) High performance, smaller size geophones are necessary for being placed within the slender downhole sonde used in geoengineering surveys. We have tried to meet these requirements by employing specially developed downhole tool and seismograph systems.

6 Hardwares for field data acquisition

To receive good quality 3-component seismograms in a borehole, as is needed for delineation of the subtle effects of medium anisotropy for the short propagation distances of the shear wave, we have deployed a specially designed sonde system called "Borehole Shuttle". Borehole shuttle is a tested, multipurpose sonde that can be electro-mechanically strongly clamped against a borehole wall at any depth, and the absolute orientation of the sonde can be predetermined with the help of a rotary unit and a magnetometer. One main advantage of this system for engineering surveys is the small sonde diameter compared to the larger and heavier instruments generally used in large-scale explorations for hydrocarbon. This enables its use in holes with diameter less than 100 mm, though larger diameter borehole shuttles are now also available. In our experiments we have employed borehole shuttles

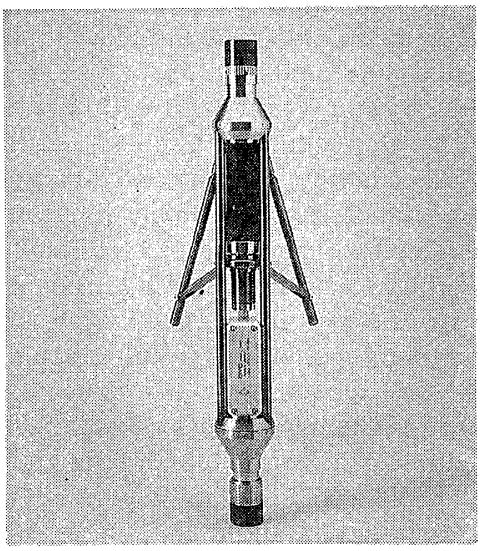

Figure 3. Borehole Shuttle (the 92mm probe).

of two different sizes; for relatively large diameter holes drilled generally in hard rocks (Field Experiments 1 and 2), we have used the sonde with 92 mm diameter (before arm expansion) and weighing 7 kg, and for slender holes drilled normally in soft formations (Field Experiments 3 and 4), we have used the sonde with diameter 51 mm (before arm expansion) and weighing only 2 kg. They are 40 cm in length. Figure 3 shows the appearance of the shuttle tool of diameter 92 mm. Ogura et al. (1989) have discussed the features of this engineering device, and Ohhashi and Ogura (1991) have analyzed its vibration characteristics. The maximum clamping force exerted on the borehole wall is 1000 N (for 51 mm diameter sonde) and 6000 N (for 92 mm diameter sonde). With high clamping force and the use of light-weight material, the borehole shuttle system provides remarkably broad-band frequency response for high resolution borehole seismic surveys.

In the upper part of Figure 4, the composition of the total sonde system used in our

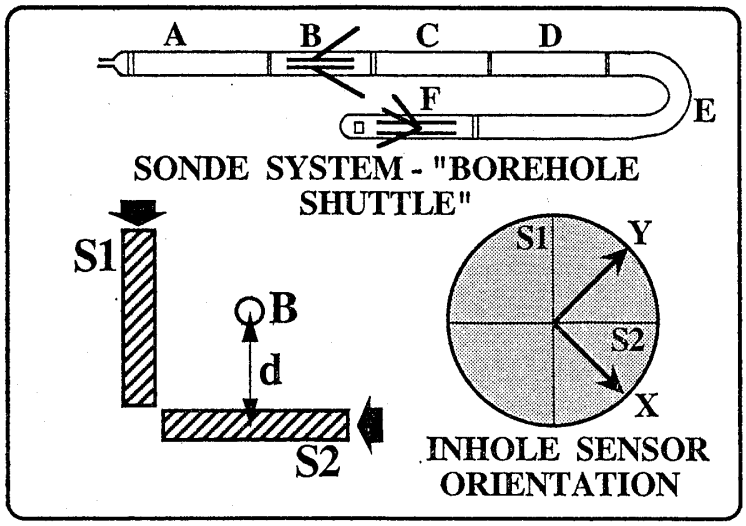

Figure 4. Basic layout of field experiments and the sonde configuration. The upper part illustrates schematically the various modules of the downhole system of the borehole shuttle; see in text for explanation on them. S1 and S2 are two orthogonal, plank-hammer type, surface shear-wave sources, and B is the borehole location in map view (refer also Table 1). X and Y are the two horhizontal components of the 3-component geophone clamped in the borehole.

experiments is schematically shown. F is the shuttle module housing the 3-component geophone. The other principal modules of the sonde system are a transformer unit (A), an anchor unit (B) to fix the sonde against the borehole in order to rotate the lower part of the assembly as desired, a rotary unit (C), a fluxgate magnetometer unit (D), and an isolation rubber tube (E). 3-component geophones (natural frequency 10 or 28 Hz) are installed in the shuttle housing (F) which is clamped firmly against the borehole wall. At each depth level of observation, the orientation of the horizontal components (called X and Y in this paper) of the inhole geophone can be easily controlled from the surface with the help of the magnetometer and the rotary unit. The accuracy of our orientation is ±5°.

The various operations of the downhole sonde system, e.g., anchoring the system, orienting the horizontal component geophones to some given directions, clamping the shuttle module against the borehole wall, checking the magnetometer reading, monitoring the digital seismograms on screen, evaluating the tool coupling, etc. can be carried out with the help of a shuttle control unit, known as "Borehole Shuttle 170", which can also function as a seismograph. We have used additional high-resolution engineering seismographs for our data recording. For Field Experiments 2 and 3 we have used 12 bit systems, but for Field Experiments 1 and 4 we have employed the instantaneous floating point (IFP) amplifier — McSeis 170f which has 20 bit resolution. The entire hardware system is produced by OYO.

7 Method of field data acquisition

The general layout of our field experiments is shown in Figure 4. S1 and S2 are two surface shear-wave sources placed orthogonal to each other. They are located close to the borehole, within 1.5 to 2 meters from the hole-mouth. Note that we call our sources as S1 and S2, unlike many other researchers who choose to designate the two split shear

Table 1. List of field parameters.

Expt. Condition	Field Expt.1	Field Expt.2	Field Expt.3	Field Expt.4
Location	Gifu, Japan	Illinois, USA	N. Kanto, Japan	S. Kanto, Japan
Ground Condition	Hard rock	Hard rock	Soft soil	Soft soil
General Lithology	Gneiss, Granite	Shale, Limestone	Sand, Silt	Sand
Field Geometry	Near-Offset VSP	Near-Offset VSP	Near-OffsetVSP	Near-Offest VSP
Source Type	Hammering Bolted Plank	Plank Hammering	Plank Hammering	Plank Hammering
Source Azimuth	S1=N95° E S2=N 5° E	S1=E-W S2=N-S	S1=N46° W S2=N44° E	S1=N20° W S2=N70° E
In-hole geophone orientation (X, Y)	X=N140° E Y=N 50° E	X=N135° E Y=N45° E	X=E−W Y=N−S	X=N155° E Y=N 65° E
Borehole Casing	Uncased	Uncased	Vinyl Chloride Casing	Uncased
Depth Range	5m~49m	79m~139m, 162m~204m	20m~44m	5m~49m
Depth Sampling	every 1 meter	every 2 meters	every 4 meters	every 0.5 meter
Data Sampling	every 50 μs	every 500 μs	every 500 μs	every 200 μs
Source Offset	1.5 m	2.0 m	2.0 m	1.65 m
Geophones (3-component)	10 Hz	10 Hz	28 Hz	10 Hz
Reception Freq.	5~4000 Hz	5~500 Hz	5~1000 Hz	5~4000 Hz

waves as S1 and S2. In our experiments S1 and S2 are two wooden planks of dimension 2.5m×30cm×20cm, which are normally fixed to the surface soil by heavy weights on them (e.g., front wheels of field vehicles raised on them or large water-filled drums and sand-filled sacks placed on them); however for Field Experiment 1 only, since the surface was hard rock, we had to bolt these wooden planks to the surface using three wooden poles and cement through holes dug on the rocks by drilling machines. Shear waves are generated by hitting these wooden planks horizontally on the edge with large wooden hammers. The generated waves are mostly SH waves, though some P and SV waves are also often produced.

We house a 3-component geophone (10 Hz or 28 Hz) in the borehole shuttle sonde as described earlier, and receive seismograms at various depths at a regular interval. In some occasions, we have used a string of geophones placed in multilevel shuttle housings and have covered a number of depth levels simultaneously. However, the data that we present in this paper and the results that we explain are all based on single level observations only. At first, the sonde is firmly clamped to the borehole wall at each depth level of observation, with the two horizontal sensors oriented to given azimuths. Shear waves are then generated by S1 and S2 sources at the surface, and are recorded by the downhole sensors. To check the arrival of the SH phase, we hit each source plank at two opposite edges and verify the polarity reversal in the signal. During observation at various depth levels, the absolute orientations of the two horizontal components (X and Y) of the geophone are always maintained constant with the help of the magnetometer and the rotary unit. In most investigations carried out earlier by other researchers, data were received with varying sensor orientation at varying depths (commonly the tension in the cable causes its twisting, resulting in arbitrary orientation of the sonde at different depths in the borehole), and then with the knowledge of the inhole sensor (obtained from a gyro or using the relationship between directions of wave propagation and particle motion polarization for known wave types), they were subsequently analytically rotated to a uniform orientation (e.g., radial and transverse) at all depths. However, there are various assumptions involved in these approaches, and the received wavefield is also affected if the orientation of the sensitivity axis of the geophone relative to a given incident displacement changes (Ghose and Takahashi, 1991). It is hard to avoid this problem if the direction of the incident displacement varies randomly with depth, which is not very common. It is still advisable to keep the geophone orientation constant and known at all observation points in the borehole. We have achieved this by using the borehole shuttle. Generally the X-component and the Y-component of the inhole 3-component geophone have been oriented at 45° relative to the orientation of the two perpendicular shear-wave sources at the surface, as shown in the inset of Figure 4. In our experiments, data in borehole have been received at every 50 cm to 4 m depth intervals. The sampling interval for the received seismograms is between 50 μsec and 500 μsec. The frequency window for reception has normally been kept wide, between 5 and 4000 Hz. Table 1 summarizes the field parameters of the 4 field experiments that we report in this paper.

8 Data processing algorithm

For a vertically incident, vector S-wavefield, the distribution of energy between the two orthogonal reception coordinates in the horizontal plane — X and Y, bears important clue to the local azimuthal anisotropy of the medium. The basic objective of data processing here is to find the natural polarization azimuths for the vertically propagating shear wave that correspond to the azimuths of the maximum and minimum effective rigidity (μ_e) in the

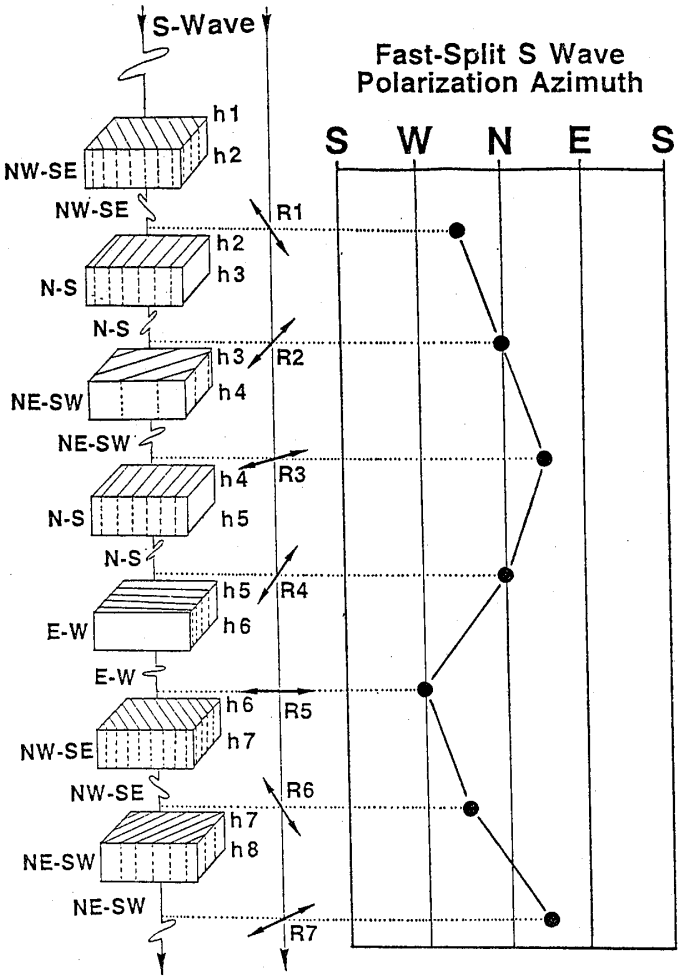

Figure 5. Fundamental objective of data processing illustrated. If the medium is vertically birefringent (because of any reason, say, by the presence of aligned subvertical fractures or microcracks, or due to aligned grains or pores, or for anisotropic horizontal stress, or else), and therefore causes splitting of shear waves (Figure 1), then from the azimuth of the fast-split shear wave we can determine the orientation of the local "stiff" direction of the medium in the horizontal plane. If R1, R2, ...etc. are geophones at various depths within a borehole, and if we can find the polarization direction of the fast-split shear wave for each of them independently, then it is possible to interpret the depth distribution of the orientation of the "stiff" direction.

immediate vicinity of an observation point in a borehole, and the magnitude of difference in the phase velocity of shear waves polarized in these two directions that indicates the magnitude of the effective rigidity contrast. The idea of depth distribution of the vertical shear-wave birefringence as a means to deduce the distribution of the elastically "stiff" direction of the medium, is illustrated in Figure 5. The cause of such vertical birefringence can be various. Assume that R1, R2, R3, ……, R7 are receivers at some regular depth levels within a vertical borehole that receives the 3-component seismograms. If in the depth range h1～h2 located immediately above the receiver R1 the "stiff" direction strikes NW-SE, then the fast-split shear wave arriving at R1 will be polarized also NE-SE (refer Figure 1). In the following depth range, say h2～h3 located between receivers R1 and R2, if the "stiff" direction changes its azimuth to N-S, then the fast-split shear wave arriving at R2 will ideally be polarized in the N-S direction, and so on for receivers R3, R4, ……R7. Now if from the received wavefield at various receiver locations we can extract the polarization direction of the fast-split shear wave, then we can find

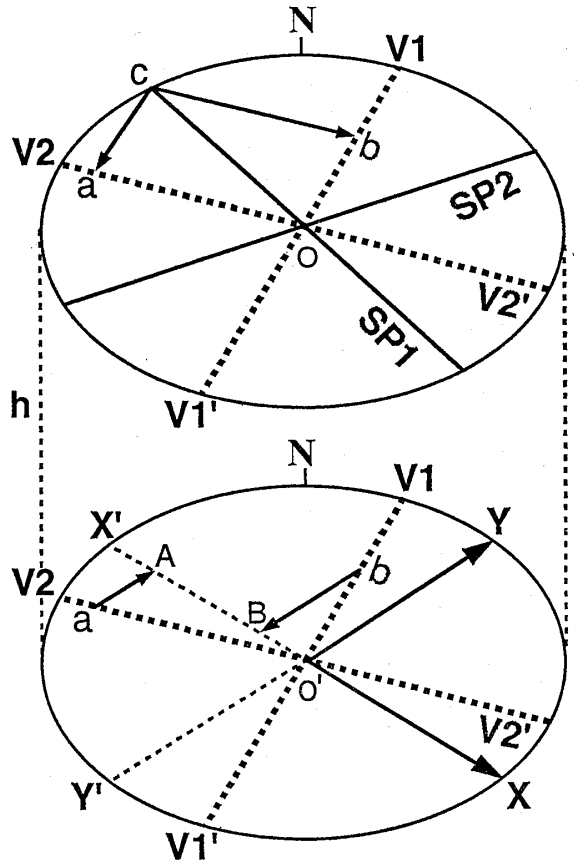

Figure 6. Basic philosophy of the proposed data processing technique (energy-minimization algorithm) that can efficiently decouple the shear-wave energy in the horizontal plane between the two horizontal-component receivers, in order to evaluate the parameters of the medium anisotropy. See in text for details.

the depth distribution of medium anisotropy, as illustrated on the right hand side of Figure 5. Also if we can decouple the fast-split and the slow-split shear waves at each receiver point, then from the difference of their respective phase velocities we can deduce the depth distribution of the degree of "stiffness contrast" in the horizontal plane.

The basic philosophy of the processing technique is schematically explained in Figure 6 where the top-view of a borehole with the aligned horizontal component geophones in it is shown. Let V1V1' and V2V2' denote the natural polarization azimuths for two velocity extrema (i.e., the "stiff" and the "weak" directions of shear strength within the horizontal plane). Let SP1 and SP2 be the respective polarization azimuths for two vertically incident shear waves at point O (note, there can be any number of incident waves and not necessarily two only; and though SP1 and SP2 have been drawn almost orthogonal to each other, they need not have any particular angular relationship between them). In case of vertical birefringence, an incident shear-wave displacement with magnitude OC and oriented along azimuth SP1 will be vectorically resolved into Oa and Ob, i.e., into the natural coordinates, and these two phases will propagate downward with different velocities. Now consider that at a point O' located at some depth (say h, that may correspond to the depth interval, say h1~h2, of Figure 5) below the point O, we have the 3-component geophone clamped against the borehole wall, and the absolute orientations of the two horizontal components -X and Y are known or predetermined, which is a reality in case of our field experiments. Vectorical projections of the displacements Oa and Ob, traveling at different velocities, will be received by the two horizontal geophones at point O'. If we focus on one geophone component only, say the X-component, the later will

receive O'A from Oa and O'B from Ob, as illustrated in Figure 6. In other words, each of the two mutually perpendicular horizontal geophones will receive both the fast and the slow shear-wave energy. For obvious geometric reasons the magnitudes of these two phase-energies received by the X- or the Y-component will not generally be the same (for example, as shown in Figure 6, O'A>O'B), and this will be determined by the alignment of the natural coordinates with respect to the observation coordinates. Now for case 1 (which should be the most general case), if Oa≠Ob, and say for instance Oa>Ob, then the equation $(O'A+O'B)_{min}=Ob$ holds always good (here $(O'A+O'B)_{min}$ is the minimum value of the sum of the vectors O'A and O'B for any angular orientation or azimuth of the geophone component, i.e., of O'X'). Next for case 2 (i.e., by a very special coincidence), if Oa=Ob, then the equation $(O'A+O'B)_{min}=Ob=Oa$, holds good. These suggest that if we can minimize energy in any one horizontal component of the inhole 3-component geophone by mathematical rotation of the received X- and Y-seismograms, then the rotated azimuth corresponding to minimum energy would coincide with one of the two natural coordinates, viz. the fast or the slow direction within the horizontal plane. At this orientation the fast and the slow energy will be best separated between the two horizontal components. The above equations will not hold if the two natural coordinates (V1V1' and V2V2') deviate significantly from orthogonality; they will remain valid when the deviation from orthogonality is small and within about 10°, which is generally sufficient. In case of the arrival of multiple-split shear waves, since the integrated phase energy along one of the two local natural coordinates is normally dominant over the other (i.e., corresponds to the case 1 discussed above), and since based on the above idea of energy minimization the energy of the phase/polarization that is statistically predominant within the chosen time window is minimized by independent mathematical rotation at each depth level and with initial geophone orientation known/predeterminded, the processing should derive the local natural coordinates faithfully.

While processing 4-component seismic data (i.e., two horizontal sources and two horizontal receivers) many of the existing techniques involving rotation scanning (e.g., Alford, 1986; Thomsen, 1988; Nicoletis et al., 1988; Winterstein and Meadows, 1991a, 1991b; etc.) implicitly make one or more of the following three assumptions. First, the polarizations of the two recorded split phases need to be orthogonal. Second, the orientations of the split shear-waves need to be consistent throughout the whole of the raypath; in other words, a layer with a given orientation of the fast and the slow directions has to have considerable thickness (several hundreds of feet). Third, the source spectra for the two surface shear-wave sources need to be close enough so that cross-correlating their respective traces can be justified. All of these assumptions are quite often not true, particularly in realistic field conditions. Even for zero-offset VSPs, slight nonorthogonality in the polarization azimuth of the split shear-waves may result if the strucuture is not horizontal and there are steeply dipping cracks (Li and Crampin, 1993). The processing technique that we introduce here does not assume orthogonality of the two split shear-waves, as discussed above. The second prevalent assumption of depth-invariant natural coordinates is unrealistic for most practical purposes because in any shallow prospecting the primary interest is to know not the average fracture or stress orientation only, but also to derive the depth distribution of these properties. The third assumption is also quite often hard to justify, and can potentially invite erroneous interpretations. In fact in our field datasets too, we find some clear difference in the predominant frequency between the S1 and S2 sources, caused by the difference in the state of ground coupling and/or ground condition between the two surface shear-wave sources. This is rather common and unavoidable in actual field conditions.

Based on the idea explained earlier, we have developed an algorithm to decouple efficiently the fast and the slow shear-wave energies between the two horizontal components.

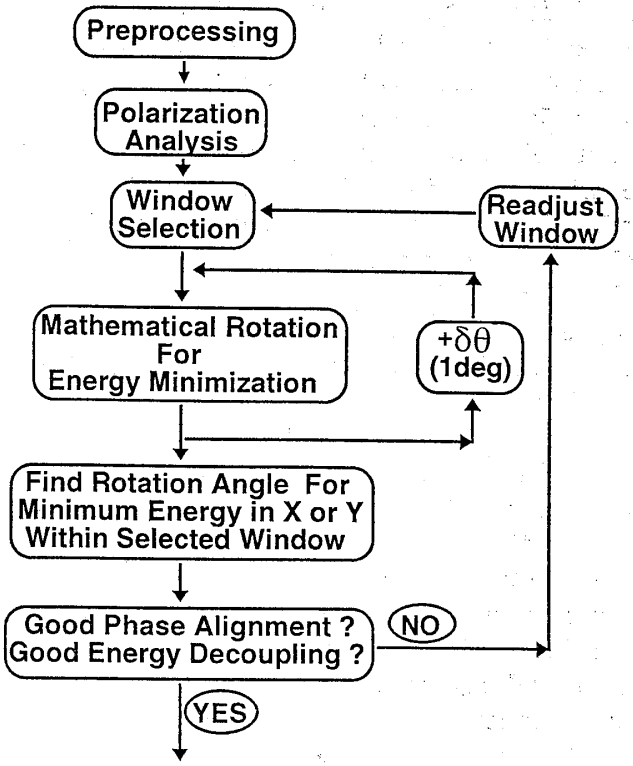

Figure 7. Flow chart of data processing.

As the inhole geophone orientation is predetermined in our field experiments, in processing we can avoid the above three assumptions. For each source and each depth level the processing is done separately. The complete flow chart of our algorithm is shown in Figure 7. Preprocessing of data includes source time correction and bandpass filtering. This is followed by polarization analysis of 3-component seismograms.

To estimate correctly the direction of the incident polarization at a given depth and to correlate it with the same at other depths, it is important that the process of energy-minimization is carried out on a constant phase at all depths. For simple cases it is not difficult to achieve this. But for complicated situations (like in Field Experiment 1, to be described later in this paper, where the two source-generated signals arrive one after another within a short interval of time), it is difficult to compute the incident polarization azimuth, particularly for any later arriving slow phase. As it is well-known now, the fast-split phase arrives earliest, and being least distorted is easy to identify; this fast phase is normally expected from one of the two sources, S1 and S2. However, the later phase will tend to be a mixed one. For such complicated shear wavetrains, one possible way to achieve consistency in prescribing the correct location of the time window for analysis can be the polarization analysis of the observed wavefield.

A principal polarization direction is first determined by maximizing the power in the direction of the incident displacement. Assuming the trajectory of the particle motion a triaxial ellipsoid, the polarization parameters given by the geometry of the ellipsoid are derived by eigen analysis of the covariance matrix of 3-component particle displacements. Observed seismograms are then projected onto the eigen vector that corresponds to the maximum eigenvalue of the matrix, and a single waveform is generated for each depth level. The most distinct S phase consistently appearing at all depths in this synthesized waveform is identified, and a time window broad enough to include sufficiently a first arrival wavelet for the fast and the slow shear waves, to provide an accurate statistical representation of the energy of

these two waves, is located for each depth level. Generally we have used a window width of about one wavelength centering around the first peak of the identified phase.

In the next step, we rotate mathematically by 180° the two horizontal components at an interval of 1° to find the angle at which the energy within the selected window in one horizontal component becomes minimum. At this rotation, the predominant shear-wave energy within the chosen time window is focused on the other horizontal component. The energy within a given time window is the sum of the square of amplitude at all sample points; as an alternative, we have calculated by trapezoidal rule the area within the seismogram for the chosen time window. The computation time required to find this energy minima is minimal as the energy is computed only for the restricted time window. Since the orthogonality of the split shear-waves is not assumed here, unlike Alford rotation (Alford, 1986) or layer stripping (Winterstein and Meadows, 1991a) algorithms, simultaneous minimization and maximization of the energy between the cross-components is not done. These various steps of processing are carried out interactively for the entire dataset; and the efficiency of energy minimization, the phase alignment in trace pasteup, and the satisfactory energy-decoupling between the two horizontal components are confirmed before accepting the final solution.

For the two different shear-wave sources with widely separated polarization directions, we have minimized the energy in the alternate horizontal components (i.e., X for S1 source and Y for S2 source, refer Figure 4). The justification for energy minimization in the alternate component (X or Y) for S1 and S2 sources is that, if the "stiff" and the "weak" direction of the medium in horizontal plane be respectively close to the directions of S1 and S2 source polarizations or vice-versa, then S1 and S2 energy would preferentially be split into more fast and more slow shear-wave energies, which would ultimately lead to a focusing of these different modes in X and Y components for S1 and S2, respectively. In field data, we indeed notice more energy in the alternate horizontal-component receivers for the two sources, and they possibly correspond to fast and slow, or slow and fast shear waves, respectively. Thus in case of two different source polarizations, the cross-component energy minimization is desirable.

9 Field experiments

We present here the data and the results of 4 field experiments carried out during 1989 ~1992. The first two are carried out at hard rock sites, while the next two are performed at soft soil sites. The sites for experiments 1, 3 and 4 are located in Japan, while the site for experiment 2 is in the United States of America. Experiments 1 and 4 are more elaborate, and considerable independent information are available for them; for experiments 2 and 3, the amount of additional information is relatively less. We shall discuss experiments 1 and 4 in somewhat greater details than experiments 3 and 4.

9·1 Field Experiment 1: Hard, Mesozoic, Metamorphic Rock Site, Gifu Prefecture, Japan.

(a) Site characteristics and geology

The site is located about 130 km northeast of the Nagoya city, in a mountainous region that is underlain by the Hida metamorphic rocks, one of the oldest rock formations in Japan. The underground is hard, fractured, Mesozoic gneiss and intrusive granites with V_P~6 km/sec and V_S~3 km/sec. Prominent structures of gneiss e.g., bands, laminations and veins of epidote, chlorite and calcite, as well as bands and veins in granites are distinct on the cores recovered from the test borehole (Figure 8). Examination of core reveals that these lithological structures

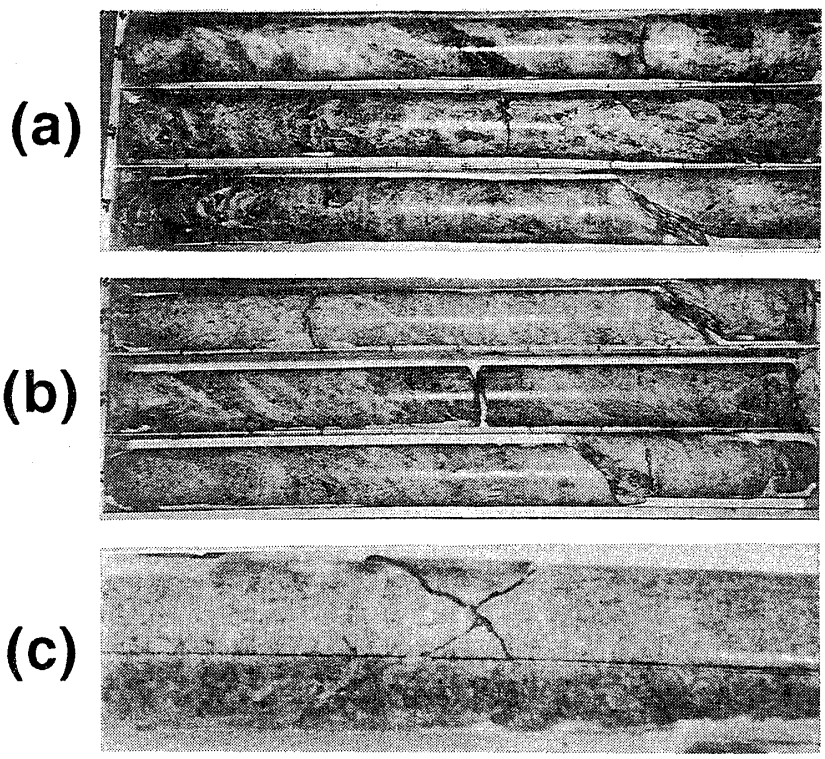

Figure 8. Field Experiment 1: Photo of cores showing lithologic structures (veins, laminations, bands, etc.) in gneiss and granite rocks; distinct cracks are found oriented along these structures. (a) cores (24~27m) in gneiss; (b) cores (42~45m) in granite; and (c) example of conjugate cracks (32.6m).

have basically two preferred alignments orthogonal to each other, NNE-SSW and WNW-ESE. The presence of many well-developed, steeply dipping cracks, generally following one of these two principal trends of rock structures, is also clear. Conjugate cracks can be identified at certain depths. The site is traversed by one of the most prominent Quaternary active faults of Japan-the Atotsugawa fault, a nearly 100 km long right-lateral strike-slip fault aligned about NE-SW (Figure 9). For this reason, a strong directionality of the local stress regime is anticipated.

Detecting on shear wave seismograms from crustal earthquakes over a wide range of source zones and source-receiver azimuths in the whole of Japan (40 stations in 10 different regions), Kaneshima (1990) has reported shear-wave splitting that is attributable to crustal anisotropy. For majority of stations the direction of the leading, fast-split shear wave is found parallel or subparallel to the maximum compressive stress. However for Hida region, where our present test site is located, as one of the few exceptions the fast-split shear-wave polarization is found to be much deviated from the maximum stress direction, and relatively close to the local alignment of gneissosity. Kaneshima and Ando(1986) reported subparallel alignment of the leading shear waves observed at station Amajo (AMJ) which is located only a few tens of kilometes away from our present test site. Here the fast-split shear wave is found polarized approximately NNE-SSW. The tectonic stress regime in this region is well examined through the analysis of earthquake focal mechanisms and strikes of active faults (Mikumo et al., 1988). It has been inferred that the maximum compressive stress is WNW-ESE and the minimum compressive stress NNE-SSW. The leading shear-wave polarization direction is almost perpendicular to the maximum compression. Around station Amajo, the ground rock is highly anisotropic gneiss, same as our test site, and the geological trend coincides with the foliation plane and strikes NNE-SSW (Nozawa et al., 1975). Kaneshima (1990) has, therefore, interpreted the observed fast shear-wave polarization in the Hida region and the crustal anisotropy as having the lithologically induced component strong enough to mask the

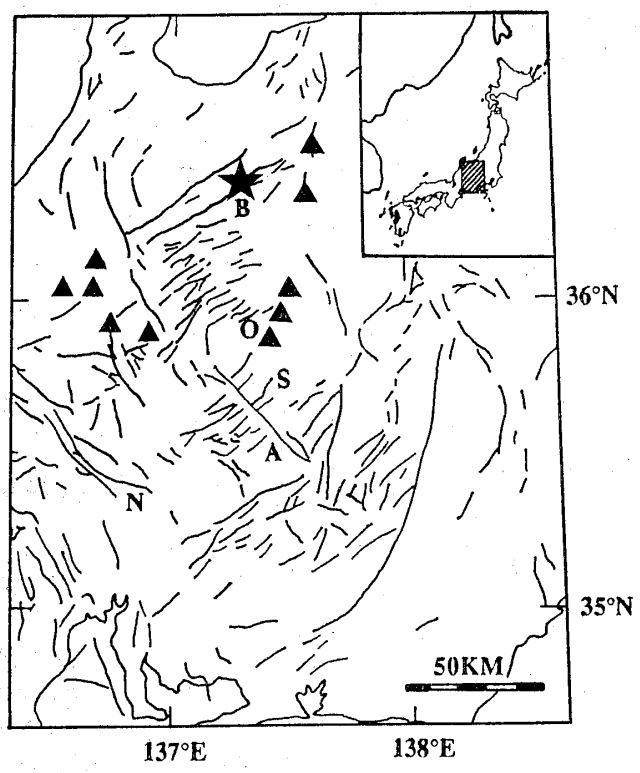

Figure 9. Field Experiment 1: Major tectonic features in central Japan and location of our experiment site (asterisk). Solid lines are active faults, from the Research Group for Active Faults (1980). Classification of fault activity is also given by them. A: Atera Fault (class A-B); B: Atotsugawa Fault (class A); S: Shirasu-Touge Fault (class A-B). Triangles are Quaternary volcanoes (O: Ontake Volcano). (After Yamazaki et al., 1992)

effects of stress-related cracks on seismic velocities.

Figure 10 shows the detailed geology of the near-surface rock formations derived from the analysis of cores. Primary minerals are hornblende, k-feldspar, epidote, chlorite, diopside, hematite, muscovite and biotite. A sharp change in geology is evident around 33 meter depth. The depth region shallower than 33 meter is composed primarily of gneiss, while below 33 meter it is predominantly granite. Depths around 33 meter mark a definite change in the environment of petrogenesis.

(b) Experimental conditions

The main field parameters have been listed in Table 1. One special feature of this site is that there is no soil cover at all, and hard rocks extend right from the surface. To generate shear wave on such hard rock by plank-hammering, we have bolted the wooden planks S1 and S2 to the ground, using three wooden poles and cement. As a result, when each source plank (S1 or S2) is struck at the edge horizontally, along with SH-wave, polarized in the direction of the strike, sufficient SV-wave, polarized perpendicular to SH, is also generated. In such near-offset VSPs, since the propagation direction for seismic waves is almost vertical, the S-plane is nearly horizontal; so SV displacement lies in almost the same horizontal plane as SH, but polarized 90° to the SH motion. Due to a source motion involving plank and poles, the SV-wave is found to originate slightly later than the SH-wave.

(c) Field data

The uncased borehole drilled in hard rock is very clean. The sampling rate of the received seismograms is high (50 μsec). Figure 11 shows our observed 3-component seismograms. Note the good signal-to-noise ratio. We have succeeded to observe shear waves

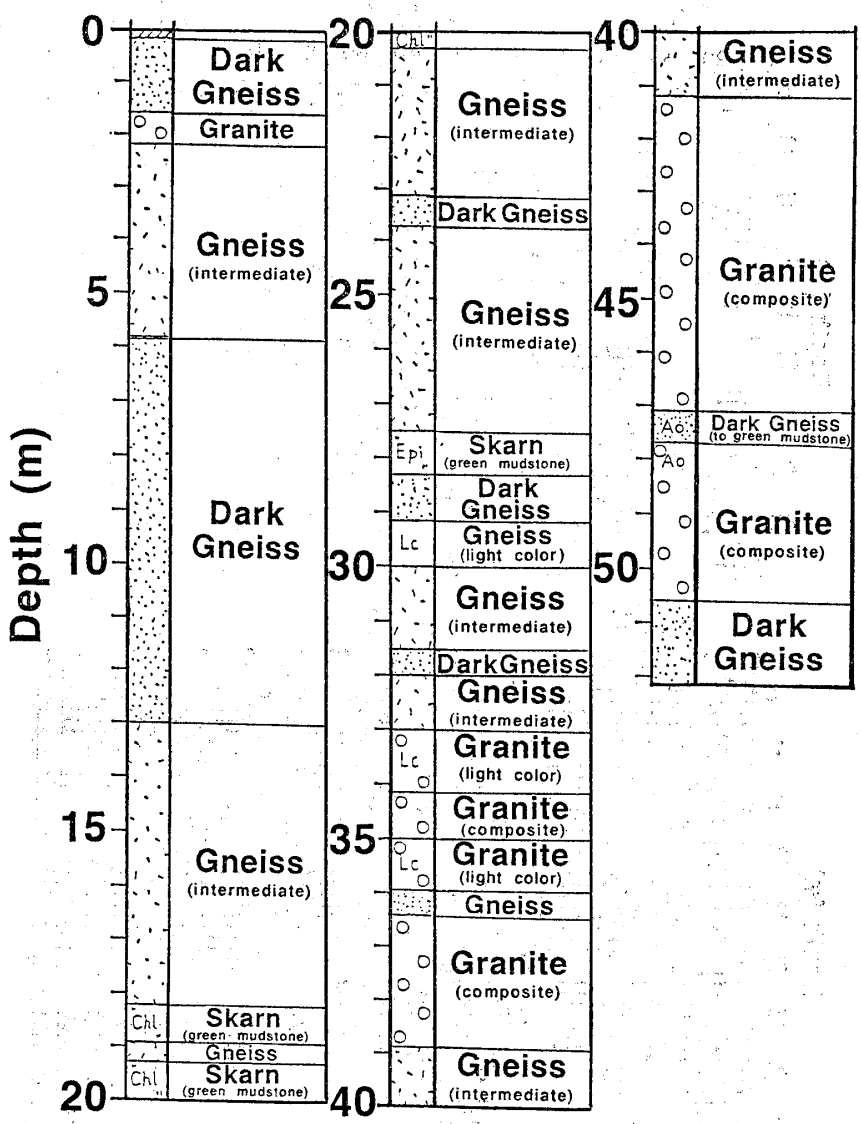

Figure 10. Field Experiment 1: Detailed geology of the underground rocks determined from analyses of cores.

with frequency well exceeding 100 Hz. A careful examination of field seismograms reveals that the alignment of the principal S-wave arrival differs slightly between X- and Y-component seismograms. The first-arriving shear-wave energy in the X-component from the S1 source is a little faster than that arriving in the Y-component from the S2 source. Another important feature noticeable in field records is that, although the two horizontal geophones are oriented at 45° from each of the two perpendicular directions of source polarization (Figure 4), there is more energy in the X-component for source S1 and more energy in the Y-component for source S2. These two observations indicate the fair possibility of the interference of medium anisotropy on shear-wave propagation in this site. In Figure 12, the observed particle motion at the shallowest depth level is shown. Note the peak SV arrival (marked by b) in the X-Y plane about 2~3 msec after the peak SH-arrival (marked by a). This shows that there are actually two shear-wave signals, separated by about 2 msec, generated by each source, and these two are nearly perpendicular to each other. It is difficult to present a definite explanation about the mechanism of generation of the cross-polarized shear wave by plank-hammering; it, however, appears likely that the motion of the wooden poles grounded into the rock, that we have used for bolting our source planks, is responsible for the generation

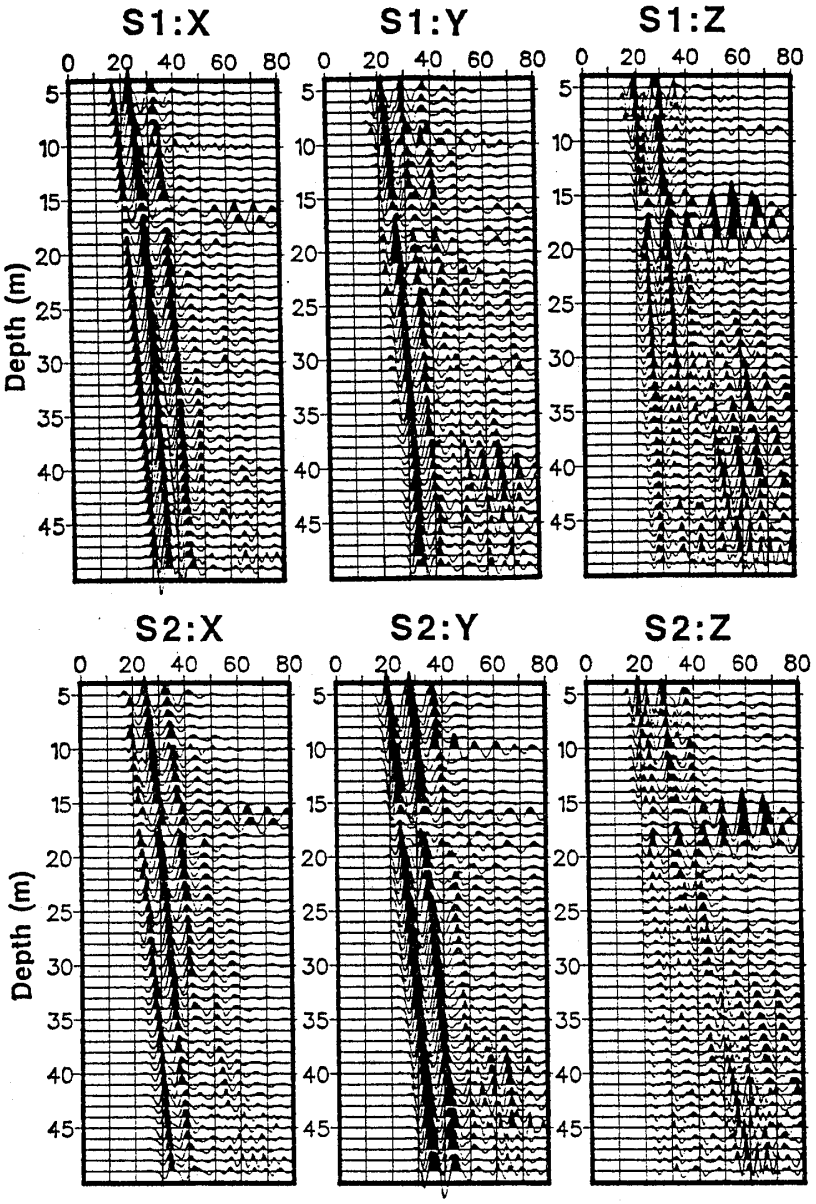

Figure 11. Field Experiment 1: 3-component seismograms for S1 and S2 sources received within the borehole. The seismograms are 50-350 Hz bandpass filtered and corrected for any source-time variation; X-, Y- and Z-component traces at each depth are normalized relative to the maximum value of amplitude in them.

of the two orthogonally polarized shear waves.

(d) Results of processing

The processing of the source-time corrected and band-pass filtered (50-350 Hz) seismograms is carried out following the procedure discussed earlier (Figure 7). The shear-wave energy in the X-component for S1 source and in the Y-component for S2 source, within a 3-msec time window (corresponding to half the period and 60 sample points), is minimized by mathematical rotation of the horizontal component seismograms. The time window for minimization at each depth is located by prior polarization analysis of the 3-component records. For this dataset, we have used a relatively narrow window because of the complexity arising from the arrival of two separate signals that are separated at the origin by only about 2 msec.

The selection of time window by polarization analysis is illustrated on field data in Figure 13, where θ and ϕ are the measures of the direction of wave propagation respectively

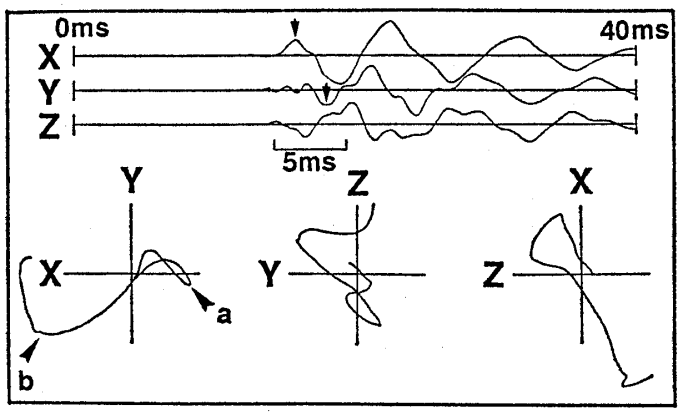

Figure 12. Field Experiment 1: Observed 3-component seismograms for source S1 received at depth 5 meter and the hodograms in a 5 msec window. a and b are arrivals of the peak displacement for the two perpendicularly polarized S-phases generated by source S1.

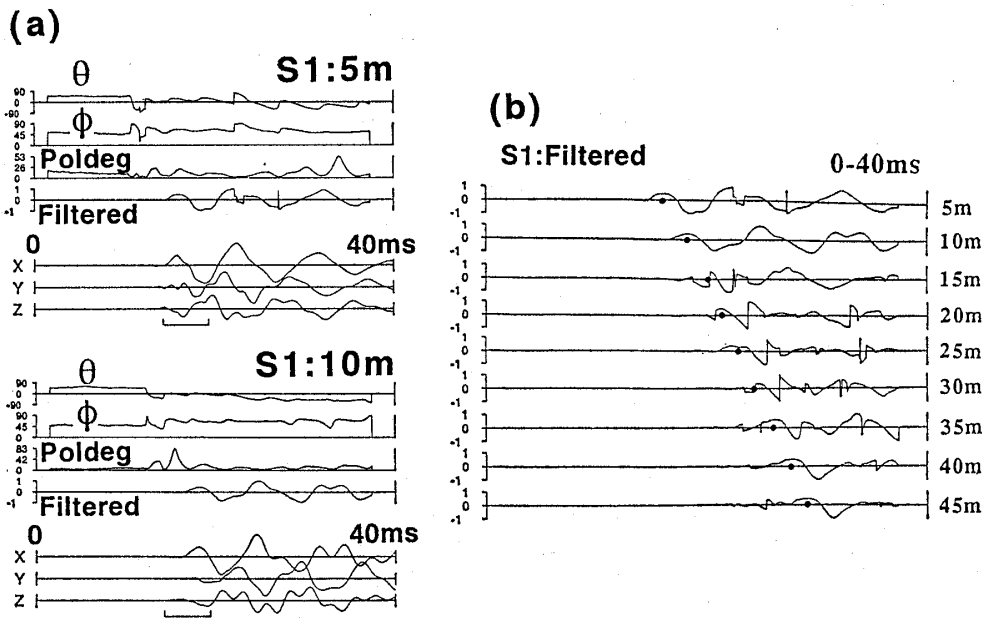

Figure 13. Field Experiment 1: Illustration of the result of polarization analysis for determining the location of the time window for subsequent processing of energy minimization. (a) Time variation of the polarization parameters, illustrated for the 3-component seismograms (shown for 0-40 msec) received at 5 and 10 meter depths, for source S1. The analysis has been carried out here on a 30 msec wide sliding time window. See in text for explanation of θ, ϕ and "Poldeg". "Filtered" is the seismogram obtained by projecting the observed 3-component seismograms onto the eigen vector that corresponds to the maximum eigenvalue of the covariance matrix of observed displacements. (b) The location of the time window for energy-minimization at each depth is selected around the peak time (shown by the black dot) for a given phase appearing consistently at all depths. Here the "Filtered" traces at 5 meter interval for source S1 are shown.

from the strike of the sagittal plane and from the vertical axis, as estimated from the orientation of the particle motion ellipsoid obtained by eigen analysis of the covariance matrix of the observed 3-component seismograms. "Poldeg", a measure of linear polarization, is affected by various factors, and so is not useful for our purpose. However the filtered waveform, "Filtered", generated by projecting the three-component seismograms onto the eigenvector that corresponds, the maximum eigenvalue of the covariance matrix of the observed 3-component displacements, can define a given phase quite consistently. The crest or trough of the phase aligned consistently

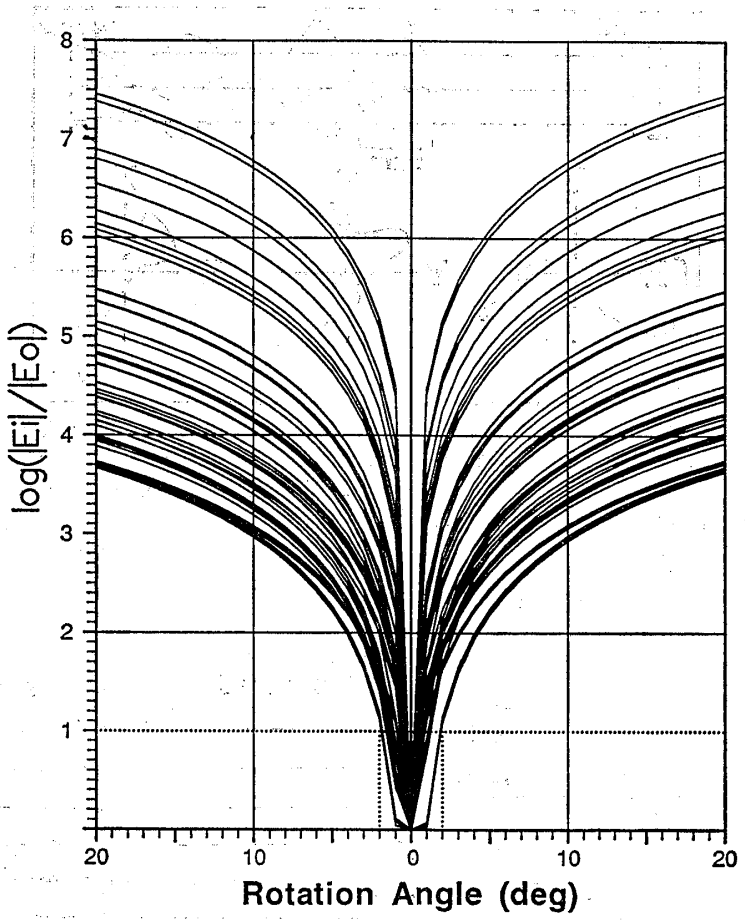

Figure 14. Field Experiment 1: Efficiency of energy minimization by the proposed algorithm, as a function of rotation around the orientation of energy-minima (0°). E_0 is the achievable minimum energy within the chosen time window, and E_i is the energy at some other rotation.

in the pasteup of filtered waveforms (Figure 13) can be picked as the center of the time window for energy minimization. Since the energy-minimization scheme proposed here searches the polarization direction that statistically dominates the chosen time window, it is stable. We find that any slight variation of the window width does not affect the result much.

Figure 14 illustrates on field data the efficiency of energy decoupling by our processing. Here, the energy at a particular rotation angle normalized with respect to the minimum energy is plotted as a function of rotation around the angle corresponding to the energy minima. For S1 source, curves for all depth levels are shown; the result is similar for S2 too. The convergence is sharp. Within ±2° the energy increases by about 10 times, signifying small error bar for our azimuth estimates.

For S1 and S2 sources the processing is performed separately. Figure 15(b) illustrates the result of our processing for source S1; compare with the result of processing assuming isotropy (Figure 15(a)). In Figure 15(b), S1X:Rot and S1Y: Rot are the post-rotated, decoupled X and Y components, respectively. The rotation to achieve best energy-decoupling is carried out at each depth independently, and so they are different from depth to depth. To compare the result of processing for the two surface shear-wave sources, Figure 16 shows the processed seismograms of the alternate horizontal components for them, i.e., S1X: Rot and S2Y:Rot. In all such plots, the peak time of a given phase (marked by black circles and squares) has been searched digitally. A number of important observations can be made on the processed data as follows.

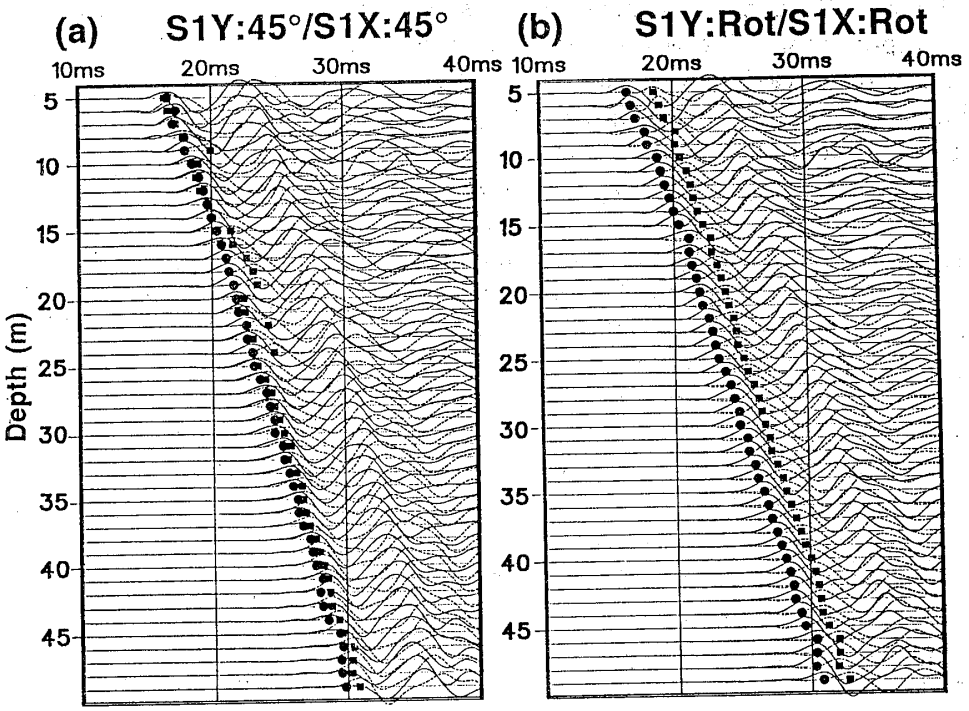

Figure 15. (a) Field Experiment 1: Y (solid line) and X (dashed line) seismograms (source S1), after 45° rotation at all depths. (b) Energy-decoupled Y and X seismograms for source S1, S1Y:Rot and S1X:Rot, for which the rotation angle is determined separately at each depth. Black circle and black square mark the arrival time of the peak S-phase in Y and X, respectively.

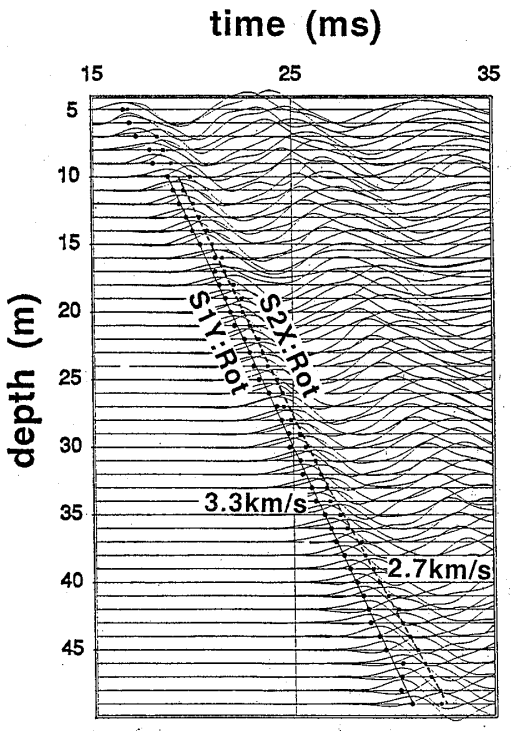

Figure 16. Field Experiment 1: Results of the best possible energy-decoupling for S1 and S2 sources. Note that, up to around 32 meter depth there is no clearly visible difference between the phase velocities in the energy-decoupled seismograms for S1 and S2 sources; however, below 32 meter depth a slow phase appears in S2X:Rot. See in text for interpretation.

(1) Note in Figure 15(b) the distinct separation of energy between the two rotated, horizontal components. The prominent energies visible in the two decoupled horizontal components and progressing with almost a constant separation (about 2 msec) maintained between them, are the two orthogonal shear waves generated at the source (Figure 12). Since X and Y components of the geophone in the borehole are oriented at 45° from the S1 and S2 source orientations, in case of no anisotropic interaction, a clockwise mathematical rotation by 45° of the two observed horizontal-component records (refer Figure 4) should separate the energy uniformly at all depth levels. But the reality is clearly not so. In Figure 15(a), the observed seismograms rotated clockwise by a constant amount of 45° at all depths are shown. Comparing Figure 15(a) with Figure 15(b), it is evident that it requires different amount of rotations of the observed X and Y components at different depths to achieve constantly the best separation of shear-wave energy between them. This can only be explained if the polarization directions of the incident shear wave varies with depth, i.e., if shear-wave splitting occurs. Notice in Figure 15(b) that the alignment of phase arrival is significantly improved after the processing; this feature is used interactively during processing as an important check of the efficiency of energy-decoupling and for any fine adjustment of the window location. The improvement in phase alignment in X and Y components is a result of relatively uniform decoupling of the two source-generated signals between the two horizontal receivers, at all depths. Another very important observation that offers credibility to our energy-minimization algorithm is that, comparing Figure 15(b) with Figure 15(a), the shape of the waveform is much improved after our processing, and this improvement is consistent in depth.

(2) Comparing the two plots in Figure 15, it can be seen that when the observed horizontal component seismograms are rotated, the time of the shear-wave phase in S1:Y (solid line) does not change as much as it does in S1:X (dashed line). This is because the observed S1:Y has already a certain amount (though not to the extent as in observed S1:X) of the phase that we are driving by rotation from the X- to the Y-component; in other words, this particular phase, located in the chosen time window, is being enriched by our rotation, as its major resolved part originally arriving in the X-component is now being focused on the Y-component. However in case of S1:X, we are driving a given phase as much as possible out of the chosen time window; consequently the phase that remains in S1:X is different from the one being driven out by rotation, and hence its time is different. When the rotation that corresponds to the best possible decoupling is achieved at each reception point (Figure 15(b)), the two phases are completely separated between X and Y components.

(3) One very important observation of the interaction of medium anisotropy on shear-wave propagation is possibly visible in Figure 16. Here we compare the phase velocities of the first of the two phases that are generated by each of S1 and S2 sources, which are now decoupled respectively in S1Y:Rot and S2X:Rot. At first sight it is clear that the difference in their phase velocities is not recognizable up to about 30～32 meter depth, but below that the phase velocity in S2X:Rot sharply decreases from nearly 3.3 km/sec to 2.7 km/sec — a decrease of over 20%. Some major change in the orientation of the medium stiffness is surely occurring around 30～32 meter depth, and our rotation scheme can resolve that change for the S1 source, and thereby can follow the same phase through the entire depth range of our observation, but it cannot do the same for the S2 source. This apparent, sharp decrease in the phase velocity in S2X:Rot can be interpreted as to be due to the mixing of a slow-split phase of the source-generated later signal, that results from a change in the medium symmetry commencing around 30～32 meter.

(4) From Figures 15 and 16, it is clear that the variation of the polarization direction due to a change in medium symmetry can be observed (from the change in the rotation required at various depths to decouple energy between the two horizontal components, as shown in Figure 15(b)) more easily than the variation in velocity. It is well-known that of the two critical observations that can be made of the split shear waves, i.e., measuring their polarization directions, and measuring the delay between them or finding the difference in their phase velocities, the estimate of the polarization direction of the fast-split shear wave is relatively more stable and accurate. The fast-split polarization is essentially a local phenomenon that depends only on the symmetry of the last anisotropic region that the ray has passed through, which for a VSP may well be immediately adjacent to the geophone. The polarization direction is not particularly sensitive to the degree of anisotropy. The arrival of the slow-split mode, and hence the delay between the two split shear waves or their velocity difference are phenomena that depend on the properties along the ray path; they are much less easy to measure or interpret reliably. It is rather common, particularly when the propagation distance is short or the degree of anisotropy is small, that the arrival of the later, slow-split shear wave is superimposed on the wavetrain of the fast-split shear wave; the later arrivals can also be masked by reverberations generated by near-surface lateral heterogeneities. Delays are also sensitive to the matrix velocities in rocks containing cracks, and are likely to vary rapidly with direction in a complicated manner. The velocity variation between fast and slow shear waves is particularly difficult to observe in our present dataset because in such a high-velocity, hard-rock medium the travel-time is very short, and since the complicated source motion creates additional difficulties by generating two closely timed signals, their split phases interact with each other in a complicated manner. It is apparent in Figure 16 that, though our processing carried out on the observed S1X has succeeded to catch the same phase (i. e., a given fast or slow phase that changes polarization direction with propagation) althrough (and so we find nearly constant phase velocity), on S2Y it has not been able to do so below 30~32 meter, because within the chosen window the observed S2Y possibly contains very closely spaced fast- and slow-split phases with comparable energy content between them (and hence we notice a clear change of the phase velocity). Contamination is more expected for the slow-split phase. The predominant energy in the observed S2Y, that has successfully been decoupled by our processing up to the depth of about 30~32 meter, is more likely to be the slow-split phase, while that arrived at all depths in the observed S1X is possibly the fast-split phase.

By our processing, S2X:Rot (and S1X:Rot too) becomes oriented to the slow direction of the medium up to the depth of about 32 meter; the other orthogonal, source-generated signal (the later one) gets aligned to the fast direction. But they are separated originally by about 2 msec. Now below 32 meter, there is possibly a significant change in the orientation of the fast and slow directions of the medium. As a result, the fast-split and the slow-split phases are again split into the new fast and slow directions. This can explain how an additional slow phase can appear below 32 meter (as visible in S2X:Rot in Figure 16); this is the fast-to-slow split wave for the later signal, which is hard to resolve for the S2 source.

As mentioned earlier, compared to the polarization direction and its depth distribution, the velocity difference between the split shear waves is more difficult to ascertain stably when the propagation distance is so short. Nevertheless, we have tried to see if any gross, statistical trend can be seen in the velocity relationship between the decoupled S-energy arriving at X- and Y-components from S1 and S2 sources. We calculated the interval velocity anisotropy, given by (VSY—VSX)*100/VSY, using the digitally read phase

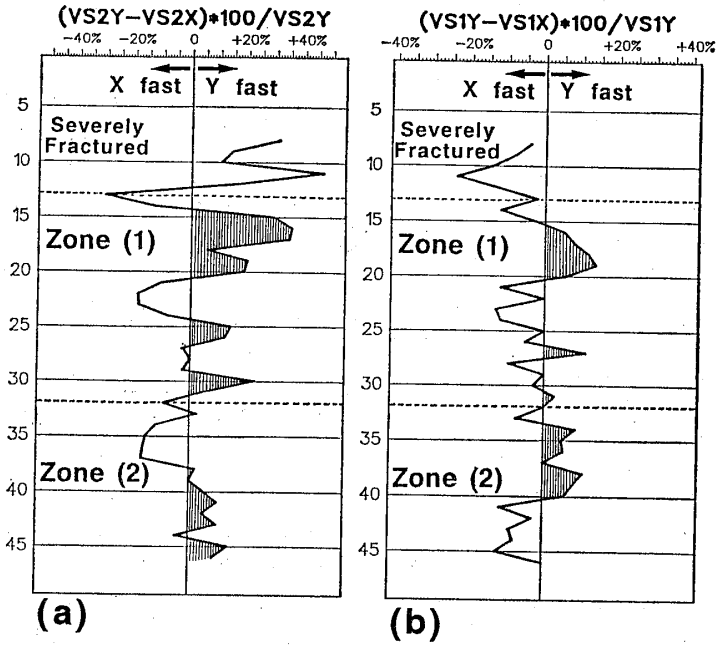

Figure 17. Field Experiment 1: Interval velocity anisotropy calculated for the two orthogonally polarized S-phases generated (a) by source S2, and (b) by source S1.

times (crest or trough, as marked in Figures 15(b)). The depth distribution of the interval velocity anisotropy is shown in Figures 17(a) and 17(b). In this particular illustration, the depth interval used is 6 meters; the sliding interval is moved always by one depth level, and the estimated velocity anisotropy is plotted at the center of the interval. One should observe here the gross trend only and not the very small fluctuations resulting from scattering noise. The very shallow region (5 meter to about 13 meter) has possibly received the effect of drilling and other heavy construction works carried on the surface at our test site, because of which it is too heavily and too randomly fractured to reflect any meaningful pattern in the velocity distribution. However below that, if we compare the distributions in Figures 17(a) and 17(b), we can distinguish comfortably two depth zones; approximately 13～23 meter: Zone(1), and 32～45 meter: Zone(2). In Zone(1), the distribution is grossly the same between S1 and S2. In Zone(2), this relation is sharply opposite between S1 and S2. One obvious conclusion is that there is a sharp change in the medium around 30～32 meter, that is affecting differently the propagating wavefields from S1 and S2 sources.

For such short propagation distance, it is difficult to resolve confidently the magnitude of the shear-wave birefringence. Referring to Figures 17(a) and 17(b), it is apparent that the magnitude varies with depth. These digitally estimated values of interval velocity anisotropy have a signal part and a noise part. The correlatable distribution between S1 and S2 sources (Figures 17(a) and 17(b), respectively) strongly suggests a coherency of the signal part between them. It appears that at certain depths the birefringence, averaged over 6 meters, is as high as 20%; the average value of it would be about 10%.

(5) As the sensor azimuth is predetermined during observation, from the estimated rotation angle for energy minimization, the azimuth of the energy-decoupled X and Y components can be derived at each depth. In Figure 18, the azimuths of the energy-decoupled Y and X components for respectively S1 (solid line) and S2 (dashed line) sources, viz. S1Y:Rot and S2X:Rot, are plotted against depth. The corresponding processed seismograms have already been shown in Figure 16. The cross-component polarization

azimuths for the two sources are shown here to illustrate the results of independent processing on S1 and S2 datasets; obviously S1X:Rot and S1Y:Rot orientations will be exactly orthogonal to each other, so will be S2X:Rot and S2Y:Rot. In Figure 18, it is very clear that up to 30~32 meter depth, S1Y:Rot and S2X:Rot are almost 90° separated from each other (nearly WNW and ENE, respectively), and their depth distributions are quite similar; they possibly represent the two directions of the velocity extrema (fast and slow) in the horizontal plane. A clear but gradual change takes place below about 32 meter; the polarization of S1Y:Rot slowly changes from WNW to about NS and beyond, while that of S2X:Rot changes slightly from ENE toward north. This happens because below 30~32 meter the symmetry of the medium changes from WNW toward NS, and our processing of seismograms for S1 source succeeds to identify that change and rotate the Y-component always to the orientation of one principal axis (the fast direction). We therefore notice a nearly constant phase velocity in the processed traces for source S1, for the entire depth range (Figure 16). Though in the scale of our observation and with the frequency that we have used, it is difficult to see easily the difference in the phase velocity between S1Y:Rot and S1X:Rot (Figure 15(b)), it is likely that they correspond to the polarization directions of the fast- and slow-split shear waves, respectively. For S2 source, though our processing has correctly decoupled the fast and the slow phases up to 30~32 meter depth, as we notice very good matching in the depth distribution of the derived polarization directions between S1 and S2 (Figure 18) and the unchanged phase velocities, below 30~32 meter, due to the superposition of multiple-split phases from the two source-generated signals, the processing has not sufficiently decoupled the fast and the slow phases. The discrepancy between the derived orientation of the polarization azimuth between S1 and S2 below 30~32

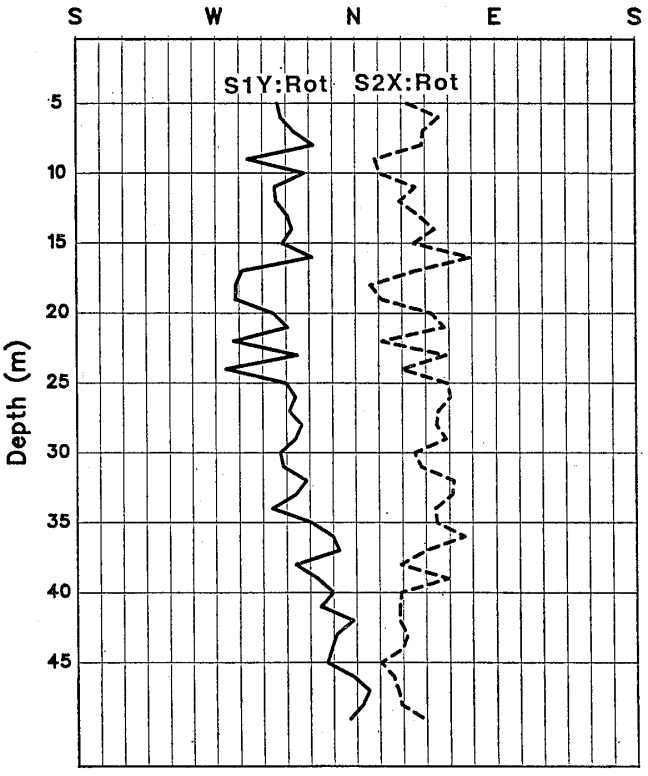

Figure 18. Field Experiment 1: Depth plot of the polarization azimuth of shear-waves in S1Y:Rot and S2X:Rot, calculated from the amount of rotation needed for energy-decoupling at each depth and the absolute orientations of X- and Y-component geophones known during observation. Solutions for sources S1 and S2 (solid and dashed lines, respectively) are mutually independent ones.

meter (Figure 18) is therefore closely related to the apparently sharp change in the phase velocity in S2X:Rot (Figure 16) occurring around 30~32 meter depth.

(e) Discussion: correlation with other independent observation

The site of our experiment is made of relatively homogeneous, hard rock with little variation in the major physical properties. Figure 19 shows the unfiltered P-wave seismograms recorded in the same borehole between 15 and 50 meters. P wave is generated by a vertical impact source at the borehole-mouth. The seismograms show impressively high signal-to-noise ratio. A V_P of nearly 6 km/sec can be assigned to this shallow rock formation. Evidently, there is little V_P variation in the whole depth range, reflecting relative homogeneity.

We have also obtained a number of geophysical logs in our test borehole. Figure 20 shows caliper, γ-ray (uncorrected density), apparent resistivity (micrologs), and self-potential logs. The caliper log shows that the borehole is very clean, which is also confirmed by the amount and the shape of the recovered cores. The borehole diameter decreases slightly with depth as a consequence of drill-bit erosion. The two micrologs shown correspond to two different electrode spacings (short- and long-normal); they also reflect no significant change with depth in the physical properties of the medium around the borehole. The self-potential increases linearly with depth, which is usual. The density distribution along the borehole, as reflected in the natural γ-ray log, does not exhibit any sharp change too. All these observations indicate that the medium around our borehole is relatively homogeneous.

However, the prominent lithologic structures (Figure 8) that characterize the gneiss and the granite rocks in this test site are expected to create significant anisotropy

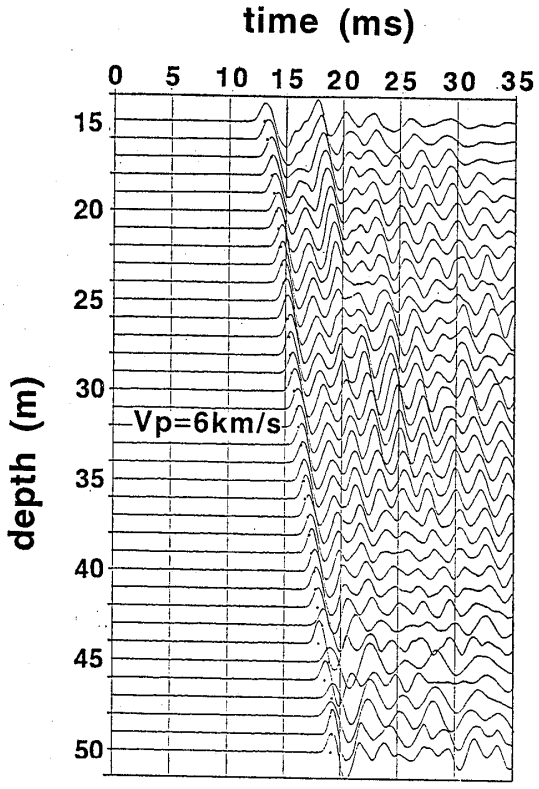

Figure 19. Field Experiment 1: Unfiltered vertical component seismograms for P-waves generated at the hole-mouth (by vertical impact). There is clearly no change in V_P with depth, indicating relative homogeneity of the subsurface and good reception condition.

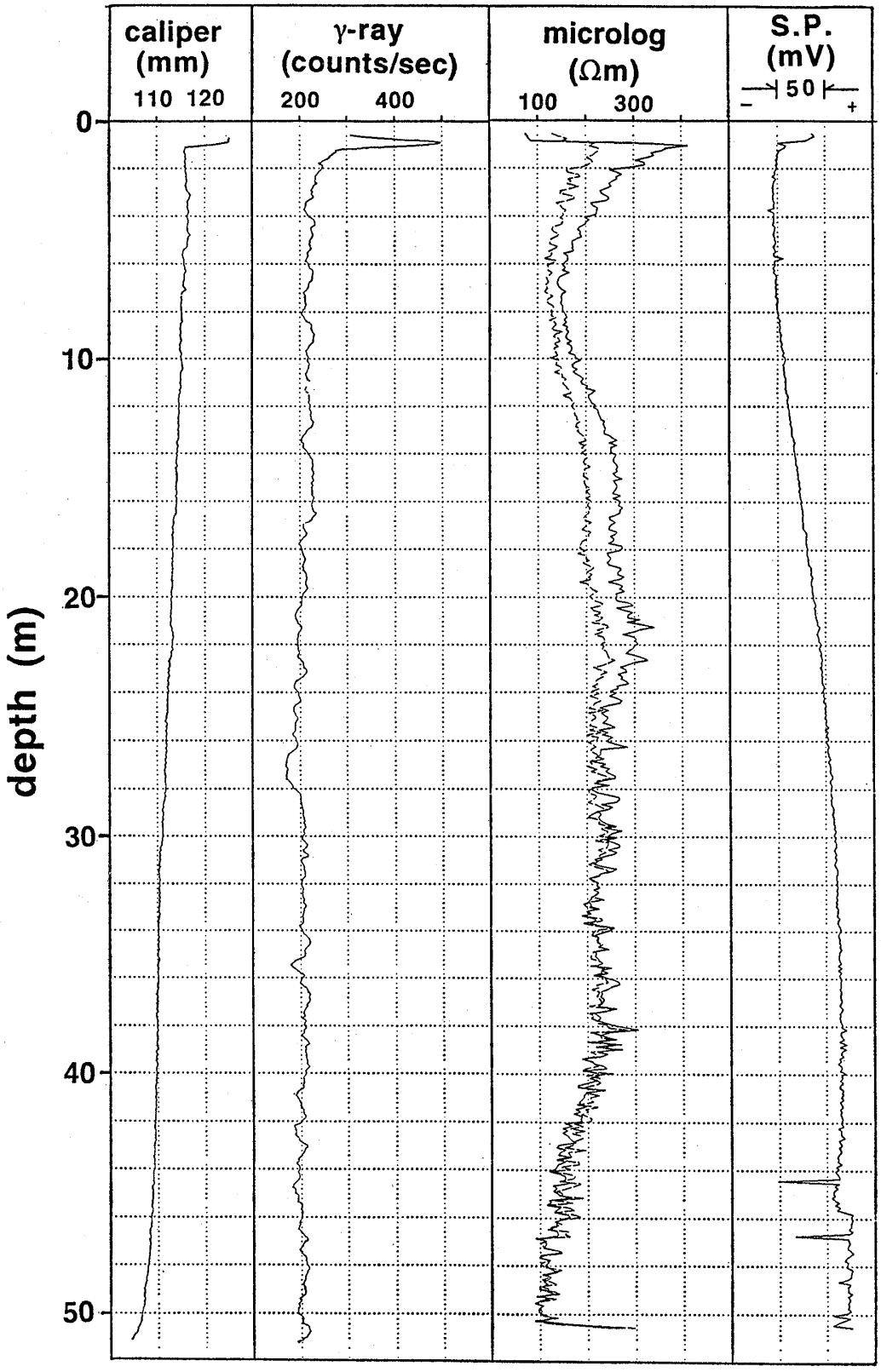

Figure 20. Field Experiment 1: Geophysical logs indicating no sharp variation of the physical properties of the medium with depth.

in the elastic properties. We have obtained the results of acoustic emission tests on rock samples derived from a drill-hole located very adjacent to our test hole. From these tests, the average value of the Young's modulus under uniaxial stress, in a direction parallel to the prominent lithological structure is found to be even 20% greater than that across the structure.

Excepting at very shallow depths (up to 12~13 meter) where, as mentioned before, the rock is severely and rather randomly fractured partly due to the heavy construction and drilling operations carried at the surface, the core recovery from our test hole is almost 100%. Figure 21(a) shows the percentage core-recovery plotted against depth. Examination of cores establishes the presence of numerous distinct cracks with steep dips, developed along prominent lithological structures, e.g., bands, veins, laminations, etc. in gneiss and granite. Often there are clear changes in color along the crack plane. It is certain that the crack orientations are lithologically controlled. Figure 21(b) plots the number of cracks per meter in cores. After careful inspection of the crack surface and other related features, we have selected only those cracks which are formed surely not due to the effect of drilling, but which represent the natural condition of the rock. We have measured carefully dip and strike of each distinct crack. Table 2 presents the dip and strike of the thin cracks that we have measured on the cores. The crack strike is measured on cores with the help of borehole TV images. There are many subvertical cracks with dip exceeding 60°, though some shallow dipping cracks are also found in the very shallow (<10 m) and in relatively deeper parts (>30 m) of our borehole. We find that the cracks generally follow one of the two preferred lithologic directions.

In Figure 22, black dots represent the strike of the distinct cracks measured on cores; light shadow highlights the general trend in the depth distribution of cracks.

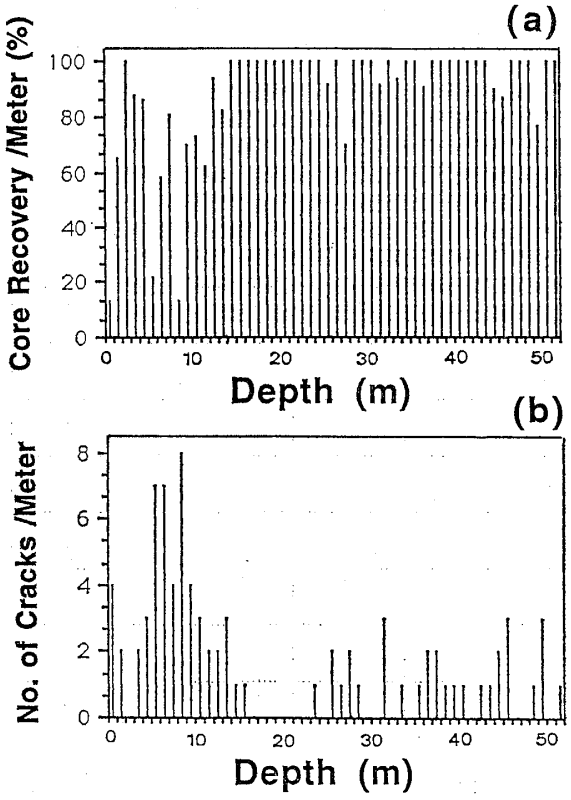

Figure 21. Field Experiment 1: (a) Core recovery per meter versus depth.
(b) Number of cracks per meter versus depth.

Table 2. Attitude of cracks measured in cores.

No.	Measurement depth (m)	Strike (deg)	Dip (deg)	Remarks	No.	Measurement depth (m)	Strike (deg)	Dip (deg)	Remarks
1	5.20	N10W	88	not very accurate	32	30.20	N62W	80	
2	5.80	N 9W	60		33	31.30	N66W	27	(conjugate)
3	6.50	N42W	60		34	31.30	N22E	58	(conjugate)
4	6.70	N16W	44		35	32.28	N158W	48	
5	7.10	N82W	54		36	32.60	N50E	60	smaller one (conjugate)
6	7.28	N20W	35		37	32.60	N 5E	40	larger one (conjugate)
7	7.43	N 4E	40		38	35.37	N128W	25	
8	7.55	N44W	70		39	36.40	N138W	72	
9	7.80	N55W	35		40	36.70	N122W	66	
10	8.10	N60W	73	prominent fracture zone	41	37.53	N10E	30	
11	8.18	〃	73	〃	42	37.73	N 6W	35	
12	8.45	〃	73	〃	43	38.35	N 8W	47	
13	8.70	〃	73	〃	44	39.05	N90W	66	
14	9.00	〃	73	〃	45	39.95	N111W	40	possibly a crack
15	9.80	N 0E	68	major one (conjugate)	46	40.67	N101W	39	
16	〃	N72E	82～98	minor one (conjugate)*	47	42.85	N14E	40	
17	10.30	N42W	86		48	43.05	N47E	38	
18	10.45	N63W	35		49	44.70	N30W	33	
19	10.80	N28W	85	upper part of the plane	50	44.90	N47W	50	
20	〃	N 5E	—	lower part of the plane*	51	45.08	N25W	56	
21	10.98	N32W	48		52	45.30	N10W	33	
22	11.70	N50W	65		53	45.70	N 4E	38	
23	12.60	N46E	104	slightly twisted crack plane	54	48.47	N20E	30	smaller crack (conjugate)
24	13.80	N70E	104		55	48.55	N70E	67	larger crack (conjugate)
25	15.50	N68W	75		56	49.54	N70W	43	smaller surface (conjugate)*
26	17.10	N57W	78		57	49.54	N18W	24	larger surface (conjugate)
27	18.50	N20E	84		58	49.65	N60E	82	
28	20.30	N70W	125		59	50.00	N66E	73	
29	25.80	N92W	100	very pronounced fracture	60	50.33	N72E	42	
30	27.50	N57W	—		61	51.85	N45E	42	
31	29.00	N63W	80						

* Not considered as a representative one.
The dip is measured perpendicular to the strike, and toward the upthrown sude.

Because of the random fracturing in very shallow depths (up to about 13 meter), the crack orientation does not show any prominent trend here. But below that, up to about 32 meter, it is clear at first sight that the general crack strike is consistently WNW. At around 32 meter the crack orientation changes quite sharply. The scatter in crack-orientation data below 32 meter is a real feature caused by clear contortions on the crack plane and appearance of conjugate cracks. Between about 32 and 39 meters, crack orientation lies dispersed between nearly NS to N50°E. Then between 39 and 45 meters, the general crack orientation appears to change from nearly N50°E up to NW. Below this depth there is possibly change again in crack orientation toward NE, but as our observation hole ends, we do not have much data below.

In Figure 22, we have superposed the derived distribution of polarization azimuth of S1Y:Rot and S2X:Rot (same as Figure 18). Comparing the observed crack orientation profile (black dots) with the derived profiles of polarization azimuth of the energy-decoupled S-phases in S1Y:Rot and S2X:Rot (solid line and dashed line, respectively), the most striking result that emerges is that up to about 32 meter depth the polarization azimuth of the S-phase in S1Y:Rot lies close to the azimuth of the steeply dipping cracks measured on the cores; the azimuth of S-polarization in S2X:Rot lies at almost 90° from the crack orientation here. At 32 meter, as the general crack azimuth changes sharply, we notice also the beginning of a clear but gradual change in the S-polarization azimuth in S1Y:Rot toward the new direction of general crack azimuth; the shift is not clear for S2X:Rot, for which the polarization azimuth passes closer to the general crack strike below 32 meter.

In Figures 17(a) and 17(b), it is found in Zone (1) as common for both S1 and S2 sources that, VSX>VSY in a few narrow depth regions viz. 14~15m, 21~25m, 27~28m,

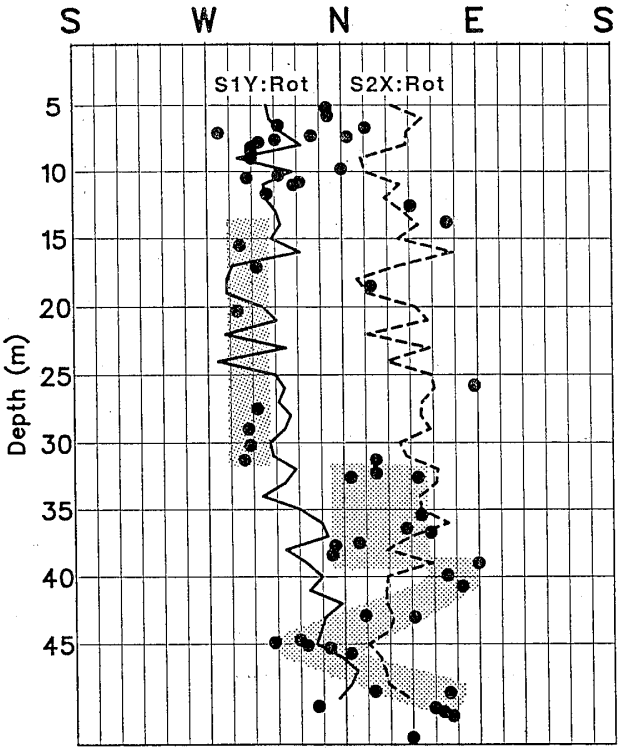

Figure 22. Field Experiment 1:Distribution of the shear-wave polarization azimuth versus the distribution of the crack azimuth. Black dots are individual crack strikes measured on cores using borehole TV images. Hatches indicate the general trend of the depth distribution of crack azimuth. Solid line (S1Y:Rot) and dashed line (S2X:Rot) show depth distribution of polarization azimuth of the energy-decoupled S-phase from the two sources.

and for the rest VSY > VSX. Comparing this with Figure 6 we see that in Zone (1) the cracks are oriented close to the azimuth of the Y-component (for both S1 and S2), i.e., predominantly in the fast direction. Between 21 and 25 meters depth where VSX > VSY, we find that the rock is more massive and intact, and the cores are totally devoid of cracks; also the orientation of a prominent crack located around 26 meter depth is indeed closer to the polarization azimuth of the S-phase in the energy decoupled X-component. For both S1 and S2 sources, the change in fast direction of the medium within such small depth interval indicates the sensitivity of shear-wave polarization to the presence and attitude of cracks. In Zone (2), however, the situation becomes relatively complex as we also find the crack orientation to be remarkably scattered. Though there is surely a shift in the orientation of the medium symmetry, the fast direction of the medium is possibly not as well defined in Zone (2) as in Zone (1). For S1 source the fast shear wave has satisfactorily been resolved by our processing at all depths; this is given by S1Y:Rot in Figure 22. We can well identify a first-order correlation of this fast shear-wave azimuth with the average crack orientation. Possibilities for such real-field positive correlation, even in the scale of a few meters only, of in-situ velocity of the fast-split shear wave with the independently measured orientation of fine-scale cracks, are significant.

The evidence of this clear change in crack orientation occurring around 32 meter depth, where the geology also changes significantly from gneiss to granite, can thus be correlated to the change in the distribution of shear-wave birefringence derived on field seismograms, that we have so far discussed. The three observed correlations between crack distribution and the peculiarities in shear-wave propagation can be summarized as follows.

(1) Correlation of the change in crack orientation around 32 meter depth with a clear, gradual change in the polarization direction of the decoupled shear-waves for S1 source (see S1Y:Rot in Figures 18 and 22). This interpretation is further corroborated by the fact that the phase velocities in the decoupled components of S1, i.e., S1X:Rot and S1Y:Rot (Figure 15) does not show any change with depth, which is because our processing has succeeded to decouple the fast and slow modes at all depths by rotating the two horizontal components to these two directions. Thus, S1Y:Rot, which is aligned close to the crack strike, possibly represents the "stiff" direction of the medium in the horizontal plane; S1X:Rot, being almost orthogonal to the general strike of the cracks, is possibly the "weak" direction.

(2) Correlation of the change in crack orientation around 32 meter depth with an apparently sharp change in the phase velocity in S2X:Rot (Figure 16), that we can interpret as to be due to the interference by a slow-split phase generated around 32 meter depth from the source-generated later signal that travels the shallower region as the fast phase. Below 32 meter, because of this additional mixing of the slow phase for the S2 source (whose arrival is evident in the phase alignment), it has not been possible to decouple completely the fast and the slow split modes by our processing; consequently the derived polarization direction for S2 does not manifest the change occurring around 32 meter (Figure 18). This contrasts with the result of good decoupling achieved for the S1 source.

(3) Correlation of the change in crack orientation around 32 meter depth and the behavior of shear-waves propagating from S1 and S2 sources, to the comparative distribution of interval velocity anisotropy below and above 32 meter depth between S1 and S2 sources (Figures 17(a) and 17(b)). We notice that up to around 32 meter depth (i.e., in Zone (1)), the derived anisotropy distributions are very similar between S1 and S2 sources, though the feature that the decoupled Y-component represents the fast direction is not so obvious. But below 32 meter (i.e., Zone (2)) the relation between S1 and S2 is almost

opposite; this is because, though S1Y:Rot gets aligned to the fast direction after our processing, due to the interference of an additional slow phase, S2Y:Rot is not so aligned.

It is apparent that the crack system and hence the effect of crack-induced polarization anisotropy are relatively simple and consistent up to about 32 meter depth, but below that the situation becomes complex. Such fine-scale correlation of the polarization azimuth of the energy-decoupled S-phases with the orientation of individual cracks measured on cores heightens the possibilities for in-situ detection of shear-wave anisotropy.

Incidentally, the observed average orientation of cracks up to 32 meter is close to the direction of the regional compressive stress (WNW-ESE). The crack orientation below 32 meter, though it lies dispersed between N-S and E-W, is relatively close to the regional foliation direction that strikes NNE-SSW. It is possible that the steeply dipping cracks up to the depth of about 32 meter have received a major influence of the regional tectonic stress, particularly the contribution of the highly directive horizontal stress caused by the motion of the active strike-slip fault existing in the immediate vicinity of this test site. In these shallow depths, the effects of tectonic stress might have been strong enough to mask the effects of large-scale geological trend. However, the depth region around 32 meter marks a major change in the stress regime; below this the regional lithological structures might be more influencing in orienting the cracks that have relatively shallow dips. Finally, this variation in crack orientation has affected the shear-wave birefringence of the medium.

(f) Summary of experiment results

(1) We have received good quality, 3-component shear wave seismograms in a borehole drilled through a hard, fractured rock formation. However, the source-complexity generated two orthogonally polarized shear-wave signals for each source, that are separated by a small difference in origin time.

(2) The shear waves split into fast and slow modes in course of their propagation. These fast and slow directions of the medium change with depth. Our proposed processing technique has separated the two orthogonal source generated signals, by rotating the observed horizontal component seismograms to the directions of the incident fast- and slow-split shear waves at various depths. As a result of processing the phase alignment and the shape of the waveforms have significantly been improved.

(3) Our processing has succeeded to identify a clear change in the orientation of the medium symmetry occurring around 32 meter depth. For S1 source, this change is visible in the derived polarization direction. For S2 source, the resolution is good up to about 32 meter, but below 32 meter the interference of an additional slow phase causes difficulty in decoupling the split modes sufficiently. When compared between S1 and S2, the interval velocity anisotropy also exhibits a clear change in pattern below and above 32 meter.

(4) We have carefully measured the dip and the strike of each distinct crack on the cores with the help of borehole TV images. It is found that the orientation of the steeply dipping, natural cracks between depths 13 and 32 meters of the borehole is generally NW-SE, which matches fairly well with our derived orientation of one of the two directions of medium symmetry; we have interpreted this as the fast direction. Below 32 meter, the average crack orientation clearly changes from NW-SE to between N-S and E-W. Very significantly, we find the derived polarization azimuth of the fast shear-wave from the S1 source also to change slowly to the new direction of the cracks. For S2 source, since the processing cannot resolve sufficiently the split phases because of the complicated interference between two source-generated signals, this change is not visible in the polarization direction.

9·2 Field Experiment 2: Hard, Paleozoic, Sedimentary Rock Site, Illinois, USA.

(a) Site characteristics and geology

The Buckhorn test facility is located in the West-Central Illinois, near the town of Kellerville. A simplified geological cross-section of the Illinois basin with reference to the location of our test site is presented in Figure 23. The geology of the Buckhorn site, in stratigraphic sequence from top to bottom, consists of surface glacial deposit underlain by minor Pennsylvanian clastics, Mississippian Keokuk-Burlington limestones, Mississippian and Devonian "Kinderhook" shales, Devonian Cedar Valley argillaceous carbonates, Silurian Kankakee "White Lime" carbonate, and the Maquoketa shales (Figure 24). Porous parts of the Kankakee formation bear oil, and have been the subject of much attention in the past (Saito et al., 1991; Takahashi et al., 1991).

(b) Experimental conditions

Our experiment is carried out on hard, weathered surface. The main field parameters are given in Table 1. Of all 4 experiments that we report in this paper, this is the deepest one. The borehole has iron casing up to 75 meter; this prevents us from carrying out experiments at shallower depths. Also, there is severe hole widening in the silty upper portion (140~161 meter) of the Hannibal shale, which is highly fractured. Consequently, it is not possible to clamp our sonde against the borehole wall here and receive data. The surface glacial deposits are strongly attenuating for seismic energy. To achieve greater energy for the surface-generated shear waves, we have used a heavy (200 kg) iron mass suspended from a derrick to hit the edge of each source plank.

(c) Field data

We have received 3-component seismograms in two depth ranges within the uncased borehole. The depth ranges of our observation are 79 m~139 m (in Keokuk-Burlington limestone) and 162m~240m (in shales of New Albany Group). Figure 25 shows our field observed seismograms after source time correction and 5~50 Hz bandpass filtering. The shear-wave arrivals are clear and well-aligned. Certain amount of shear-wave energy is visible in the vertical component, although the principal energy is clearly horizontally polarized. The average Vs in the Keokuk-Burlington limestone is between 2 and 3 km/sec, while it is only 1.1~1.2 km/sec in the New Albany shales. Another clear observation is that, when we compare the horizontal-component seismograms between the two orthogonal sources, there is slightly more shear-wave

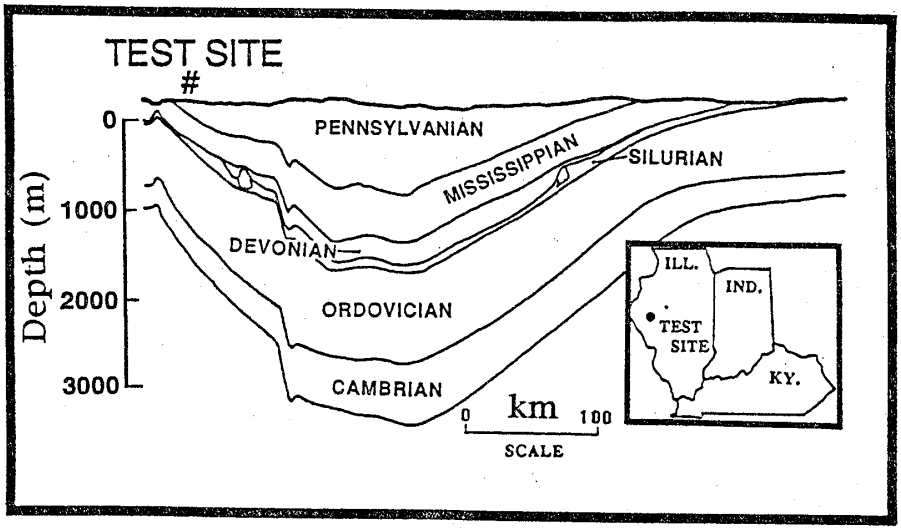

Figure 23. Field Experiment 2: A schematic cross-section of the Illinois basin (after Illinois Geological Society and cooperating organizations); our test site is located on the western flank of the basin.

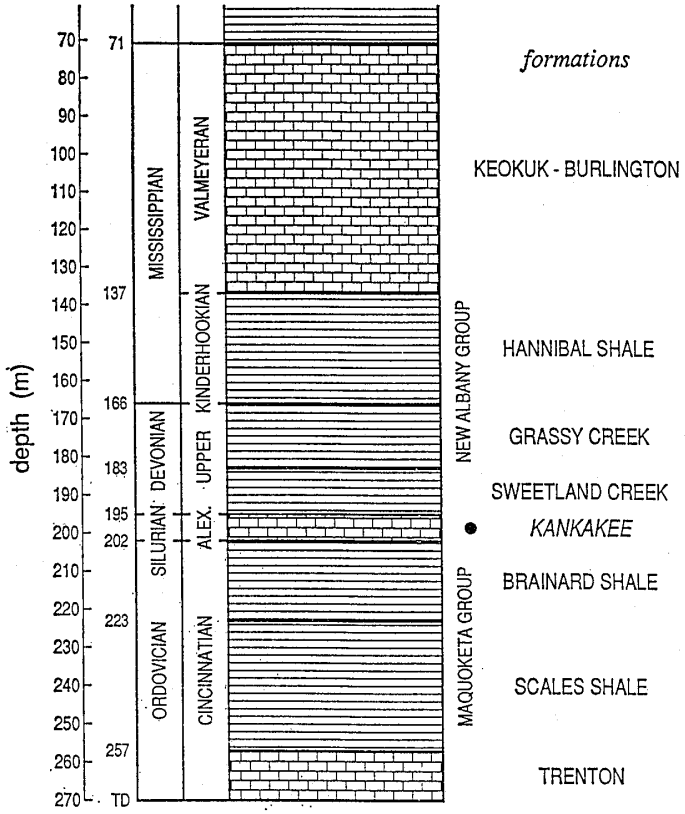

Figure 24. Field Experiment 2: Detailed stratigraphic sequence of the subsurface formations (between 60 and 270 meters) at our test site. Our experiment is carried out between 79 and 139 meter, and between 162 and 204 meter depths.

energy in the Y-component for source S1 and in the X-component for source S2, and this difference increases with depth, particularly within the New Albany shales. Since the two horizontal components of the geophone at all depths are oriented at 45° from the two source polarizations, this is not expected unless there is some degree of vertical shear-wave birefringence in the medium that causes a gradual change in the orientation of the medium symmetry with depth.

(d) Results of processing

The data processing has been done following the technique described earlier (Figure 7) and illustrated in details for Field Experiment 1. However compared to Field Experiment 1, since the source motion is relatively simple here, we used a much wider (30 msec) time window for energy minimization. The location of the time window has been chosen by polarization analysis. We have verified the efficiency of energy-decoupling on this dataset too (i.e., equivalent result of Figure 14), and have found that the convergence is sharp. The estimated rotation angles for energy-minimization and the derived polarization azimuths have small error bars ($<\pm 2°$).

For S1 and S2 sources the processing has been performed independently. For S1 source energy-minimization has been carried out on the X-component records, while for S2 it has been done on the Y-component records. Figure 26 shows the energy-decoupled X- and Y-component seismograms for the S1 source (i.e., S1Y:Rot and S1X:Rot). It is evident that the processing has successfully focused almost all energy to the Y-component. The result is same for S2 too, for which all energy has been focused into the X-component. Compared to the observed seismograms (Figure 25), the shape of waveforms after energy-decoupling has become much uniform at all depths and improved. There is negligible cross-component energy left over after the energy-minimization processing.

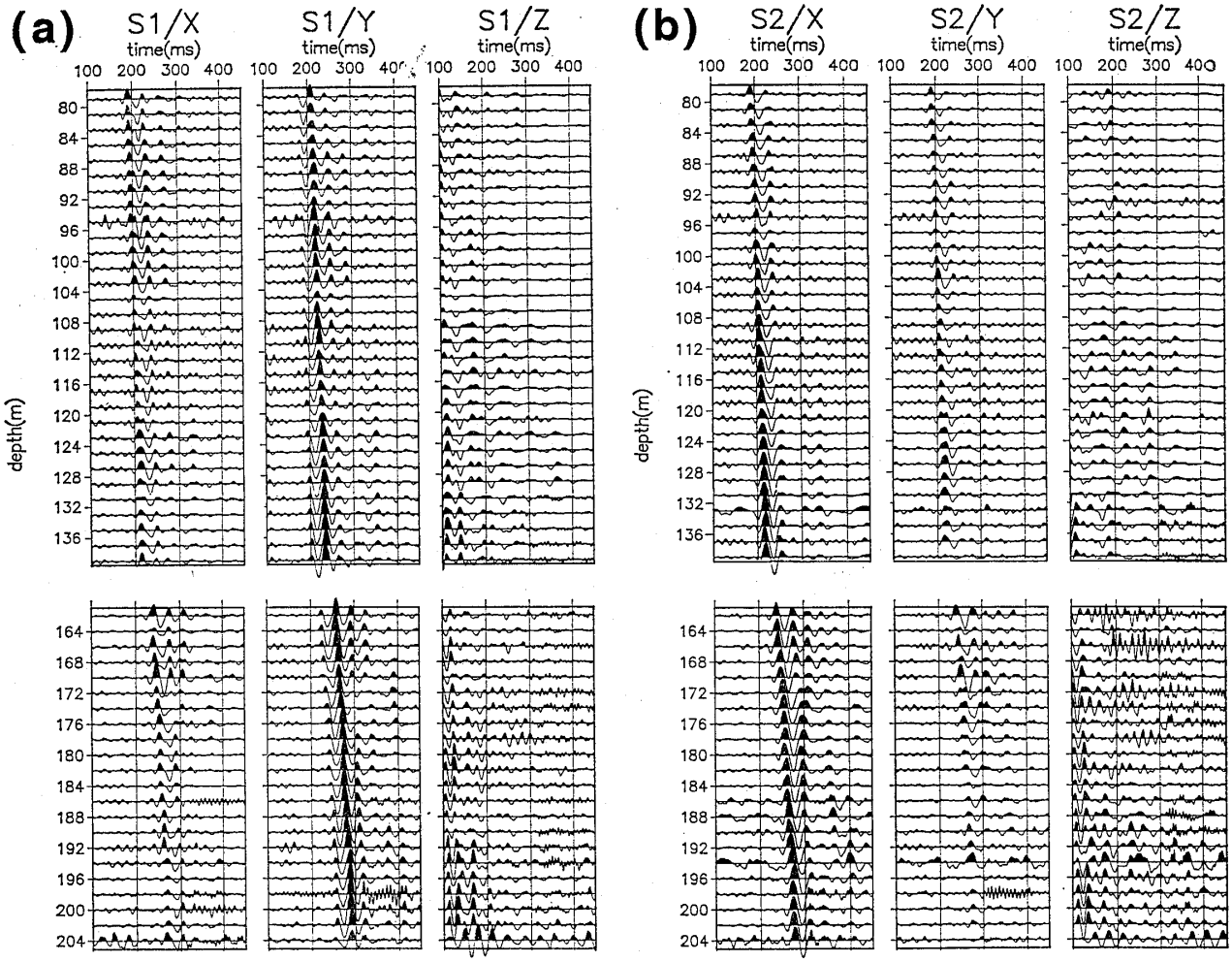

Figure 25. Field Experiment 2: 3-component shear-wave seismograms for S1 and S2 sources ((a) and (b), respectively), after 5~50 Hz bandpass filtering and correction for any source-time variation; X-, Y- and Z-component traces at each depth are normalized relative to the maximum amplitude in them.

From the knowledge of the orientation of the inhole horizontal component geophones, we have converted the angle of rotation necessary for energy-minimization at each depth to the absolute azimuths. Figure 27 shows the depth distribution of polarization azimuth for S1Y:Rot (solid line) and S2X:Rot (dashed line). The source polarizations for S1 and S2 are E-W and N-S, respectively. We notice that within the Keokuk-Burliohton limestone (in 79~139 meter depth range of our observation), the predominant polarization of the received SH wave is not too deviated from the source polarization for both S1 and S2. However, the polarization direction observed within the Grassy Creek and Sweetland Creek shales (in 162~195 meter depth range) is clearly rotated by about 15°~30° with respect to the source polarization, and this polarization shift in shales tends to increase with depth. This indicates that up to the lower limit of the Keokuk-Burlington limestone there is probably no major depth variation in the orientation of the "stiff" and the "weak" directions of the medium in the horizontal plane. But the fractured Hannibal shale, in which we have failed to receive data owing to hole-widening, is possibly more birefringent, and so are the underlying Grassy Creek and Sweetland Creek shales; consequently the polarization azimuth is altered within the shales relative to the Keokuk-Burlington limestone. The directions of maximum and minimum effective rigidity in horizontal plane are slightly different between the limestone and the shales here, and this is

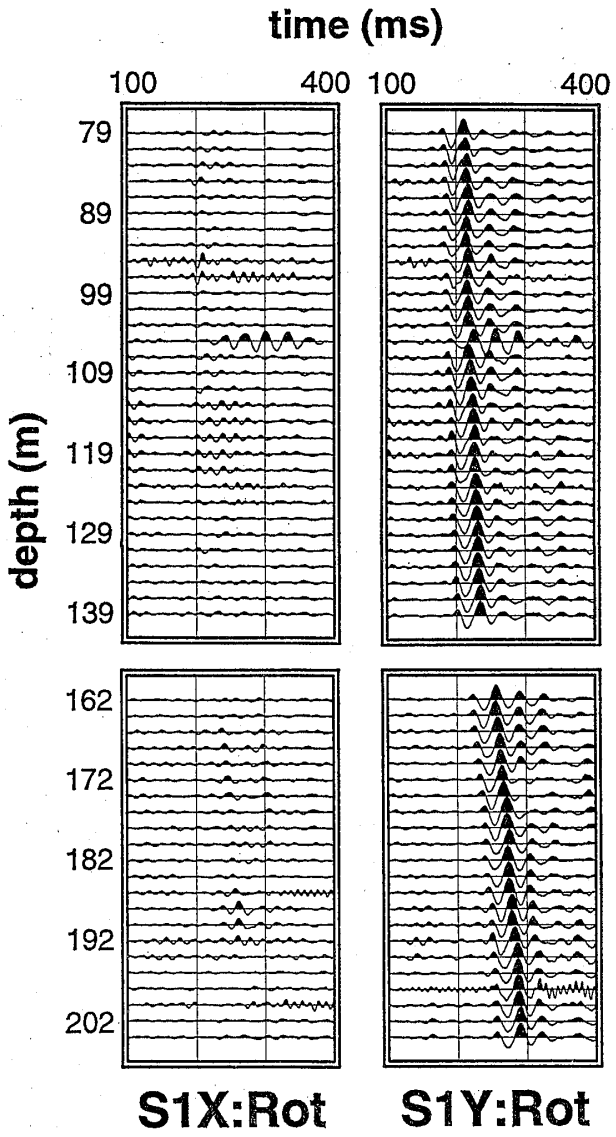

Figure 26. Field Experiment 2: Result of processing illustrated for source S1. The energy-decoupled horizontal components, S1X : Rot and S2X : Rot are shown. The energy has clearly been focused on the rotated Y-component. The rotation angle needed for the energy-decoupling varies with depth and is an indicator of the local orientation of the medium symmetry.

likely to be related to the difference in their internal structures. The two polarization azimuths (S1Y:Rot and S2X:Rot) generally maintain a nearly 90° separation between each other during propagation through the medium. Our solutions for S1 and S2 sources are mutually independent ones. The contribution of noise in our observation is minimal and generally invariant with depth. When observed carefully we notice that the azimuth distributions for S1Y:Rot and S2X:Rot exhibit good mutual correlation; this suggests a common influence of the medium on the propagation of shear waves from both S1 and S2 sources.

From the decoupled seismograms S1Y:Rot and S2X:Rot, we have read digitally a constant phase (peak or trough time) through the entire depth range of our observation. As in Field Experiment 1, we have computed the interval velocity using the difference in phase velocity between S1Y:Rot and S2X:Rot. The derived anisotropy distribution is shown in Figure 28. Here we have used an interval of 8 meter to derive this distribution. Admittedly, our sampling rate of 500 μsec is not high enough to enable attach high credibility to this observed distribution

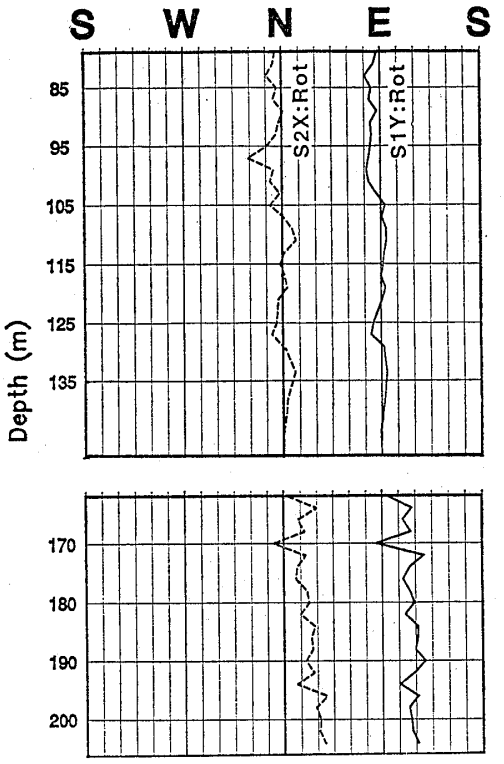

Figure 27. Field Experiment 2: Depth distribution of the polarization azimuth of shear waves in S1Y:Rot and S2X:Rot, calculated from the amount of rotation needed for energy-decoupling at each depth and the predetermined orientation of the X- and Y-component geophones in the borehole, Solutions for sources S1 and S2 (solid and dashed lines, respectively) are mutually independent ones.

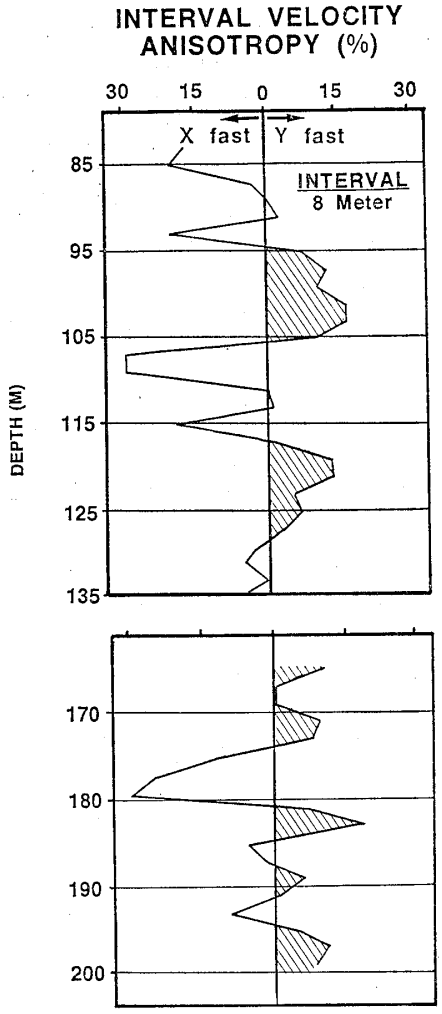

Figure 28. Field Experiment 2: Depth distribution of interval velocity anisotropy.

of the magnitude of anisotropy, particularly when the magnitude is small. It is, however, possible to recognize some gross pattern in the depth distribution of interval velocity anisotropy, or of the magnitude of birefringence. The magnitude of birefringence is generally around 10 % or less, when averaged over 8 meters. Secondly, in the depth range of 79~139 meter, that corresponds to the Keokuk-Burlington limestone, the polarization azimuth S2X:Rot possibly represent the fast direction of the medium in horizontal plane except around 95~105 meter and 117~120 meter depths. Among the New Albany Group of shales, the Grassy Creek shale located around 175~182 meter is most anisotropic; excepting this part, in majority of depths within the shales S1Y:Rot generally represents the fast direction.

(e) Discussion: correlation with other independent observations

We have obtained some high quality geophysical logs in the same borehole to see if our observed anisotropy exhibits causal correlation with other physical properties. In Figure 29, we present a composite picture illustrating geology, apparent resistivity, V_P and V_S determined by suspension P—S logging (which is a measurement technique of interval seismic velocities in borehole from high density and high frequency data received with a sonde containing a seismic source and two receivers placed at 1 meter separation; see Ogura et al. (1988) for details), porosity, and natural γ-ray counts, along with our estimated distribution of the polarization azimuths of S1Y:Rot and S2X:Rot, and the interval velocity anisotropy.

It is possible to correlate in Figure 29 our estimated parameters of anisotropy to other independently determined medium properties. Between 95 and 105 meters, we notice the significant presence of cherty limestone; the apparent resistivity is relatively high here. We find that the interval velocity anisotropy is relatively high (~10%) here, with S1Y:Rot possibly the fast direction — a visible difference from the depths above and below; the polarization azimuth also shows a slight but clear change around 95 meter. It is known that cherts contain subvertical fractures and have higher fissility. We anticipate that the observed change in shear-wave birefringence (in magnitude and orientation) is related to the effective anisotropy of the cherty limestone. The other narrow depth zone located around 117~120 meter is also special in its dolomitic composition; we do not find dolomites in other depths. The apparent resistivity is also relatively high here. We notice 5~10% interval velocity anisotropy, with again S1X:Rot possibly representing locally the fast shear-wave azimuth.

Within the New Albany shales located beween 137 and 195 meters, and constituted of the Hannibal shale (137~166 meter), the Grassy Creek shale (166~183 meter), and the Sweetland Creek shale (183~195 meter), a part (175~181 meter) of the Grassy Creek shale indicates relatively high (15%~20%) shear-wave birefringence. We observe some clear changes in other physical properties in this part of the Grassy Creek shale, e.g., changes in apparent resistivity, V_P, natural γ-ray counts, etc. (Figure 29). Within the Kankakee limestone (195~202 meter), which is a potential source-rock for hydrocarbons, the derived polarization azimuth exhibits some characteristic trend which may be meaningful. Kankakee is well-known for its relatively high fracture density; subvertical fractures may create the change that we observe here. Since we do not have data beyond this depth, it is not possible to confirm if the observed trend is particularly representative of the Kankakee formation or not. Unfortunately in our experiment, the

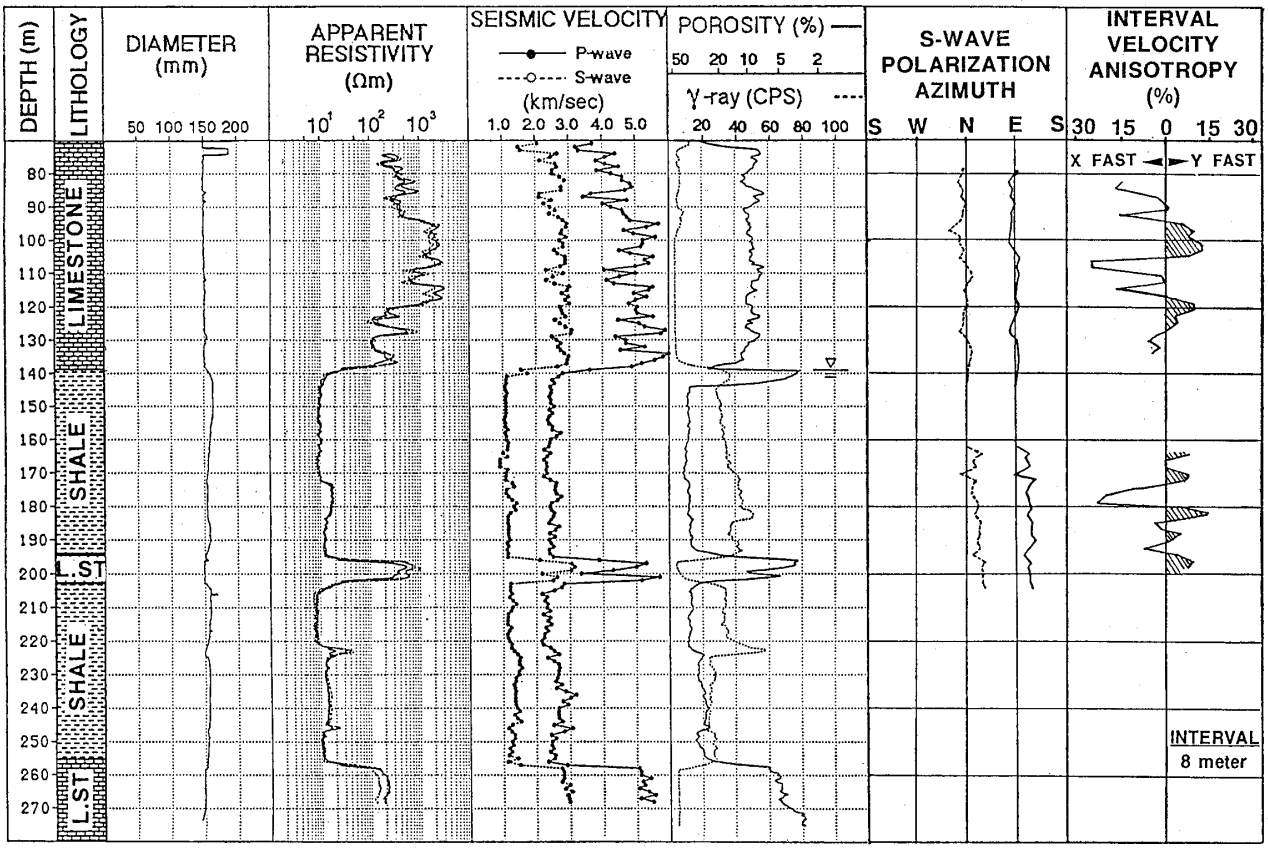

Figure 29. Field Experiment 2: Depth distribution of the physical properties of the underground obtained from the detailed geophysical logs, compared with the distribution of the polarization azimuth of shear waves. See in text for details.

data sampling lacks the density that is required to clearly resolve many features of the reported anisotropy, hence a few of the possible correlations might appear fortuitous. Nevertheless, the clear observation of conformity between the distribution of the parameters of anisotropy and that of a number of independently measured physical properties is causally significant.

(f) Summary of experiment results

(1) We have received 3-component shear-wave seismograms in Mississippian limestone (79~139 meter), in Silurian-Devonian shale (62~195 meter), and in Silurian limestone (195~202 meter), within a borehole drilled in a hard-rock sedimentary basin. Though our key objective is to assess the implications of shear-wave birefringence in geotechnical engineering, this relatively deep experiment is meant to shed light on the relation of shear-wave anisotropy to the broad lithological characteristics, in the environment of a matured sedimentary basin. The quality of our field data is good.

(2) Our processing has succeeded to decouple the horizontal component energy. This has resulted in a clear improvement and uniformity in the shape of the decoupled waveforms.

(3) We detect a change in the parameters of vertical shear-wave birefringence between the Keokuk-Burlington limestone (between 79 and 139 meters) and the shales of the New Albany group (between 162 and 195 meters). From surface up to the lower limit of the Keokuk-Burlington limestone, the two directions of the minimum and the maximum stiffness in horizontal plane are possibly oriented about N-S and E-W, i.e., almost undeviated from the directions of initial source polarizations, and N-S is probably the fast or the "stiff" direction for a vertically propagating shear-wave (coincidentally being close to the S2 source polarization direction). However, the polarization directions are rotated by 15°~30° clockwise within the New Albany Group of shales and below. The Kankakee limestone formation underlying the New Albany shales is also likely to possess some characteristic orientation of the vertical birefringence. The magnitude of velocity anisotropy is generally not very high and is less than 10% in most cases, though it may locally be higher at some restricted depth zones. Our data sampling rate is judged not sufficient for delineating the degree of birefringence with significant accuracy.

(4) Some interesting correlations are apparent between the observed parameters of anisotropy (magnitude and orientation) and the rock units characterized by distinctive physical properties and/or internal structures.

9·3 Field Experiment 3: Soft, Quaternary, Subsoil Site, Northern Kanto Plain, Japan.

(a) Site characteristics and geology

The test borehole is located in an urban area about 30 km north of the Tokyo city. The soft subsoil is composed of flat, alternating layers of sand and silt. These are alluvium deposits primarily of Holocene period. In Figure 30, the geology of our test site is shown. The shallow subsurface is devoid of any notable variation in the depositional history. One main purpose of our experiment in this rather uninviting site is to verify if shear wave birefringence in soft subsoils can at all be recognizable with our present abilities, even when the site does not have any special feature in its deposition or in internal structure.

(b) Experimental conditions

The main field parameters are summarized in Table 1. Shear waves have been generated on the surface by plank-hammering. The borehole is entirely cased with vinyl-chloride casing. The two horizontal components (X and Y) of the inhole geophone is always oriented at 45° from the two orthogonal source polarizations (S1 and S2). We have 3-component

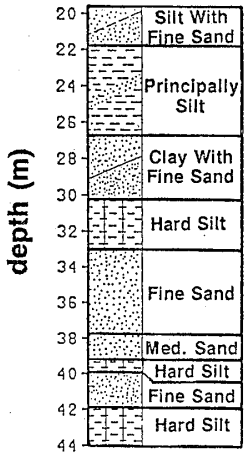

Figure 30. Field Experiemnt 3: Geological column derived from careful analysis of soil samples.

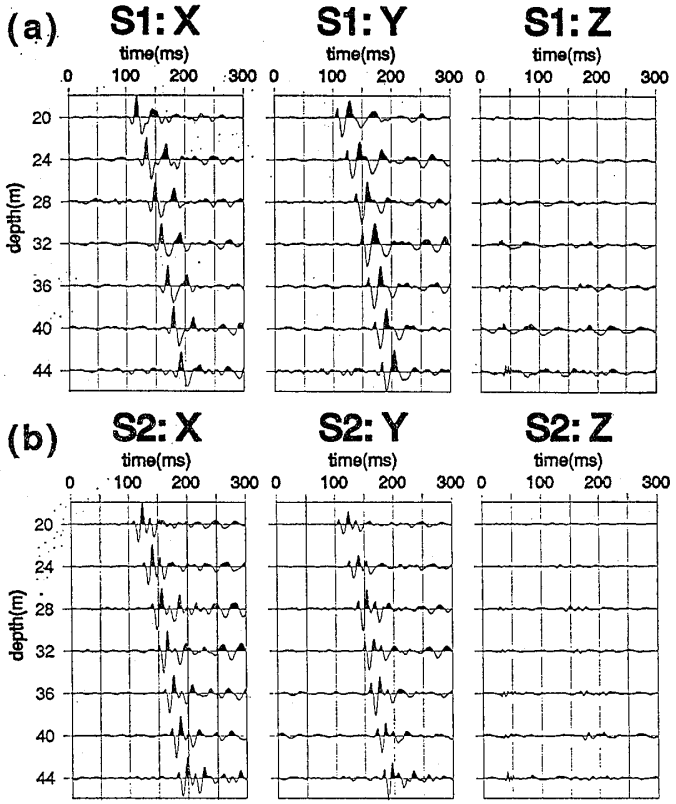

Figure 31. Field Experiment 3: Observed 3-component seismograms after source time corrections, for S1 and S2 sources.

seismograms received at 7 depth levels within the borehole between 20 and 44 meters, at a 4 meter interval.

(c) Field data

Figure 31 shows the observed seismograms after source-time correction and 5～50 Hz bandpass filtering. The signal-to-noise ratio is very good. Unlike Field Experiments 1 and 2, we notice here that the energy distribution in the field data between the two horizontal components is fairly equal, and uniform at various depths. This gives the first-hand impression that there is possibly no significant splitting of the shear wave due to medium anisotropy. There is no energy in the vertical components, indicating that the signal is almost pure SH-wave. The average estimated shear-wave velocity lies between 250 m/sec and 375 m/sec.

(d) Results of processing

The data have been processed following the same flow (Figure 7) as has been used for Field Experiments 1 and 2. Energy-minimization has been done on the X-component traces for source S1 and on the Y-component traces for source S2. The time window for energy minimization is 30 msec wide. The efficiency of energy minimization on this dataset has been checked; it is found that the estimated rotation angles for energy minimization have computation error less than $\pm 2°$. Figure 32 shows the processed X- and Y-component (solid and dashed lines, respectively) seismograms for both S1 and S2 sources. Notice that the shear-wave energy has been well focused in Y- and X-components for S1 and S2 sources (called S1Y:Rot and S2X:Rot) respectively, and it is uniform at all depths. One interesting feature visible after processing is that a little amount of energy consistently remains in the cross-components for both S1 and S2 sources (i.e., in S1X:Rot and S2Y:Rot), that cannot be reduced further by rotation (with whatever relocation of the time window for energy-mini-

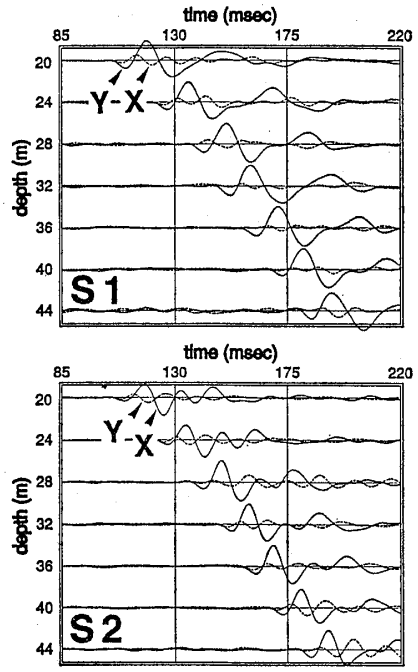

Figure 32. Field Experiment 3: Result of energy-decoupling between the two horizontal components. S1Y:Rot and S1X:Rot, and S2X:Rot and S2Y:Rot, are superposed on each other for comparison. The energy has very efficiently been focused into S1Y:Rot and S2X:Rot, for the two respective sources.

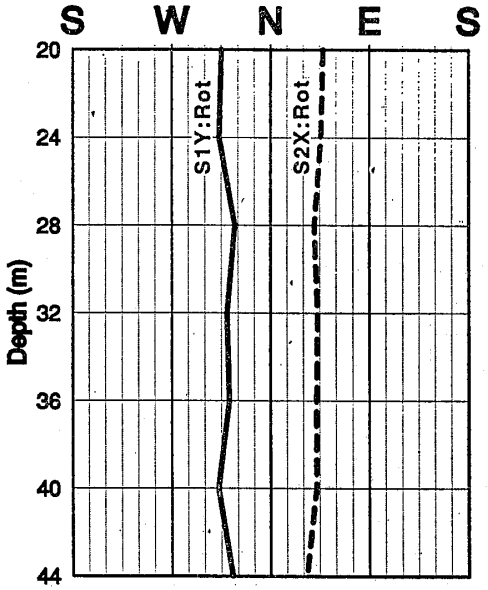

Figure 33. Field Experiment 3: Depth distribution of the polarization azimuth. Polarization directions change little with depth; they are also same as the respective source polarization directions, implying little shear-wave birefringence. of the 4 field experiments, this is the only one that exhibits very little vertical birefringence in shallow surface-formations.

mization). This cross-component phase has shorter wavelength than the main signal, but it travels with the speed of shear wave. It is probably an SV phase generated by the source, that has different frequency than the SH phase. The focusing of the two different S-phases in the two horizontal components illustrates the efficacy of the processing algorithm.

Figure 33 shows the depth distribution of polarization azimuth for S1Y:Rot and S2X:Rot (solid line and dashed line, respectively), which we have derived from the knowledge of the inhole geophone orientations and the angular rotations needed at each observation point for decoupling the shear-wave energy between the two horizontal components. Incident polarizations for S1 and S2 stably align NW and SE respectively, through the entire depth range of our investigation; these azimuths are close to their respective source polarization directions. This suggests that there is little change in shear-wave polarization at this site because the degree of birefringence is possibly small, and/or because our two source polarizations are close to the "fast" and "slow" azimuths of the medium, for the vertically propagating shear wave. When we search for any systematic difference in the phase velocity between the two orthogonally decoupled shear waves, S1Y:Rot and S2X:Rot (and also between the two decoupled horizontal components for the same source, i.e., S1X:Rot and S1Y:Rot, and S2X:Rot and S2Y:Rot), we recognize that the degree of birefringence is indeed small here, so that our data sampling rate (500 μsec) cannot resolve it with confidence and our depth sampling rate cannot delineate any meaningful distribution. The magnitude of average anisotropy does not exceed 5%, a value that we anticipate based on averaging the values at various depth levels.

(e) Discussion: correlation with other independent observations

Within the limit of our acquisition and processing capabilities, the sand/silt subsoil of this experiment site, devoid of any special depositional history and internal structures, does not exhibit any significant shear-wave birefringence. Figure 34 presents a composite picture of lithology, N-value, S-wave velocity from suspension logging, and values of some important elastic properties determined by laboratory testing of soil samples, along with the distribution of the polarization azimuth for two cross-polarized shear waves. We find that although there are some changes in the other medium properties within this depth range (e.g., the transition around 28 meter), there is no prominent change in the polarization azimuth.

The absence of any distinctive expression of vertical birefringence on shear-wave data

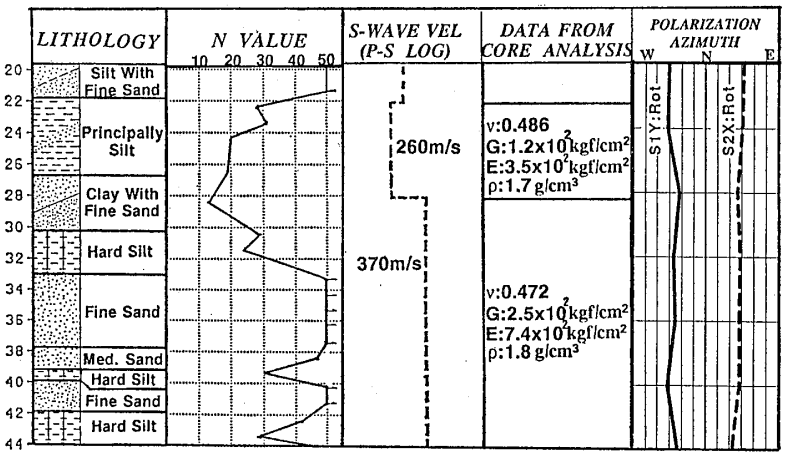

Figure 34. Field Experiment 3: Correlation of other observed parameters with the distribution of the polarization azimuth of shear wave. Though a clear transition in the physical properties takes place between 28 and 32 meters, the age or the depositional environment is constant in this depth range of the soft soil, and we observe also no change in the distribution of any anisotropy here.

here is not due to a coincidental proximity of our source polarization azimuths to the "stiff" and "weak" directions of the medium; but it is because the degree of birefringece is truly small at this site. Compared to the sites of the other three experiments reported in this paper, the present site is least impressive in terms of its depositional history, internal structure, or the anticipated stress regime. We conjecture that, for the occurrence of a measurable amount of shear-wave birefringence in shallow subsoils that can be related meaningfully to the medium properties, the causal influence of depositional environment, structure, and/or dynamic state of the medium, is possibly crucial. Such influences are common in nature. The present test site may, however, stand as an example of a medium notably lacking these influences.

(f) Summary of experiment results

(1) In a soft subsoil formation composed of flat layers of silt, and devoid of any notable variations in depositional history, internal structure, stress distribution, etc., we have received 3-component shear-wave seismograms of good S/N at a number of depth levels in a borehole.

(2) Our processing has been able to successfully decouple the shear-wave energy between the two horizontal components.

(3) Within the limit of our observability, we find little vertical birefringence for shear waves, at this site. The polarization direction also does not show any variation with depth that may reflect the presence of anisotropy. The shear-wave anisotropy may be weak and within a few percent.

(4) For this site, we attribute the lack of observed birefringence to the absence of any major causative facter like stress, or history of deposition under a directional agent, aligned internal structure, etc., that are generally common in most shallow subsoils.

9·4 Field Experiment 4: Soft, Quaternary, Subsoil in a Reclaimed Land-Site, Southern Kanto Plain, Japan.

(a) Site characteristics and geology

The test borehole is located in a reclaimed land-site on the southern edge of the Tokyo city in the Tokyo Bay area. The pressure of further urbanization around the Tokyo megalopolis has already affected this area in last couple of decades and some important civil engineering projects are still planned for future. Placed in the low land flanked by the lower reaches of the Ara River and the delta of the Tama River (Figure 35), the bay-shore has its reclamation works started around 1957~61, using sands from the Tokyo Bay. The topmost 2~3 meters are made of soil carried from the Tokyo city. The reclamation was completed by 1971. The total thickness of the landfill material (sand and soil) at our experiment site is about 8 meters, below which lie the naturally deposited alluvium and diluvium layers of the Quaternary period.

Figure 36 presents the geological column of our test site, formation name and age, and the principal composition of various layers as determined by careful soil sampling from the drill cores. Numerous drill holes are drilled in a regular grid in this site for a very thorough diagnosis of the subsoil condition from an engineering perspective. Underlying the shallow lid of landfill material, the main geologic strata in this area are the Edogawa Formation, the Tokyo Formation and the Upper-Yurakucho Formation. In the entire column shown in Figure 36, there are two main boundaries — one between Edogawa and Tokyo Formations (at around 38~39 meter depth), and the other between Tokyo and Upper-Yurakucho Formations (at around 14~15 meter depth), that represent major change in depositional environment, age, and physical composition of the subsoils. Both these boundaries are marked by the presence of gravel layers derived from buried river

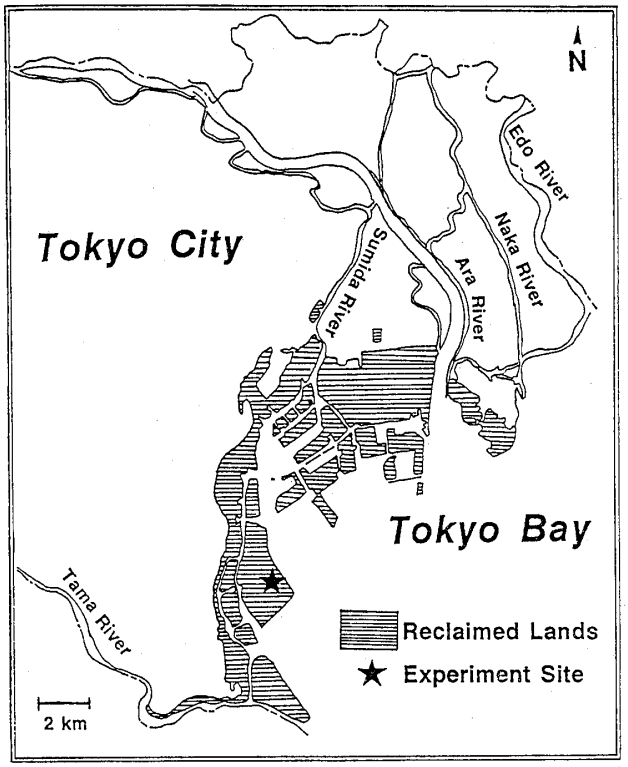

Figure 35. Field Experiment 4: Location of the experiment site in a reclaimed land south of Tokyo. Being at the confluence of a number of rivers, the site is underlain by ancient river-bed deposits.

terraces. In our test hole, we find (Figure 36) the gravel formation, btg, at about 14 meter depth, separating the Tokyo Formation from the Upper-Yurakucho formation. This also defines a major boundary between diluvium of Pleistocene age and alluvium of primarily Holocene age. The physical properties of the soil below and above this boundary sharply differ. The other boundary here, separating the Edogawa Formation from the overlying Tokyo Formation, is also marked by a river-terrace gravel layer (though not intersected by our present borehole), well-known as Tokyo Gravel Formation (Tog). Correlating data from other boreholes surrounding the present test hole, it is found that the 'Tog' formation pinches out just 40~50 meter north of our test hole and its northward thickening is related to a spatial variation of the depositional environment. A humus layer, which normally distributes immediately above the Tog, is present in the geologic column of our test hole (Figure 36), and this here marks the top of the Edogawa Formation and the bottom of the Tokyo Formation. From various analyses involving data from many closely spaced boreholes in the area, it is established that beginning from the 'Tog' downward into the Edogawa formation, the soil properties (grain size, mechanical strength, permeability, etc.) abruptly change from those of the overlying Tokyo Formation.

(b) Experimental conditions

We have carried out the near-offset VSP experiment in a 66 mm diameter borehole drilled in soft subsoil. The principal field parameters are listed in Table 1. Of the 4 field experiments reported in this paper, this experiment has the densest depth sampling; 3-component seismograms have been received in the borehole at an interval of only 50 cm, between depths 5 and 47 meters. The borehole has iron casing only up to 5.5 meter and it is uncased below. Shear waves are generated at surface by plank hammering.

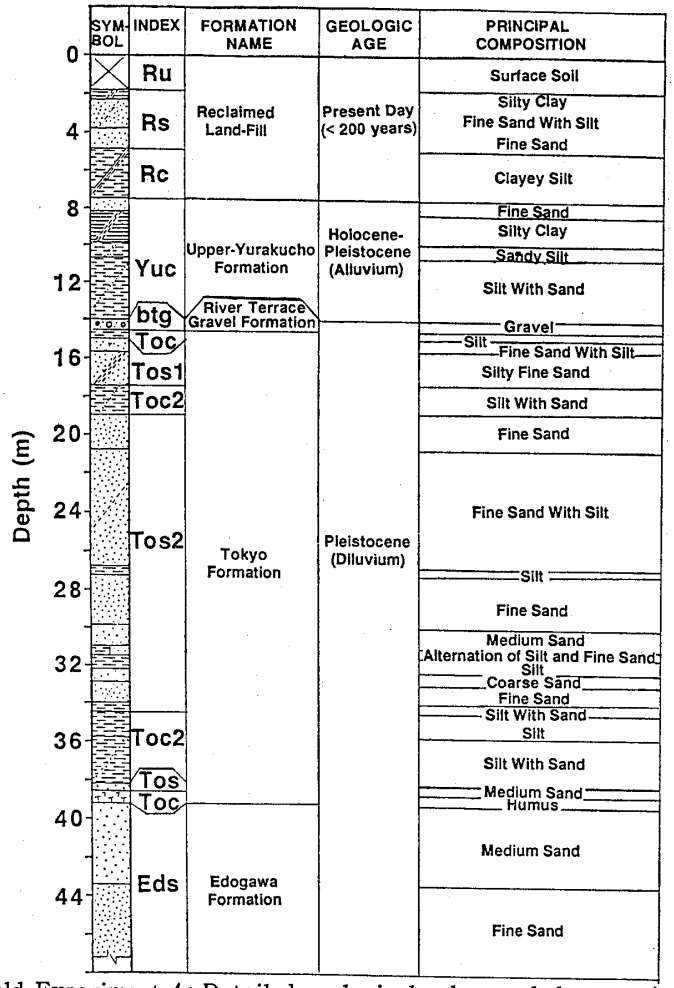

Figure 36. Field Experiment 4: Detailed geological column of the experiment site, derived from careful analyses of the sand samples. The two main boundaries in the naturally deposited sediments are located between the alluvium and the diluvium formations (i.e., around 13~15 meters), and between the Tokyo and the Edogawa formations (i.e., around 38~40 meters).

Data are sampled at every 200 μsec. An instantaneous floating point (IFP) amplifier with a 20 bit resolution is used for data recording. A 3-component geophone is installed at the borehole-mouth for monitoring the source motion and correcting accurately for any source-time variation.

(c) Field data

Figures 37(a) and 37(b) show the observed 3-component seismograms after careful source-time correction and 10~100 Hz bandpass filtering. Note the good signal-to-noise ratio. In such a soft formation and with surface plank-hammer source, it has been possible to receive shear-wave data with frequency exceeding 50 Hz. There is very little compressional- or shear-wave energy in the vertical (Z) component, indicating generation of relatively pure SH-wave, and not much SV or P. There are some later arrivals in the vertical component in the restricted depth range between 12.5 meter and 18.5 meter for both sources S1 and S2; however, the horizontal component seismograms are not much disturbed by them. The sonde-borehole coupling is generally uniform and good, which we have monitored constantly in the field during data acquisition. In this particular experiment we have had the horizontal geophones, X and Y, oriented close to S1 and S2 source orientations, and not at 45° from them as we did in the other

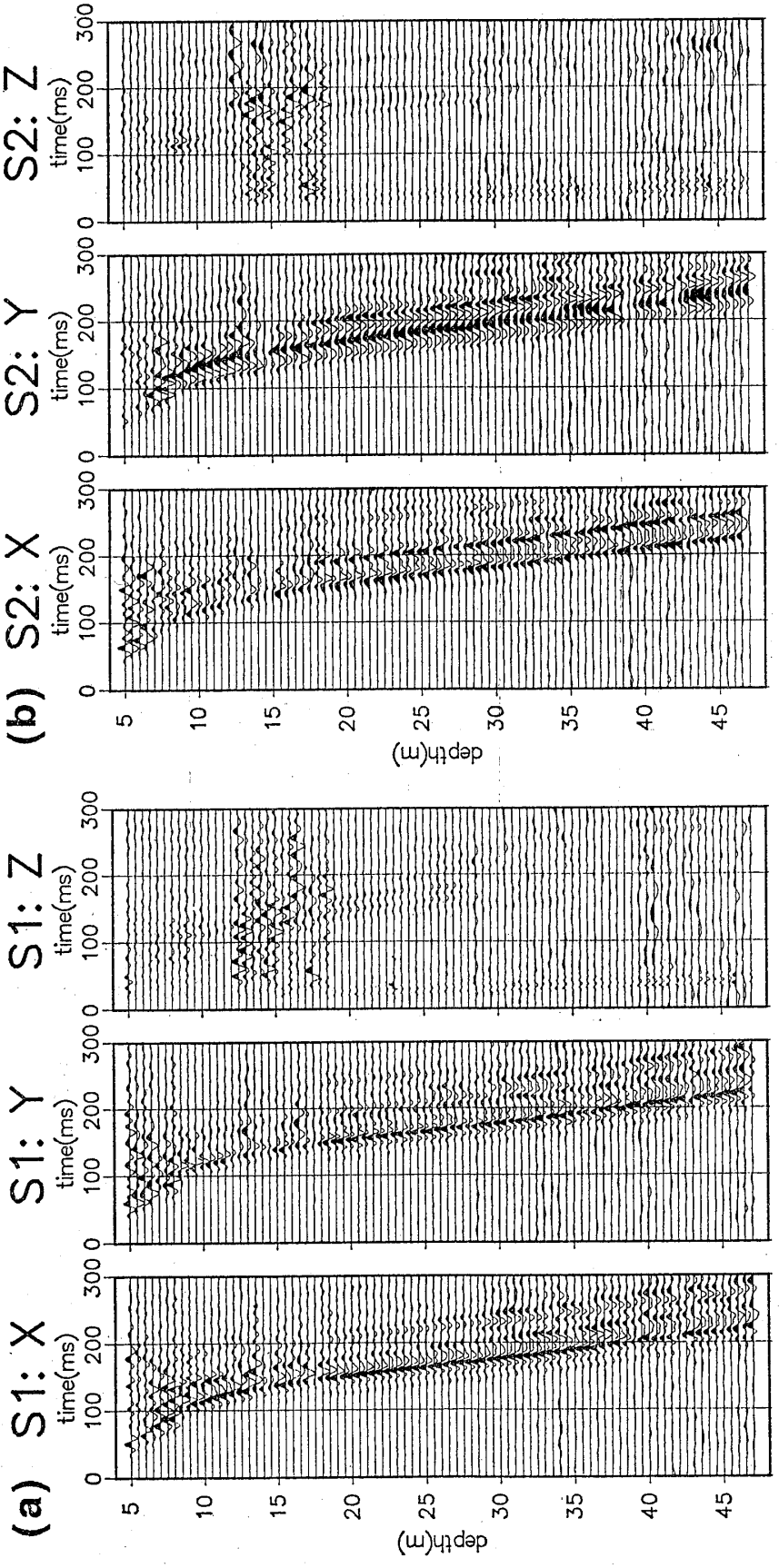

Figure 37. Field Experiment 4: Densely sampled, 3-component seismograms for S1 and S2 sources ((a) and (b), respectively), after 10~100 Hz bandpass filtering and correction for any source-time variation. X-, Y- and Z-component traces at each depth are normalized relative to the maximum amplitude in them.

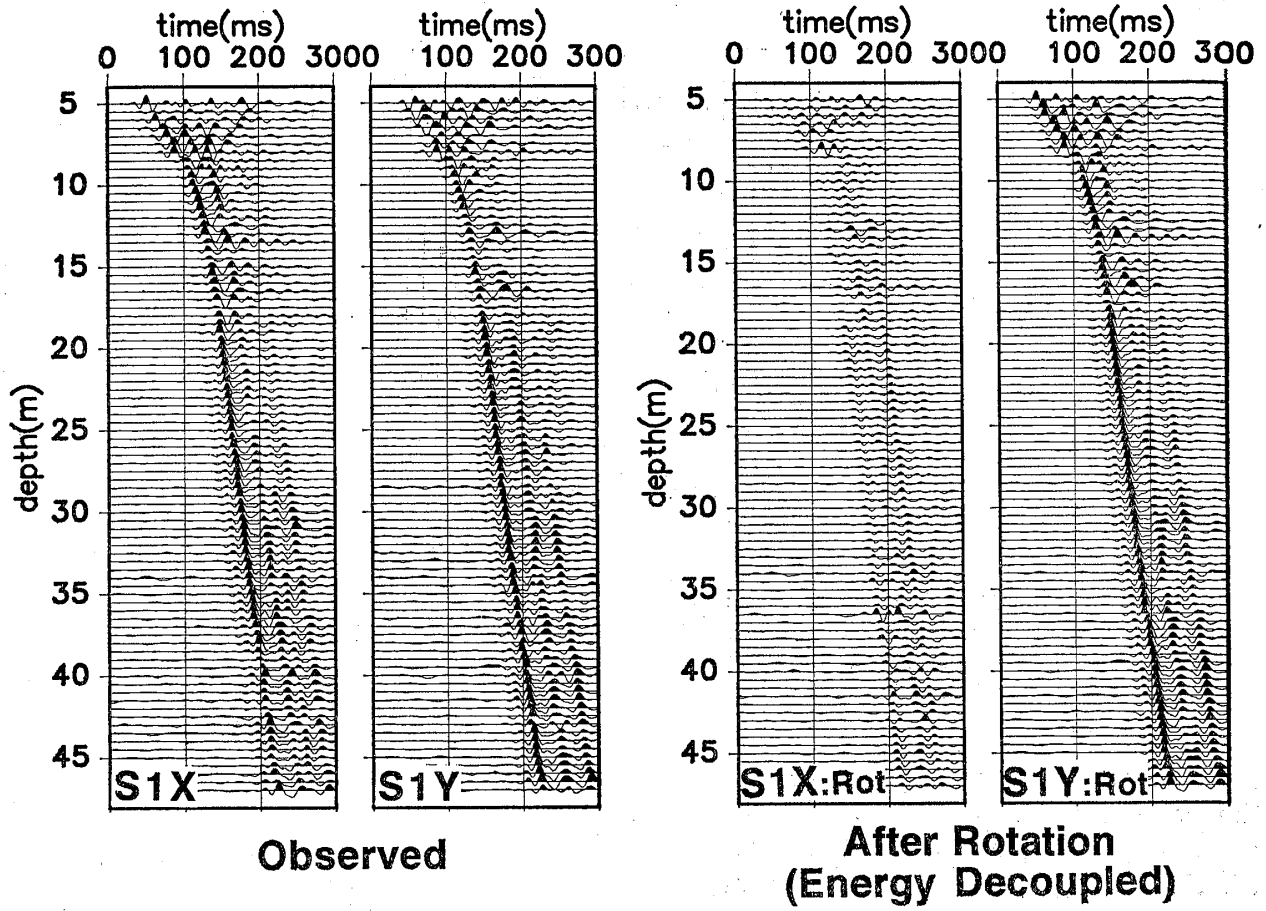

Figure 38. Field Experiment 4: Result of our processing illustrated for the S1 source. Note that the energy is focused well in S1Y:Rot; also note that some shear-wave energy consistently remains in S1X:Rot and this cannot be reduced any further by seismogram rotation.

three experiments. These orientations are strictly maintained constant at all depths of observation. One important feature to note is that, although X- and Y-component geophone orientations are close to S1 and S2 source polarizations respectively, there is significant shear-wave energy in the observed S1:Y and S2:X (Figures 37(a) and 37(b)) right from the very shallow depth levels. This can only be explained by a sharp change at shallow depth of the polarization azimuth of the propagating shear wave, caused by birefringence.

(d) Results of processing

The same algorithm of data processing (Figure 7) has been employed for this dataset. A 30 msec wide time window has been located by polarization analysis of the 3-component seismograms. The efficiency of energy minimization on this dataset has been verified; the convergence is sharp, and the rotation angles for energy minimization are estimated with error bars smaller than $\pm 2°$. Figure 38 illustrates the result of processing for source S1. The result is similar for S2 too, except that for S2 the energy-minimization is carried out on observed Y-component traces, instead of X-components. In Figure 38, the observed X- and Y-component seismograms for S1 source (same as in Figure 37(a)) are shown on the left, for comparison. On the right hand side, the rotated, energy-decoupled X- and Y-components are shown. The necessary rotations for energy-minimization are different for different depths. It is found that the result is stable against slight variation of the window width.

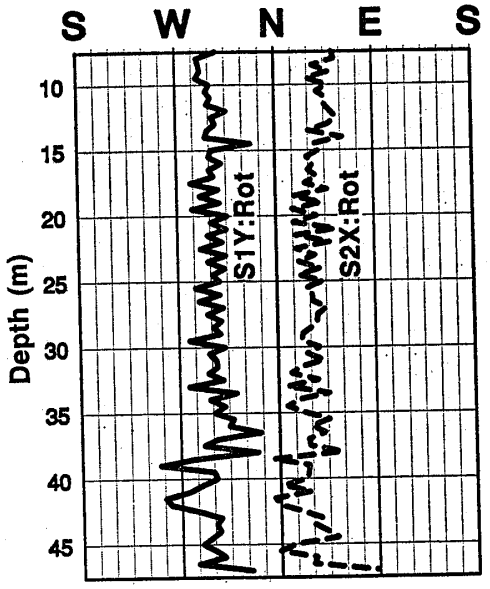

Figure 39. Field Experiment 4: Depth distribution of the shear-wave polarization azimuths. The two solutions, for S1 and S2 sources, are mutually independent. Note the change occurring around 38～39 meters, and also another apparent one around 13～14 meters.

It is evident in Figure 38 that after energy-minimization in X-component, the majority of shear-wave energy has moved to the Y-component (i.e., S1Y:Rot), and the shape of the waveforms has improved. Further, compared to the observed seismograms, the shear-wave amplitude in the rotated seismograms is much uniform in depth, which signifies efficient energy decoupling at each depth. It can also be marked that, though small in amount, some distinct shear-wave energy consistently remains in the rotated X-component (i.e., S1X:Rot). This remaining cross-component energy cannot be reduced any further by trace rotation. We notice that this cross-component phase is relatively small at shallower depths, and its amplitude gradually increases with depth. Secondly, its wavelength is comparable to that in S1Y:Rot. This cross-component S-phase is possibly the split shear-wave phase generated by interaction of the medium anisotropy, which has now been decoupled to the Y-component. This is not likely to be a source-generated SV phase, as we have seen in Experiment 3 for which the wavelength is much shorter than the S-phase in the main component. For S2 source too, the energy minimization in Y-component results in a clear and uniform energy-decoupling between X and Y components, and some minor but consistent shear-wave energy remaining in the rotated Y-component.

From the knowledge of the azimuth of the inhole geophone components (which is predetermined in our experiment) and the angular rotations needed to decouple the shear-wave energy between the two horizontal components, we have derived the polarization azimuth of the decoupled shear-waves, for S1 and S2 sources independently. Figure 39 shows the depth distributions of shear-wave polarization in S1Y:Rot (solid line) and S2X:Rot (dashed line). Though the processing has been carried out independently for S1 and S2 sources, it is clear at first sight that the post-rotated azimuths of S1Y:Rot and S2X:Rot are well maintaining an angle of 90° between them at all depths, and their distributions exhibit good mutual correlation. S1Y:Rot is generally distributed between N50°W and N60°W, while S2X:Rot lies between N30°E and N20°E. One interesting fact to recall here is that the polarization directions of S1 and S2 sources at surface are N20°W and N70°E, respectively. This implies that in course of propagation

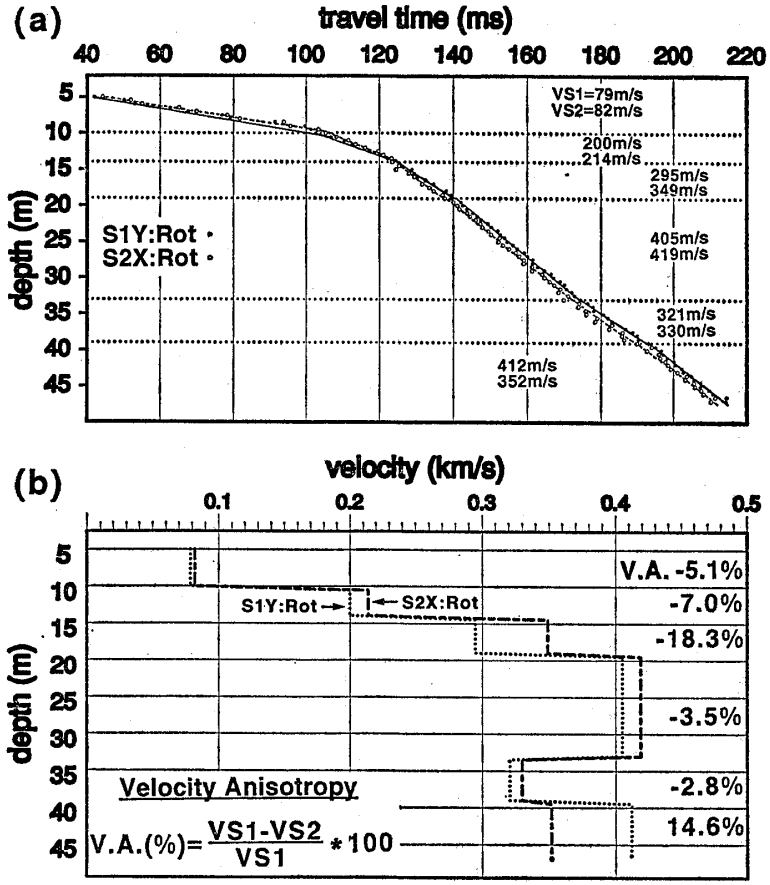

Figure 40. Field Experiment 4 : (a) The digitally read arrival time of the peak shear-wave phase in the energy-decoupled seismograms (S1Y:Rot and S2X:Rot) for the two sources and the eye-estimated velocities. Note the large velocity anisotropy between 14 and 19 meters and that below 38~39 meters (for the latter, the phase in S1Y:Rot is faster than that in S1X:Rot, unlike in the shallower depths). (b) Comparison of eye-estimated phase velocities for the perpendicularly polarized shear-waves (in S1Y:Rot and S2X:Rot) and estimation of velocity anisotropy.

through the first 7 meters of the subsoil, the polarization azimuth of the shear waves from both S1 and S2 sources has rotated anticlockwise by nearly 30°~40°. This is a good indication that the shallow subsoil layers possibly have high vertical birefringence, and that our derived azimuths of S1Y:Rot and S2X:Rot represent the two directions of velocity extrema (i.e., fast and slow directions) for a vertically propagating shear wave. We also notice a clear, split energy in the cross-components. Although these two directions vary with depth, they maintain the orthogonality between each other.

The most prominent change in the polarization azimuth, visible in both S1Y:Rot and S2X:Rot (Figure 39), takes place at around 38~39 meter depth, when both of them rotate anticlockwise by 30° to 40°. We confirmed the repeatability of our observations at a number of depths. The error in our inhole geophone orientation is within 5°~12°. Considering all possible sources of errors, the maximum error bar can be placed at ±10° This makes it difficult to attach meaning to the small fluctuations seen in S1Y:Rot and S2X:Rot polarization azimuths (Figure 39), though their overall trends are surely significant. The large azimuthal variations in the general trend recognizable in both S1Y:Rot and S2X:Rot, such as the one occurring at around 38~39 meter, are truly

meaningful. The mutually perpendicular polarization azimuths of S1Y:Rot and S2X:Rot possibly represent the directions of maximum and minimum effective rigidity of the subsoil medium.

The peak-time of the S-phase in the rotated, energy-decoupled seismograms for both S1 and S2 sources is digitally read. In Figure 40(a) these peak phase-arrival times read from S1Y:Rot and S2X:Rot (black dots and open circles, respectively) are plotted against depth. Here the time axis is much stretched for convenience of examining the relative location of each single data point. There is noise due to scattering. However, there are some meaningful variations too that might be caused by the medium anisotropy. It is worthwhile to look for any statistical trend in the distribution of the difference in interval phase velocity of shear wave between S1Y:Rot and S2X:Rot, that may emerge meaningful.

In Figure 40(a) we have drawn the average traveltime-depth curves by eye approximation. Here the solid line is the traveltime-depth curve for the peak phase arrival in S1Y:Rot, and the dashed line is for the same in S2X:Rot. It is possible to locate five depth boundaries where the traveltime-depth curves for both S1Y:Rot and S2X:Rot appear to exhibit clear changes in slope. The depths of these velocity boundaries also match with those recommended by a separate, routine VSP survey that has been carried out using the same borehole. The average velocity in each layer calculated from the slope of the traveltime-depth curves for S1Y:Rot and S2X:Rot is labeled in Figure 40(a) and plotted in Figure 40(b). The polarization azimuths of S1Y:Rot and S2X:Rot are almost

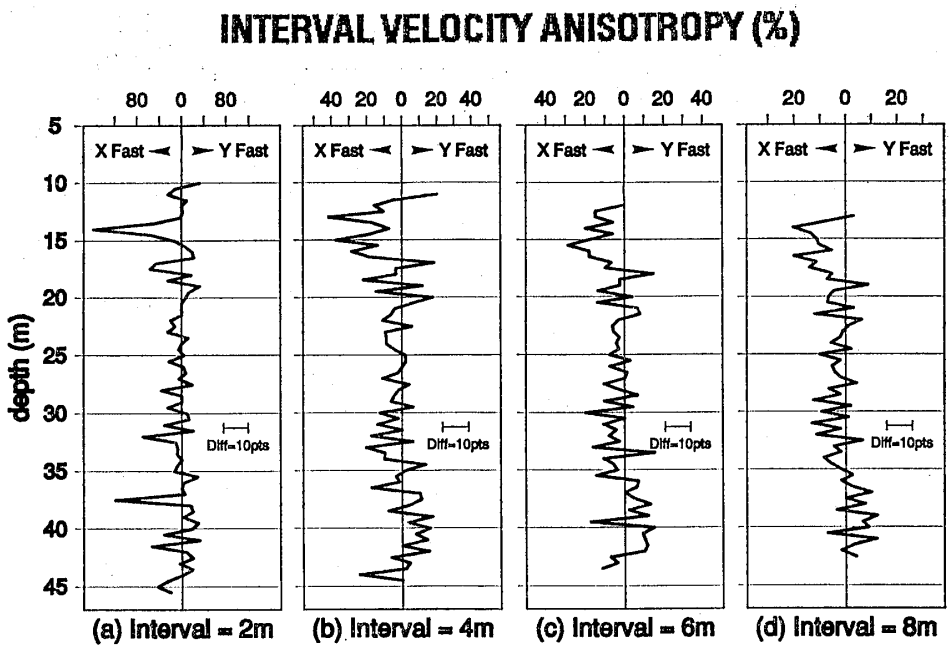

Figure 41. Field Experiment 4: Depth distribution of the interval velocity anisotropy, estimated digitally for 4 different depth intervals of averaging and using the energy-decoupled S1Y:Rot and S2X:Rot seismograms. Observe that the major trend of the distribution is visible consistently in all 4 averaging scales, though the degree of the observed anisotropy decreases with increase of the averaging interval. High magnitudes of anisotropy (20% or more) are seen around depths 12~17 meters and possibly below 38~39 meter, the exact depths are slightly shifted as the calculated values are plotted always at the center of the sliding interval. Note also that below 38~39 meters the S-phase in Y-component clearly travels faster than that in X-component, a relation that is opposite at shallower depths.

orthogonal to each other (Figure 39); their velocity difference reflects the magnitude of the average vertical birefringence. The percentage vertical birefringence, or the velocity anisotropy, is marked in Figure 40(b) for each velocity layer. The absolute value of birefringence varies within a wide range, between 3% and 18%. The two depth zones that clearly exhibit significant velocity anisotropy are located around 14~19 meter and below 39 meter; the phase alignments are generally good in these zones. Another interesting observation is that up to about 39 meter, the shear wave phase velocity in S2X:Rot is always faster than that in S1Y:Rot, thus giving negative values of anisotropy in Figure 40(b); but below this depth the relation becomes opposite, i.e., S1Y:Rot represents the fast direction and S2X:Rot the slow direction.

The test site is composed of many thin layers (Figure 36) of varying physical properties. As we have a dense depth-sampling, it is important to examine with greater care if the fluctuations in the phase arrival time for the two energy-decoupled, cross-polarized, vertically propagating shear waves are random, or they are sensitive to underground physical properties. The eye-estimated traveltime-depth curves (Figure 40(a)) do not help visualize the trend in a realistic, scale-variant way, and can potentially ignore some consistent short-wavelength changes. We have, therefore, calculated the interval velocity anisotropy using different widths of the averaging interval — 2, 4, 6, and 8 meters. They are shown in Figure 41. The sliding depth interval is moved from 5 to 47 meters at 50 cm pitch, and the computed interval velocity anisotropy $[(\Delta t_{S2} - \Delta t_{S1})*100/\Delta t_{S2}$, where Δt represents the difference in traveltime between the two energy-

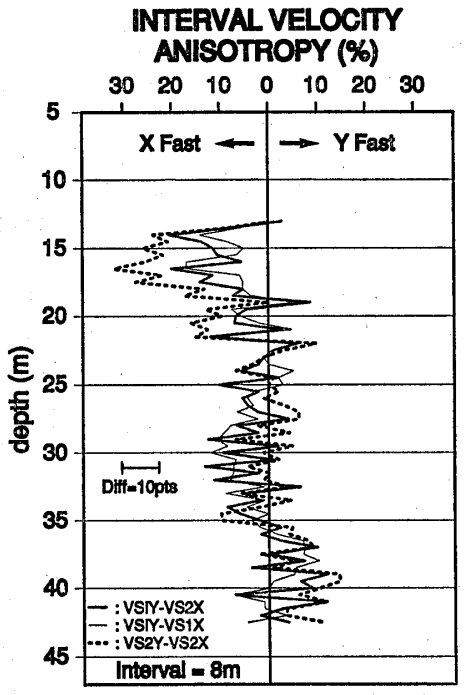

Figure 42. Field Experiment 4: Estimated velocity anisotropy for a 8 meter wide averaging interval. The three lines are for anisotropy calculated using the three different combinations of the orthogonal X and Y components of the energy-decoupled seismograms for the S1 and S2 sources. Though the shear-wave phases in the energy-minimized components (i.e., S1X:Rot and S2X:Rot) are small, they were used to see if any common statistical trend emerges; also two energy-minimized components for the same source helps to see the result without involving the effect of any variation in the characteristics between the two different shear-wave sources.

decoupled seismograms, to travel from the top to the bottom of the sliding depth interval] is plotted at the center of the interval. Interval velocity anisotropy is computed using energydecoupled S1Y:Rot and S2X:Rot seismograms.

The absolute magnitude of the vertical birefringence decreases with increasing averaging interval (Figure 41), which is an obvious result of smoothing out some thin, highly birefringent layers. This illustrates the scale-dependence of the magnitude of the observed birefringence. The magnitude of anisotropy in some thin subsoil layers is truly high. However, it is to be recognized that when the averaging interval becomes shorter, as the true effect of the medium anisotropy (i.e., the signal) tends to be more visible, the influence of the scattered noise also becomes disturbingly high. An objective judgement of the signal level and the noise level is not feasible for each depth point; however given no drastic variation in the reception condition and the data quality, the noise background may be considered relatively constant and uncorrelatable to the subsoil physical condition or geology. Subject to this condition, the depth zones that consistently show a relatively high degree of anisotropy after various depth-averaging (Figure 41), are very likely to be highly anisotropic in reality. It is anticipated that the velocity anisotropy around 13～15 meter, 16～18 meter, and 38～ 40 meter may be as high as 20% or even more.

Another unambiguous feature that can be recognized in Figure 41 is that there is a clear change around 38～39 meter in the polarization azimuth of the fast and slow shear waves. Around this depth the polarization azimuth for both S1 and S2 rotates anticlockwise by 30° to 40° compared to shallower depths, as pointed before. Also in depths shallower than 38～39 meter the decoupled S-phase in the X-component generally travels faster than that in the Y-component, but it becomes reverse below. In other words, for this site the fast azimuth, or the "stiff" direction of the medium for a vertically propagating shear wave, is N30°E to N20°E (Figure 39) at depths shallower than 38～39 meter; however, at depths immediately below this, the fast direction is shifted to nearly E-W or further. This prominent effect of medium anisotropy on shear wave propagation is confirmable on data for both S1 and S2 sources.

It has also been possible to read digitally the peak phase-arrival time for the energy remaining in the energy-decoupled cross-components (i.e., S1X:Rot shown in Figure 38, and S2Y:Rot), which we have interpreted as the split shear-wave modes generated due to the interaction of medium anisotropy. To check the result without incorporating the effect of the difference in source characteristics between S1 and S2 (source coupling, central frequency, etc.), we have calculated the interval velocity anisotropy using the time of the S-phase appearing in the two energy-decoupled horizontal components from a single source. In Figure 42, the thick solid line shows the interval velocity anisotropy obtained by using the travel time of the energy-decoupled S-phase in S1Y:Rot and S2X:Rot for an averaging interval of 8 meters (i.e., same as Figure 41 (d)); the thin solid line represents the distribution of interval velocity anisotropy calculated using the energy-decoupled phases in Y and X components for source S1, and the dashed line represents the distribution of interval velocity anisotropy calculated using the energy-decoupled phases in Y and X components for source S2. It is important to note that all three distributions in Figure 42 exhibit remarkable similarity in the gross trend, signifying uniquely the influence of medium birefringence on shear-wave propagation. This also attaches credibility to our estimated relative magnitude of anisotropy among the various subsoil zones.

(e) Discussion: correlation with other independent observations

There is no direct means to measure accurately the effective rigidity variations

in the horizontal plane at various depths. There are various isolated reports relating shear-wave anisotropy to anisotropic hydraulic, transport or mechanical properties of the medium. As yet there is no general consensus as to the cause of the vertical birefringence. There are a number of proposed models based on the observation of vertical birefringence in field data or in laboratory experiments (e.g., Nur and Simmons (1969); Nur (1971); Crampin et al. (1984)). Whatever the best model proves to be, majority of the earlier reported evidences of vertical shear-wave birefringence have been explained by unequal horizontal stresses. Almost all of these prior field or laboratory tests have been carried out on hard rocks.

The situation is very different in soft, subsoil material at shallow depths where the stress distribution is more complicated and the lateral heterogeneity is intense. In addition, the effects of fluid motion and the geometry of aligned grains and pores in the relatively unconsolidated material are also significant. Unlike the brittle rocks where the crack system plays a major role in anisotropy formation, in argillaceous and marl rocks fracturing is not intensive if at all present; however for the latter, compaction is observed in the direction of maximum compression, thus changing the initial isotropy (Shanov, 1990). Lynn (1991) reviewed the laboratory results of Hardin and Richart (1963), Roesler (1979), and Lee et al. (1986) to discuss the effects of the presence of water in rounded grain and angular grain materials and in-situ stress state on the vertical shear-wave birefringence in soft soil. She proposed that soils in the shallow weathering layer are most birefringent of materials sampled in-situ because soils have the highest

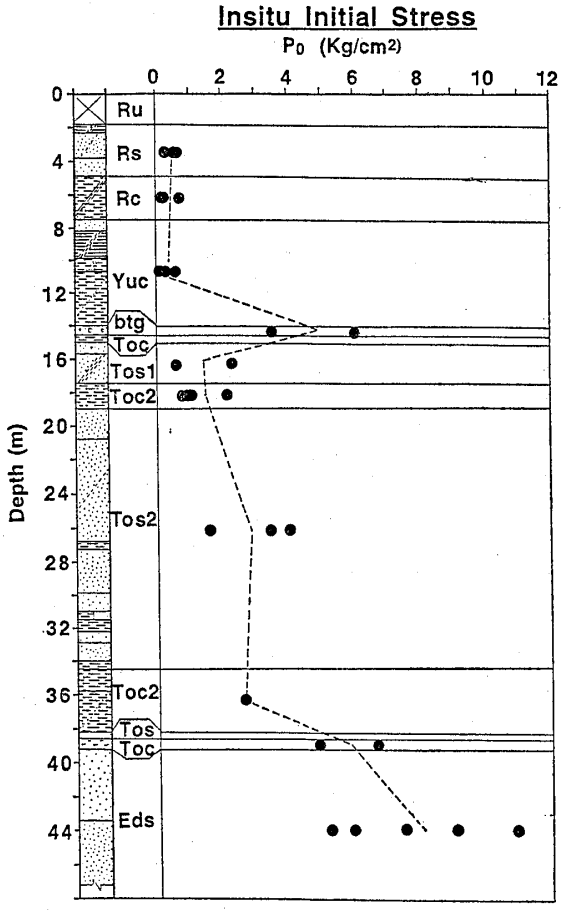

Figure 43. Field Experiment 4: Depth distribution of in-situ initial stress measured in a number of closely spaced boreholes at the same site with the help of the lateral load tester (LLT). See in text for details.

porosity, and thus the largest amount of deformed pore spaces to ellipsoidal shapes by unequal horizontal stresses; these fluid-filled ellipsoidal pore spaces form the microcrack system. Lynn finally attributed her observations of birefringence in the soft subsoil of California to a combination of four possible factors viz. unequal horizontal stress, fabric anisotropy or depositional agent anisotropy, stress-aligned fluid-filled microcracks (EDA), and the boundary effect of the depositional area. Following the equation: $V_s \sim \sigma_a^{0.149} \sigma_P^{0.107} \sigma_S^{0}$ of Roesler (1979) derived from experimental data on sand samples with stress components varying between 4 N/cm^2 and 16 N/cm^2, where σ_a is the stress component in the S-wave propagation direction, σ_P is the stress component in the S-wave polarization direction, and σ_s is the stress component perpendicular to both σ_a and σ_P, a 5%~6% vertical shear-wave birefringence would imply about 58%~72 % anisotropy in horizontal stress, which is very high.

At numerous boreholes in our test site we have reliable data of borehole lateral load tester (LLT), which is a device to measure the in-situ total horizontal stress within a borehole drilled in a soft medium (Ohya et al., 1980). The stress values obtained by LLT measurements are azimuthally averaged values and so unfortunately they do not give any idea about the anisotropic horizontal stress. Figure 43 shows the distribution of initial horizontal stress (P_0) from LLT measurements at various layers at our test site. Multiple stress values for a single layer correspond to measurements at a number of boreholes located within a small area around our test borehole, and they define an approximate range for each layer. At first sight it can be recognized that the average horizontal stress is relatively high around 14~15 m, within the river-terrace gravel (btg) formation that marks the boundary between the alluvium and the diluvium subsoils. The average horizontal stress shows another sharp rise around 39 meter depth which represents the transition from the Tokyo Formation to the Edogawa Formation. The horizontal stress continues to be relatively high within the Edogawa Formation. We notice that the depths that exhibit a clear change in the observed anisotropy distribution (Figures 39 to 42) coincide fairly well with those representing a sharp change in the distribution of the average horizontal stress measured in-situ. If we assume the in-situ anisotropic horizontal stress to be proportional to the magnitude of the observed vertical birefringence (Roesler, 1979; Lee et al; 1986; Lynn, 1991), the only conclusion that can be reached is that in zones of higher average horizontal stress measured by LLT, the contrast between the maximum and the minimum horizontal stresses (σ_H and σ_h) is also higher. Indeed, the gravel formation at around 14~15 meter depth has higher permeability than the layers below and above, and this might contribute to significant directional stress. For a certain depth below 38~39 meter too, there may be a change in directions and in the magnitude of the contrast between σ_H and σ_h, as a downward continuation of the effect of the flow in the inter-formation, river-terrace gravel layer (i.e., in the Tokyo Gravel Formation, sandwiched between the Tokyo Formation and the Edogawa Formation). However, stress anisotropy is surely not the sole reason for our observed vertical birefringence, because the large magnitude (exceeding 20~25%) of the birefringence found at several depths would require some unrealistically high anisotropy in the horizontal stress, and possibly other factors too, in addition to stress, are responsible for it.

In Figure 44, we have correlated our observed vertical birefringence (polarization azimuths and magnitude of the velocity anisotropy) with other independent observations, viz. geology, formation age, suspension P and S logs, and N-value. To compare with the general trend of the magnitude of the interval velocity anisotropy distribution, here we have shown both the eye-estimated velocity distributions, as well as the distribution of the interval velocity ansiotropy numerically estimated from the decoupled S1Y:Rot

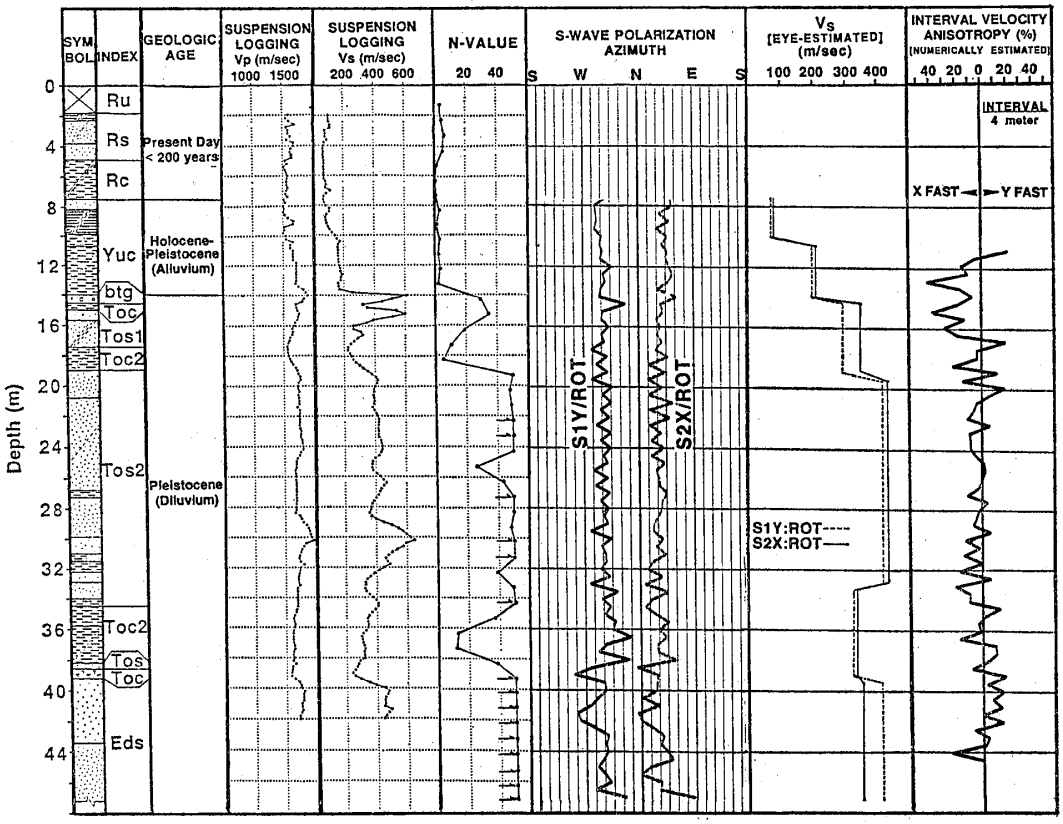

Figure 44. Field Experiment 4: Correlation of the observed distribution of vertical shear-wave birefringence in soft subsoil with other independently determined parameters.

and S2X:Rot seismograms and using a sliding averaging interval of 4 meter.

What is striking here is a good correlation in depth of the observed anisotropy with the other independent parameters. Accordingly, it is possible to identify tentatively at least 4 depth zones, as follows.

(1) Zone(1) (up to 12~13 meter depth): This depth range corresponds to the very soft alluvium deposits of primarily Holocene age, N-value less than 5, V_P=1600~1700 m/sec, and V_S<200 m/sec. The degree of anisotropy is small here and possibly not over 5% (refer Figures 40 and 41 too).

(2) Zone(2) (between 13 and 19 meters): The magnitude of velocity anisotropy is significantly high here and may even be as high as 25%~30%. The boundary between zones (1) and (2) approximately coincides with the boundary between very soft alluvium and slightly consolidated diluvium deposits, and is marked by the presence of the river-terrace gravel formation (btg)— a trail of an ancient river, in which we have also reported a relatively high average horizontal stress (Figure 43) and higher hydraulic permeability. In case of unequal horizontal stresses, the intergranular pore spaces deformed to ellipsoidal shapes might be connected to each other along a line if the grains are also aligned in the direction of the major axis of the pore ellipsoids, and this may create fluid-filled microcracks. In addition to the possibility of an existing contrast between the maximum and the minimum horizontal stresses, it is quite likely that the ancient riverine deposition has influenced the gravel, sand, and silt layers here in making the effective shear modulus in the horizontal plane greater in one direction than in the other.

Within Zone (2), we notice that the degree of anisotropy is maximum around 13～15 meters, and it apparently decreases with depth. This might reflect a spatially varying effect of the depositional environment, with the peak lying around 13～15 meters. The significant vertical birefringence that we observe in Zone (2) is possibly a combined effect of the causes mentioned earlier; among them the contribution of the riverine depositional environment appears more important than the others. In Zone (2) we also notice that the V_S abruptly increases from less than 200 m/sec to 500～600 m/sec, and the N-value increases from less than 5 to over 30. This highly anisotropic zone is consistently visible in all scales of depth averaging (Figure 41).

(3) Zone (3) (between 19 and 38 meters): The magnitude of velocity anisotropy is relatively small here and probably within 5%～8%. This zone, comprising of more consclidated diluvium deposits of the Tokyo Formation, exhibits consistently higher V_S and N-value than Zone (2). But the variation of these properties within the zone is not large, and the zone is quite uniform in composition (mainly sand, see Figure 36) and in the age of deposition too. The environment has remained constant during the deposition of these sand layers, and directional agents like stress or flow have not been important.

(4) Zone (4) (between 38 and 47 meters): This zone is made of medium to fine sand. A clear and sharp change in the orientation of the fast and the slow directions of the medium in the horizontal plane takes place here. This is visible in the depth distribution of the polarization azimuths determined independently for the two sources, S1 and S2. In this depth zone, the S-energy arriving in the decoupled Y-component and polarized in the direction N80°W～N100°W travels faster than that arriving in the decoupled X-component and polarized N10°E～N5°W. The top of this depth zone corresponds to the top layer of the Edogawa Formation (Figure 44), which is located immediately below the Tokyo Formation and the Tokyo Gravel Formation (the latter narrowly not intersecting our borehole).

The lower end of the Tokyo Formation designates a big change in the depositional column and the depositional history. Up to this boundary (located at 38～39 meter depth), we observe negative velocity anisotropy in shallower depths (Figures 40 and 41) i.e., the energy-decoupled S-phase arriving in the X-component and polarized on an average in the direction N30°E～N20°E travels faster than that in the Y-component which is polarized N50°W～N60°W. The boundary around 38～39 meter depth denotes a change in the depositional environment, significant increases in compaction (N-value exceeding 50 in the deeper region), V_P and V_S (exceeding 1750 m/sec and 450 m/sec, respectively), and average horizontal stress (Figure 43). The inter-formational river-terrace gravel layer also appears here. The humus, the gravel (not intersected by our borehole), and the underlying layer of medium-size sand (Figure 36) have possibly received the influence of the riverine deposition, as discussed earlier for Zone (2).

Detailed geotechnical investigation of the Edogawa Formation has also revealed that the variation of the water level in it during lunar attraction or during artificial pumping is laterally uniform, thus indicating good hydraulic permeability. However, the directivity of these factors (e.g., flow, stress, permeability, etc.) that have affected the deposition in Zone (4) is possibly drastically different from that at shallower depths (up to 38～39 meter).

From the correlation of the geologic logs obtained from numerous boreholes at this site, it is known that up to the bottom of the Tokyo Formation the attitude of the layers at the shallower depths is strictly horizontal. But there is a northward gradient (depth increasing) for the top of the Edogawa Formation. This results in southward

thinning of the intermediate Tokyo Gravel Formation (and pinching out of it 40～50 meter north of the present test hole). The layers hardly show any dip in the E-W direction. Such disparity between the N-S (dipping) and the E-W (horizontal) attitudes of the layers below Tokyo Formation suggests that prior to this period there was a more prominent variation in the depositional gradient between N-S and E-W directions. If the ancient river channel had its flow nearly in the E-W direction, and if the N-S corresponded the direction across, thus producing short wavelength attitudinal variation only in the E-W, then it is likely that in the direction of the flow the grain-to-grain strength would be higher and in the orthogonal direction it would be less. Also in such stress regime, the fluid-filled microcracks aligned in the E-W direction may form. For the depth range between 39 and 44 meters, which is possibly the depth range that has been more influenced by the riverine depositional environment, these might be the main reasons for the maximum effective rigidity to be E-W and the minimum effective rigidity to be approximately N-S, as is reflected in the fast and the slow polarization azimuths of the vertically propagating shear waves.

The observed anisotropy and its interesting depth distribution are probably, therefore, the results of a number of factors — horizontal stress difference that might be related at certain depths to the direction of hydraulic permeability, alignment of grains and/or pores by the influence of depositional agent, viz. river flow (and the high anisotropic zones remarkably corresponding to the layers that are closely below the ancient river beds) and in-situ stress, and fluid-filled microcracks.

(f) Summary of experiment results

(1) We have obtained good quality, 3-component shear-wave seismograms in a shallow borehole drilled in soft sandy subsoils of a reclaimed land-site. The high rates of depth sampling and data sampling have made the dataset a valuable one to study the important effects of medium anisotropy on shear-wave propagation.

(2) Our processing technique has succeeded to decouple the shear-wave energy between the two orthogonal horizontal components. The consistent, cross-component (energy-minimized component) shear-wave phase with wavelength similar to that in the main component (component on which the predominant energy has been focused) and with energy gradually increasing with depth is possibly the split shear-wave phase.

(3) We observe that the predominant polarization direction of a vertically propagating shear wave changes clearly at certain depths. The polarization azimuths of the two alternate components of energy-decoupled shear waves from the two sources, determined mutually independently, maintain constantly a 90° separation between each other, while varying with depth. We have derived the magnitude of the vertical shear-wave birefringence with various scales of depth-averaging. A common, irrevocable trend in the depth distribution of shear-wave birefringence emerges. The degree of vertical birefringence can surely be quite high (>20%) at certain depth ranges of the soft subsoil. Up to 38～39 meters the polarization azimuth of S2X:Rot (and S1X:Rot too) aligned approximately N30°E possibly denotes the fast direction of the medium, and that of S1Y:Rot (and also S2Y:Rot) aligned about N60°W denotes the slow direction. But below 38～39 meter (and at least between 39 and 43 meters), there is a sharp change in the orientation of the medium symmetry. Here the S1Y:Rot (and S2Y:Rot) azimuth oriented about E-W is the possible fast direction, and the S2X:Rot (and S1X:Rot) azimuth oriented about N-S is the slow direction.

(4) We have had independent measurements of the soil characteristics, viz. detailed lithology, N-value (mechanical strength), age of deposition, fine-scale seismic velocities, and the distribution of average, in-situ, horizontal stress. We have also considered

the depositional features of the subsoil layers. A very important result of our investigation is that the observed vertical shear-wave birefringence (both in magnitude and direction) has a first-order correlation with the occurrence of sharp changes in certain features of the subsoil, and in particular, in depositional environment (i.e., riverine or not), age of deposition, and the average horizontal stress (and possibly the related change in hydraulic permeability in a porous medium). Changes in birefringence are found to be conspicuous between the diluvium (Pleistocene age) and the alluvium (mainly Holocene age) sediments, and also in buried river-bed gravel and loam deposits.

10 General discussion

10·1 On the cause of the observed shear-wave birefringence in shallow surface-formations.

We have presented so far the results of our individual field experiments. Based on the causal correlation of the observed shear-wave birefringence with various other rock-physical or soil-physical characteristics, in this section we shall synthesize briefly the possible mechanisms for the occurrence of the vertical shear-wave birefringence in shallow surface formations.

In hard, compact rocks the birefringence is caused by : (a) lithological structures like veins, bands, etc. as we have found in gneiss and granite rocks at the site of Field Experiment 1, (b) gross internal structures created by cracks, fractures, partings, etc. as we have observed in Field Experiment 1, as well as in shales and limestones at the site of Field Experiment 2, and (c) anisotropic underground stress, that is possibly present at the active tectonic setting of the site of our Field Experiment 1. In most cases, these factors work together and cause the effective anisotropy that we observe. For instance, for Field Experiment 1, the cracks, particularly those in gneiss, are clearly developed along the prominent lithologic structures; also in the shallower depths the orientation of one of the two principal polarization azimuths, as well as the crack orientation, match fairly well with the direction of the horizontal compressive stress associated with the motion of the adjacent strike-slip fault system. The observed vertical birefringence is possibly thus related to these various factors directly or indirectly. The direct factor that emerges as common for both the experiments that we have conducted in hard formations, is the gross internal structure. We have demonstrated that careful observation can potentially delineate the polarization anisotropy to the extent that it can be correlated to the distribution of the internal structures like cracks, etc. in a scale of even a few meters.

In soft subsoil formations, that are more commonly encountered in the shallowest part of the underground and that are more important in the engineering projects carried out in the flat terrains, the medium anisotropy has traditionally been neglected in all practical applications. But our experiments suggest that the degree of shear-wave birefringence can actually be significant at certain depth zones. We infer that the observed birefringence and its distribution in granular, soft soils are mainly caused by: (a) alignment of grains or pores under the influence of some external agent (during deposition or during compaction), (b) anisotropic horizontal stress, (c) the presence of microcracks in relatively consolidated sediments, and (d) difference in the characteristic depositional effects in different times. Many of these factors contribute in varying proportions to the occurrence of anisotropy at a given subsoil site. The importance of anisotropic horizontal stress in tectonically active zones has been emphasized by a few other researchers. However, based on our field observation, we conclude that the depositional environment can be another extremely important factor that can create significant anisotropy in soft, granular, subsoil media.

A sedimentary fabric or a stratum of aligned grains can indeed cause significant vertical birefringence. We envision a model in Figure 45 to illustrate a possible situation where the individual grains comprising a sedimentary layer can be oriented during deposition or reoriented

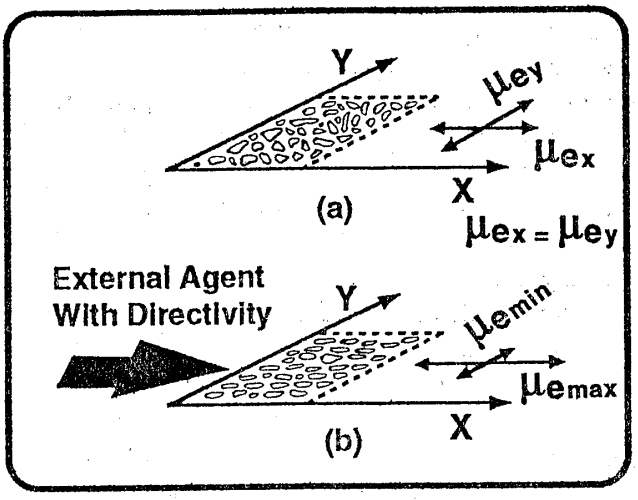

Figure 45. Field Experiment 4: Proposed model for anisotropic effective rigidity in the horizontal plane of a soft, sedimentary medium, induced by alignment of grains and/or pores under the influence of agents like wind, flowing water, moving glaciers, gravity, etc. Vertical shear-wave birefringence observed in such a medium will show correlation with the change in the environment of deposition, as we find true in our experiment.

afterward if they are subjected to an external agent that has a strong directivity. This external agent can be blowing wind, running water, percolating water/fluid, glaciers in motion, action of gravity or flow in gradient media, etc. whose effect is similar to the effect of directive stress. In course of time this may set up a preferential stiffness in one direction and a relative weakness in another direction, thereby making the medium measurably anisotropic. Nelson (1987) has reported that some eolian sandstones are azimuthally anisotropic due to a greater grain-to-grain strength in the downwind direction. Such anisotropy in sediments due to orientation of grains may occur even though the sediment might be under equal horizontal stresses and might have never been subiected to unequal horizontal stresses, as suggested also by Lynn (1991).

To interpret the consistent observation of higher vertical birefringence in the soft soil layers at the site of our Field Experiment 4, that are likely to have received more the effect of the ancient river flow, we stress on the possibility where a granular sedimentary medium can acquire significant stiffness in a given direction because of the reorientation of the grains under the influence of the external agent(s) possessing strong directivity.

10·2 Numerical verification of the plausibility of observing the vertical shear-wave birefringence in the scale of our experiment: the effects of varying medium stiffness on the synthetic seismograms for anisotropic media.

The results of the field experiments presented here have shown that anisotropy in near-surface formations can be significant in many cases. Field Experiments 1, 2 and 4 have illustrated that vertically propagating shear waves are notably sensitive to the existence of medium anisotropy.

In all experiments, the polarization direction of the leading shear wave has been found to be diagnostic of the local orientation of the symmetry of anisotropy. In a fractured hard rock (Experiment 1), we have noticed good correlation of the azimuth of the shear-wave polarization with the orientation of cracks, even in scale of a few meters. In a soft sandy subsoil (Experiment 4), we have observed a significant change in the shear-wave polarization direction

that is correlatable to the changes in age and environment of deposition, and also possibly to the change in subsurface stress state (viz. between Tokyo Formation and Edogawa Formation). In Experiment 2 also, changes in polarization direction are apparent when there are anticipatable changes in the distribution of internal structures of the rock strata (e.g., between Keokuk-Burlington limestone and the New Albany shales, or the Kankakee limestone). In Experiment 3, a lack of change in the depth distribution of shear wave polarization azimuth has been attributed to the relatively simple and constant depositional condition, age, internal structure, and stress regime in the soft sand/silt layers.

Compared to the polarization direction, the magnitude of the vertical shear-wave birefringence in near-surface formations is more difficult to ascertain stably and confidently because the propagation distance of shear waves involved in these experiments are too short for the fast and slow shear-wave phases to be identified with consistent accuracy. However, this does not imply that the magnitude of birefringence is small in the shallow subsurface; it rather points out our incapability to resolve the magnitude in the scale of our observations and under the constraint of scattered background noises and limited acquisition and processing abilities. It relates to the difference between what the reality is and what we can see in our restricted capacity. We have actually obtained strong indication in field data that the magnitude of the vertical shear-wave birefringence is often very high in the near-surface weathering layers (much higher than that found in deeper crust and mantle rocks); for instance, at certain depths in the fractured gneiss and granite rocks of Experiment 1 (Figure 17) or in the sandy subsoil layers of Experiment 4 (Figure 41), we have noticed the evidence of birefringence of about 20% or more.

What, however, counts in all practical applications is the real state of the underground and not the estimates that are inadequately made because of limitations in observation (including both acquisition and processing). If the degree of the stiffness contrast between two directions in a horizontal plane be significantly high at certain depths of the near-surface formations, as one may interpret based on our field-observed vertical shear-wave birefringence, this may have important bearing in geotechnical engineering. Recalling Figure 2, we see that a 20%～25% change in shear-wave velocity between two azimuths would imply a change of nearly 50%～70% of the effective rigidity, which is very large. It is therefore worthwhile to verify experimentally the relation between the stiffness variation in the horizontal plane and the observable change in the velocity of the horizontally polarized shear waves. We have carried out numerical experiments of shear-wave propagation in anisotropic media with varying medium stiffness.

The purpose of our forward modeling is two-fold. (1) We need to justify, in the short scale of our field experiments and using realistic medium properties, the observation of the phenomenon of shear-wave birefringence or splitting. We have observed the presence of minor cross-component energy after energy-decoupling for the dataset of Field Experiment 4, which we have interpreted as the split shear wave mode. It is necessary to check the validity of this interpretation. (2) For any realistic model of the near-surface medium, it is important to verify how a certain change of the stiffness in a given direction in the horizontal plane affects the velocity of a vertically propagating shear wave in the scale of our field experiments.

Figure 46 shows the model structure for which we have computed the synthetic seismograms. The surface shear-wave source is located at 2 meter distance from the borehole-mouth and 3-component seismograms are calculated betweeen 10 and 25 meter depths within the borehole at 1 meter interval. This geometry is very close to those in our actual field experiments The X and Y components of the geophone in borehole are oriented to radial (R) and transverse (T) directions, respectively. Though in our actual field experiments, the source motion is primarily SH (generated by planks placed at 90° from the radial direction), in numerical experiments, in addition to SH we have also considered the SV source radiation (that can be generated

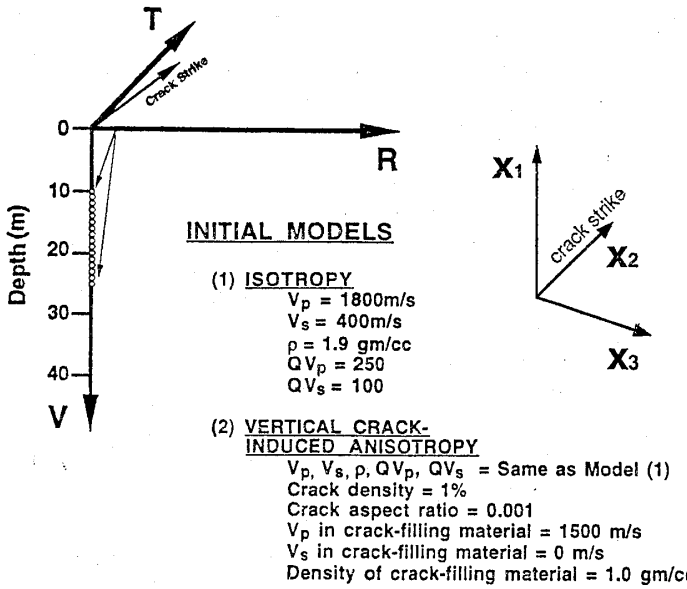

Figure 46. The initial models for numerical computation of the effects of anisotropy on the observed 3-component seismograms.

Table 3. Stiffness coefficients for isotropic and anisotropic models. Unit is 10^9 N/m^2. The coordinate system (R, T, V) is defined in Figure 46.

(a) Isotropic

6.156	5.548	5.548	0.000	0.000	0.000
	6.156	5.548	0.000	0.000	0.000
		6.156	0.000	0.000	0.000
			0.304	0.000	0.000
	[SYM]			0.304	0.000
					0.304

(b) Anisotropic(vertical cracks, 1%, T15° R)

6.154	5.549	5.547	0.000	0.000	-0.002
	6.154	5.547	0.000	0.000	0.002
		6.155	0.000	0.000	0.000
			0.304	0.001	0.000
	[SYM]			0.299	0.000
					0.299

by orienting the source in the radial direction). Our simple model has only one layer. The realistic medium properties assigned to our model are also illustrated in Figure 46.

To compute the complete waveform synthetic seismograms, we have used the algorithm of Mandal (1988). The algorithm extends the reflectivity method of Kennet (1983) and modified by Fryer and Frazer (1984) to general anisotropic media (up to 21 elastic constants), and uses the discrete numerical wavenumber integration technique (Bouchon and Aki, 1977; Mandal, 1988; Mandal and Toksöz, 1990). In this method, the computation is carried out in three steps. First, the steady-state wavefield radiation by the seismic source is represented as a superposition of waves propagating with discrete phase velocities. Second, each phase velocity component of the source wavefield is propagated through any stack of layer and the

contributions are summed for each wavenumber to transform the wavenumber domain to the space domain. Third, the final solution is obtained by Fourier transforming to the time domain and removing the unwanted effects of source periodicity and complex frequency. The final solution yields the complete wavefield for a particular source under consideration over a specified time length.

We have started with the initial isotropic model (Figure, 46), and have calculated the 3-component seismograms for SH and SV source radiations. Attenuation is introduced by specifying imaginary parts to the elastic constants (Crampin, 1981). In Table 3(a), the elastic coefficient matrix (C_{ijkl}) for the isotropic model is shown. The complete wavefield for the isotropic model is first computed. Then as a means to create anisotropy in stiffness in the horizontal plane, we introduce a small concentration of parallel vertical cracks striking in a given direction. It is to be emphasized here that our goal is not to examine numerically the effect of crack as such (for there are plenty of earlier studies doing that), but to assess the effect of anisotropic effective rigidity or stiffness on shear-wave propagation. As a first step to create this "weakness" in the medium along a given direction, we utilize the crack model. We introduce in the isotropic medium water-filled vertical cracks striking 15° radial of the transverse direction and having crack-density of only 1% and crack aspect ratio of 0.001. Thereby, the medium is made effectively anisotropic.

The anisotropic constants are derived from the theory developed by Hudson (1981), and calculated from the formulations summarized by Crampin (1984b). The usual method for calculating the anisotropy in shear-wave velocity caused by the presence of cracks and fractures is to derive the effective elastic moduli for the rock mass. In this method the additional compliance of a dilute population of fractures or cracks is incorporated into an average strain, resulting in effective moduli for the rock as a whole. The theory is valid for small aspect ratio of the cracks, which our model sufficiently satisfies. Table 3(b) illustrates the elastic coefficient matrix for the anisotropic model.

The computed seismograms (displacement) for our isotropic and anisotropic models are shown in Figure 47, for both SH and SV sources. Here, the medium response (0～80 Hz) has been convolved with a causal Hanning Ricker wavelet of 50 Hz center frequency. R and T correspond respectively to the responses in the X and Y components of the geophone. At first sight it is evident that some cross-component (i.e., R for SH source and T for SV source) energy appears, as the stiffness of the medium in the horizontal plane is made anisotropic by introducing the vertical water-filled cracks. This illustrates clearly the theoretical plausibility of the observation of shear-wave birefringence or splitting in the scale and for the field parameters of our actual field experiments. This (Figure 47(b)) also justifies our interpretation of the decoupled cross-component energy observed in Field Experiment 4 as the split shear-wave energy. As observed in decoupled field data, in synthetic seismograms we notice that the amplitude of the split shear-wave in R-component gradually increases with depth. The shear-wave phases in T and R components are respectively the fast- and the slow-split shear waves; however for such small degree of anisotropy and short propagation distance, it is not possible to distinguish easily the difference in phase velocity directly on the seismograms. We can relate here another important experience acquired on field data that, while polarization azimuths of split shear-waves can be derived stably in most cases, the magnitude of the velocity differences is a relatively difficult target. In Figure 47(b), the difference in phase velocity between the two horizontal components (which correspond to the velocity difference between the energy-decoupled X and Y components for our field datasets) is difficult to notice for the assigned frequency content and sampling rate. However since the split polarizations are widely separated from each other (90° here), it would not be difficult to decouple their energy by rotation, in case they are mixed (as we do in our energy-minimization scheme of processing).

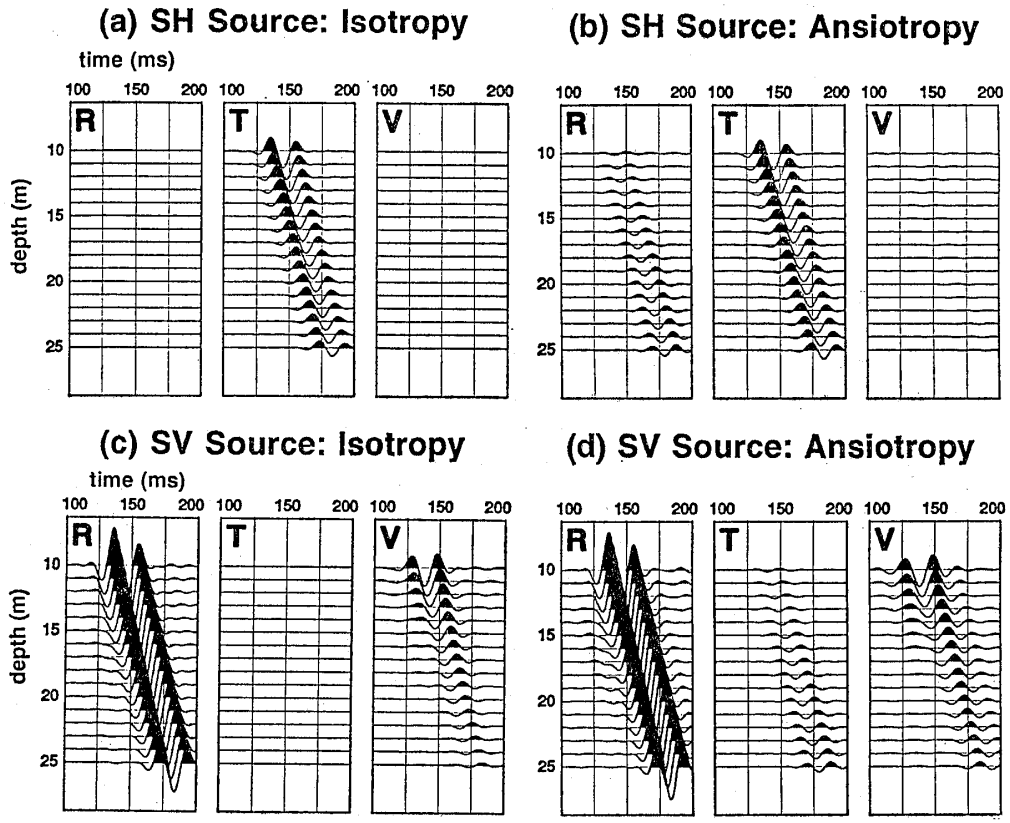

Figure 47. Synthetic seismograms for the near-offset (2 meter offset) VSP, with SH and SV sources. The realistic model parameters are described in Figure 46. The R and V components for the SH source and the T component for the SV source are enlarged 1.5 times relative to the rest, for better visibility. The effect of vertical birefringence is clear, as we find arrival of the split energy in the R component for SH source and T component for the SV source.

The second part of our numerical experiments is aimed at assessing the effect of variation of the magnitude of stiffness in a given direction in the horizontal plane on the velocity of a vertically propagating shear wave, in the scale of our field experiments. In our initial model we assign the directivity of the medium stiffness by introducing one set of parallel vertical cracks. We, therefore, use our above-mentioned crack model (Table 3(b), Figures 46 and 47(b)) as the starting model.

A single nonwelded fracture produces a discontinuity in the displacement field of a seismic wave, and the magnitude of this displacement discontinuity is related to the stiffness of the fracture (Schoenberg, 1980, 1983). The necessary assumption here is that fracture spacing is small relative to the seismic wavelength used. In such situations fractures can be represented by effective bulk material properties. Amadei and Goodman (1981), Schoenberg (1983), and others have shown that the bulk material properties of an otherwise elastic and isotropic rock mass containing a set of parallel fractures is equivalent to those of a transversely isotropic medium described by five independent elastic constants. Using an average strain method, they derived expressions for the five elastic constants in terms of the elastic properties of the intact rock, fracture spacing, and fracture specific stiffness. In a coordinate system (x_1, x_2, x_3), shown in Figure 46, where x_1, x_2 define the plane of the vertical cracks — x_1 being vertical and positive upward, x_2 being horizontal and oriented in the direction of the crack strike, and x_3 being horizontal and oriented across the cracks, these constants are given as:

$$C_{1212}=\mu,$$
$$C_{2323}=\mu/(1+E_T)=C_{1313},$$
$$C_{3333}=\mu/(\gamma+E_N),$$
$$C_{1111}=[1+4(1-\gamma)E_N]C_{3333}, \text{ and}$$
$$C_{1133}=(1-2\gamma)C_{3333},$$

where

$$E_T=\mu/(K_TH),$$
$$E_N=\mu/(K_NH), \text{ and}$$
$$\gamma=(1-2\nu)/[2(1-\nu)].$$

In these expressions, μ is the shear modulus, H is the fracture spacing, K_T and K_N are respectively the transverse and normal specific stiffnesses of the fractures, and ν is Poisson's ratio. The ratios E_T and E_N express the contribution of the fractures to the stiffness of the rock mass. Earlier experimental observations have shown that the fracture deformations are nonlinear function of stress and that the nonlinearity arises in part because of changes in the geometry of contact areas as stress on the fracture is increased. The specific stiffness of a facture under pseudostatic loading is the slope of the tangent to the stress-displacement curve; in other words, it is the ratio of the incremental stress across the fracture to the incremental displacement that the stress produces. As $K\to\infty$, $E\to 0$ and the values of the elastic constants become equal to those of an isotropic elastic medium defined by μ and ν. Hence velocities would be equal to those of a material containing no fractures.

We have experimented by assigning various values (within the theoretical limit) to the shear stiffness of the vertical cracks, which is equivalent to varying the effective rigidity of the medium in the horizontal plane in direction of the crack strike. Stiffness coefficients are derived in the (x_1, x_2, x_3) coordinate system, shown in Figure 46, in which the vertical cracks strike in the x_2 direction. We have then varied the value of the constant C_{1313} (= C_{2323}) between -0.5% and -5%, from a starting value that corresponds to an initial model of 1% crack (crack parameters being same as that shown in Figure 46). In Figure 48, the relation between percentage reduction of C_{1313} and that of the specific shear stiffness is shown. The relative changes are illustrated here; the solid line is for change relative to the 0.5% reduced value of C_{1313}, and the dashed line shows the variation of the rate of

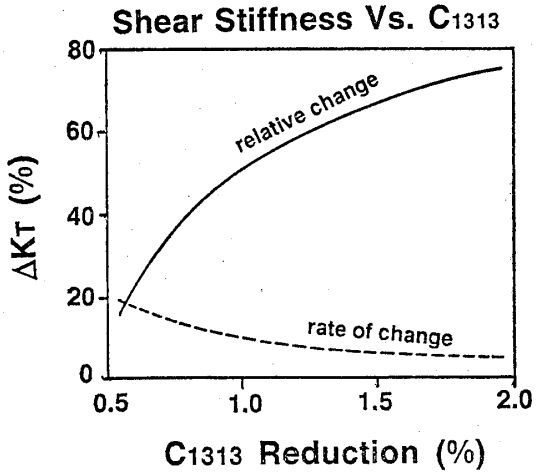

Figure 48. Specific shear stiffness of a medium due to aligned fractures (hence effective stiffness of the medium in the direction of the fracture) as a function of stiffness coefficient C_{1313}. Solid line shows the total change in shear stiffness relative to the value of 0.5% reduction of C_{1313} from the initial crack model. The dashed line shows the incremental change for every 0.1% reduction of C_{1313}.

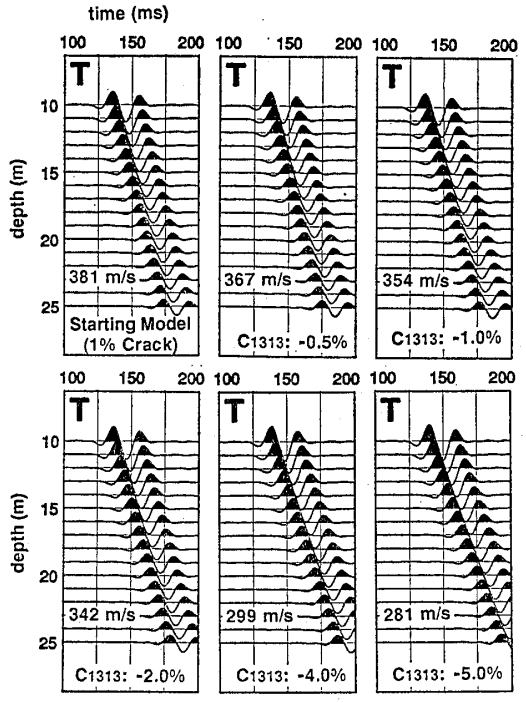

Figure 49. Transverse (T) component synthetic seismograms computed for various perturbations applied to the C_{1313} value of the starting anisotropy model. The gradual change in phase velocity is evident.

change.

In Figure 49, the calculated responses are shown for the transverse (T) component. Changes have been found in the radial component too. It is clear on the synthetic seismograms in Figure4 49 that a change in stiffness in the horizontal plane affects the phase-velocity of a vertically propagating shear wave. For instance, a decrease of C_{1313} by 2% will cause a relative decrease of shear-wave velocity observed in transverse component by over 10% (from about 381 m/sec to 342 m/sec), which is significant. We have not attempted here to show the expected difference in veloctity between the two shear waves polarized transverse and normal to the crack strike. As mentioned before, under realistic conditions (i.e., for short propagation distance and with the limited frequency and sampling rate available, as in our actual field experimemnts) the detectable difference in velocity due to change in effective stiffness is usually small. Admittedly, the large stiffness changes (e.g., the reduction of C_{1313} by over 2%) applied to the initial crack model in order to produce the clearly observable differences in velocity are too high; they have yet been used to illustrate the effects visually.

In reality, the effective rigidity in horizontal plane within the near-surface formations might indeed be highly anisotropic because of the superposition of a number of possible factors discussed earlier, e.g., aligned grains and pores in relatively soft sediments, craks/microcracks in relatively consolidated media, anisotropic horizontal stress, anisotropic hydraulic permeability, and other in-situ influences. Our numerical experiments demonstrate that such anisotropy can cause pronounced vertical shear-wave birefringence, with the polarization direction and the magnitude of the velocity difference varying with depth, thereby characterizing the distribution of anisotropy.

10·3 Implications of the observed shear-wave birefringence in near-surface formations for the engineering problems.

There are many anticipated benefits of treating the shallow subsurface anisotropic,

which it always is. Shear waves are particularly useful as they can sense the medium property not only along their propagation direction, but also across. The observation of significant shear-wave birefringence within near-surface formations and its meaningful distribution in depth, that we have reported in this paper, can have a number of important implications in civil engineering, geotechnical engineering, and earthquake engineering. We shall briefly define some of the fields/problems where the observed anisotropy in shallow surface-layers can bring immediate impact. We shall also present one concrete example where we have realistically assessed the effect of the field-observed vertical shear-wave birefringence on a problem of earthquake engineering.

(1) Measuring large-scale mechanical and hydraulic properties in hard rocks: For geotechnical engineers, especially for those who are involved in large underground constructions, such as underground power plants, fuel storage facilities, radioactive repositories, etc., measuring large-scale mechanical and hydraulic properties of the rock mass has been one of the major challenges. Our results have indicated that shear-wave birefringence, observed over relatively larger areas, can well be correlated to the hydraulic, mechanical or transport property of the rock mass, and hence can be utilized as a useful parameter for in-situ underground characterization.

(2) Monitoring crack or fracture distribution in hard rocks: The results of Field Experiment 1 have shown that it is possible to resolve on field-observed shear-wave seismograms the effects of crack distribution (particularly that of the crack orientation) in shallow ground-rocks, in a scale that is practical to the engineers involved in construction projects. In all important foundation engineering problems, e.g., in construction of dam, reservoir, bridge piers, tunnels, or high-rise buildings, monitoring the network of cracks or fractures in the basement rock comprises an important consideration. There are a few existing techniques to do this, e.g., high-resolution seismic tomography, electrical resistivity tomography, etc., but these methods quite often necessitate good contrast in physical properties at the interfaces of discontinuties within the rock, and involve high costs. Measuring systematically the shear-wave birefringence, using the available boreholes and efficient acquisition and processing systems as we have presented in this paper, can surely provide an additional, reliable means to achieve the goal.

(3) Better estimation of the V_S structure to charactrize the near-surface conditions, for both hard and soft media: The knowledge of shear-wave velocity itself in surface layers is indispensable in any engineering consideration. In particular for soft subsoils in flat lands, where most urban developments are concentrated, shear-wave data provide additional constraints on the state of compaction or strength of the formations. It is established that the mechanical strength of soil layers is much better related to V_S than V_P. For all these reasons, precision in shear-wave velocity measurements is imperative, and much efforts in hardware developments have so far been channeled toward this need. The reality of the phenomenon of shear-wave birefringence that we have reported in this paper, strongly suggests that to correctly describe the shear-wave velocity, it is essential to define the velocity variation caused by medium anisotropy. This would significantly reduce the scatter in the datasets and improve the interpretations based on V_S structure.

(4) Measuring the dynamic deformation characteristics of soil layers: Earlier investigations (e.g., Hardin and Drnevich, 1972; Yokota et al., 1981) on dependence of the dynamic deformation charactristics (e.g., shear modulus and damping constant) of soil on strain for various soil types and soil conditions (confining pressure, compaction, stress history, etc.) have assumed isotropic shear modulus. They have observed an unreasonably large scatter in the estimated value of the shear modulus for a given soil type. The clear observation of the vertical shear-wave birefringence in soft soil (Field Experiment 4) that we have reported in this paper

suggests that the effective shear modulus at a given depth for a vertically propagating shear wave may vary well, within the same horizontal plane. A consideration of the maximum and minimum values of in-situ, effective shear modulus anticipated from the velocity of the decoupled fast and slow shear waves, respectively, should provide a better evaluation of the deformation characteristics of the soil layers.

(5) Estimating in-situ, anisotropic horizontal stress in shallow depths: Evaluation of the stress distribution in surface formations is important in many engineering projects, particularly in those related to foundation or slope stability problems (construction of dams, tunnel, landslide preventive structures, etc.). There are various techniques to measure the subsurface stress distribution, many of which are based on measurements on cores or soils samples. However, the laboratory conditions generally differ widely from in-situ field conditions. Therefore, for any impotant engineering prospecting, particularly for those in soft soils, in-situ measurement of stress is considered very desirable. Though there are some means to measure the average value of the in-situ stress, there is no way to evaluate systematically by in-situ observation the nature of the anisotropic distribution of stress (e.g., direction of the maximum and minimum horizontal compressive stresses and the relative magnitude of their difference). The knowledge of horizontal stress anisotropy will provide significant insights on the lateral distortion charactristics of the subsoil. Careful and systematic observation of the vertical shear-wave birefringence in the shallow subsurface, as we have introduced in this paper, can provide a unique solution to this problem. It is now known that shear-wave birefringence is caused often by direct or indirect influence of in-situ, anisotropic horizontal stress. Lynn (1991) has related the magnitude of vertical shear-wave birefrignence observed in soft soil, to unequal horizontal stresses present in an active fault area. We have also noticed in a soft subsoil site (Field Experiment 4) that the observed variations of vertical birefringence correlate with the variations of the magnitude of in-situ, average horizontal stress measured independently, as well as with an enhanced hydraulic permeability. It has been marked also in almost all of our field experiments that often the fast and the slow directions are changed abruptly by almost 90°; if some of these observations are correct, they may reflect the contribution of a subtle change in the magnitude of the subsurface horizontal stresses (so that σ_H becomes σ_h, and vice versa). In general, the contribution of in-situ horizontal stress anisotropy on any field-observed shear-wave birefringence is yet to be satisfactorily resolved ; there are other questions to be answered too. Given all these inadequacies, the observation of vertical shear-wave birefringence can still serve as a unique tool available to date to assess the in-situ, anisotropic distribution of subsurface stress that is of great interest to the engineers.

(6) Calculating the site response for a future earthquake: It is well known that the ground behavior during an earthquake varies greatly depending on the nature of the ground. The ability to forecast the amplitude of the local ground motion (acceleration, velocity, or displacement) caused by an incident earthquake wave is essential for planning aseismic designs, as well as for assessing the liquefaction potential of a sandy soil. In order to reduce damage due to an impending earthquake, a careful consideration of the physical properties of the ground is thus very necessary. The distribution of shear-wave velocity in the shallow surface-layers constitutes one of the fundamental parameters that controls the magnitude of the ground motion. So far while computing the site responses, the shear-wave velocity structure in shallow subsurface has always been considered a unique function of depth. In other words, the dependence of shear-wave velocity on shear-wave polarization direction has not been known to or ignored by the engineers. However, as we have found in our field experiments, the near-surface may exhibit significant vertical shear-wave birefringence at some particular depths, which is attributable to a number of possible factors as disussed earlier.

We have calculated the effect of the observed vertical shear-wave bireringence on the routinely calculated site responses for earthquakes, for the site of our Field Experiment 4. The site of this experiment is located in a notably seismic region, and the possiblity of a large future earthquake is not too far-sighted. Figure 50 shows the two shear-wave velocity structures for this site that we have derived by analyzing the shear-wave birefringnce for the two sources independently (see Figure 40). Any shear wave arriving from below to the basement formation should split under the influence of the medium anisotropy, and the split phases should travel through the shallower layers with the different velocities shown in Figures 50(a) and 50(b). From surface to about 39 meter they (Figure 50(a) and Figure 50(b)) represent respectively the slow and the fast shear-wave velocity structures, but between 39 and 47 meters they become respectively the fast and the slow ones. The seismic basement is considered to be located here at a depth of around 75-80 meter. Between 5 and 47 meters depth we have approximate estimates for the vertical shear-wave birefringence. For other depths we know the shear-wave velocity from the suspension log, but we do not have any idea of the birefringence; so we have assumed these depths as isotropic (Figure 50).

In Figure 51, the result of our simple one-dimensional calculation of the surface acceleration is shown. At basement the input motion is same for the two different velocity structures (Figure 50); as the input we have used the true acceleration of a magnitude 6.7 earthquake observed within a borehole located very close to the present one. The standard computer code of "SHAKE" (Schnabel et al., 1972) has been used for response analysis. Figures 51(a) and 51(b) illustrate our computed accelerogams at surface for velocity strutures shown in Figures 50(a) and 50(b), respectively. The respective amplitude spectrum is also shown at the bottom. Figures 51(a′) and 51(b′) show our computed accelerograms at 39 meter depth for the same two velocity structurs.

To an earthquake engineer, the two most important targets are the calculated peak acceleration and the nature of the amplitude spectrum. Note in Figures 51(a) and 51(b) that the computed peak accelerations for the two contrasting velocity structures differ by over 10% (130.7 gal and 117.1 gal), which is significant. In amplitude spectrum too, we recognize a large change in acceleration in the next higher frequency phase (period about 0.5～0.6 sec). Because of the large change taking place at 39 meter, whose effects are included

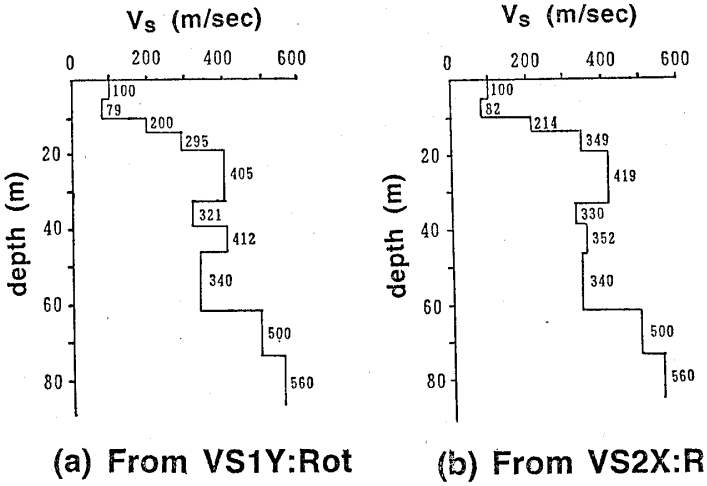

Figure 50. The two extreme velocity models obtained from field data (Field Experiment 4); they correspond to the velocities of propagation from seismic basement to surface for the two shear wave modes (fast and slow) incident from below. The depths where we do not have data (i.e., deeper than 47 meter and shallower than 5 meter) have been assumed isotropic.

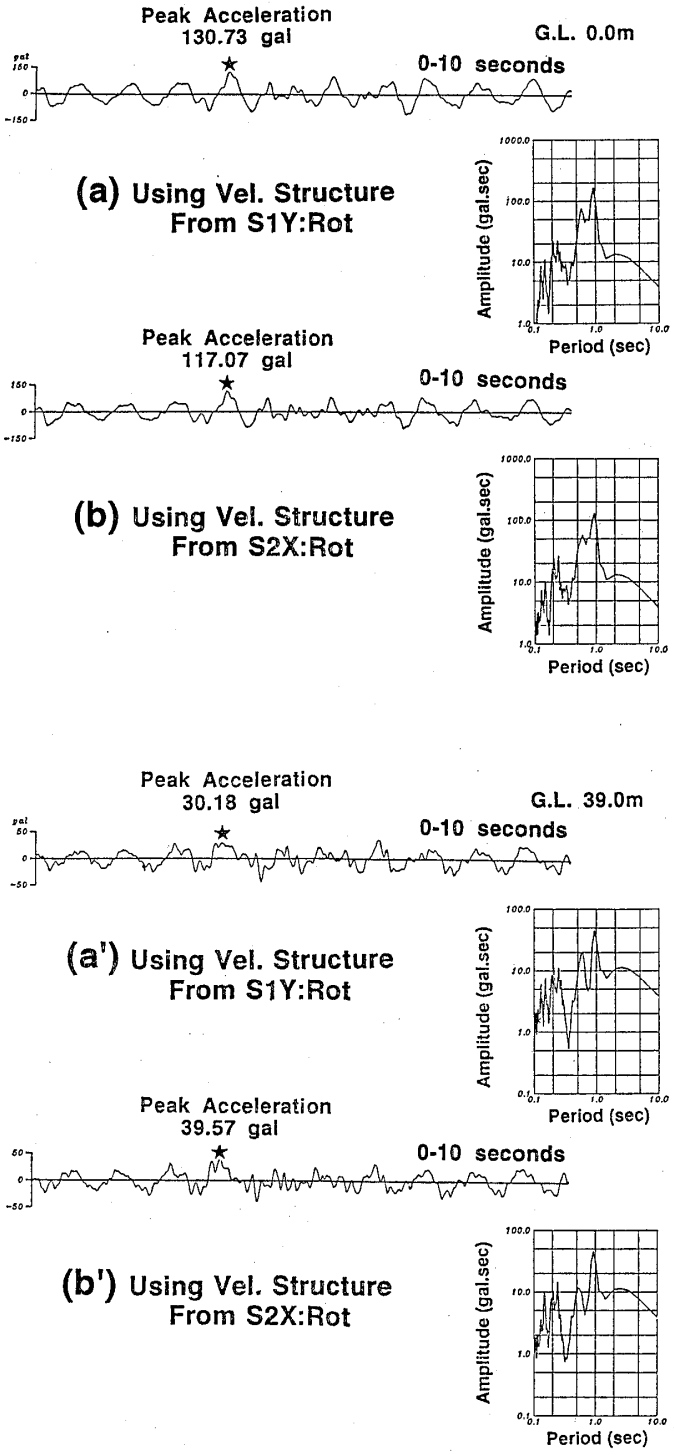

Figure 51. Computed site responses for the two velocity models (Figure 50) of the vertically birefringent near-surface. Computed accelerograms and the amplitude spectra are shown: (a) using velocity structure from S1Y:Rot and calculating the response at the surface, (b) using velocity structure from S2X:Rot and calculating the response at the surface, (a') using velocity structure from S1Y:Rot and calculating the response at 39 meter depth, and (b') using velocity structure from S2X:Rot and calculating the response at 39 meter depth. The input is same for all of them. The effects to compare between (a) and (b), and (a') and (b') are the peak acceleration and the nature of the amplitude spectrum; the differences are large for earthquake engineering considerations.

in the responses shown in Figure 51(a) and 51(b), we wanted to examine separately the effect of the velocity variation in the 39～47 meter zone alone, and to compare it with the total effect. The difference that we notice between the two calculated responses in Figures 51(a') and 51(b') is caused entirely by the large velocity difference in this 8 meter depth zone (between 39 and 47 meters) located at the boundary between Edogawa Formation and Tokyo Formation (Figure 36). The difference in the estimated response is clear both on accelerograms and amplitude spectra. It can be concluded that if a given shear-wave signal from an earthquake reaches the basement and then splits into two modes that travel vertically upward

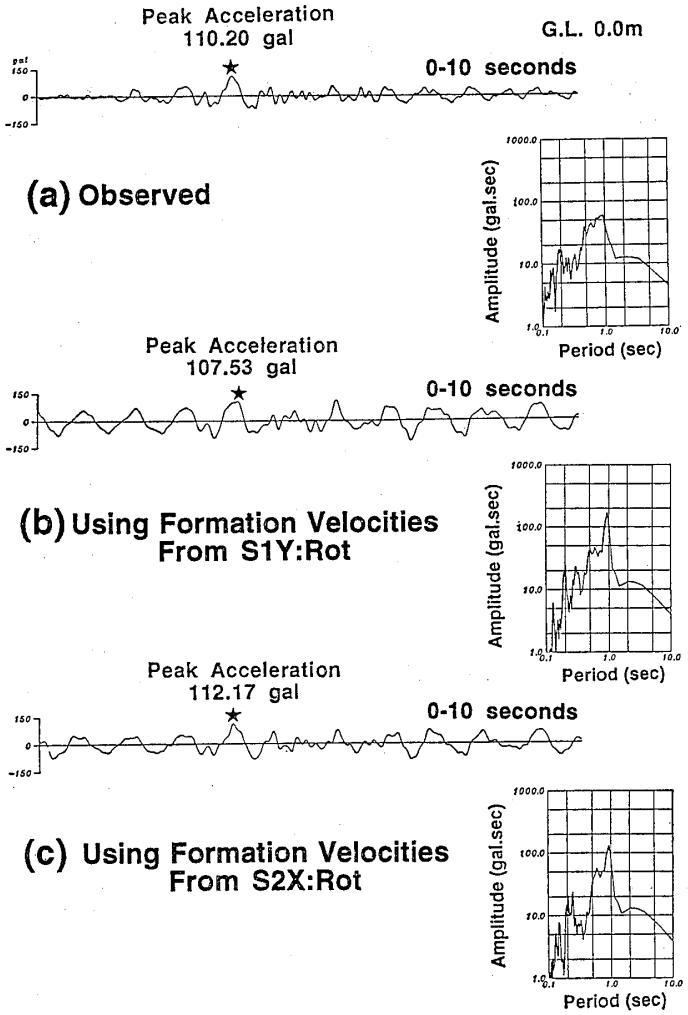

Figure 52. Comparison of the observed ground motion (a) with the computed responses ((b) and (c)) using the two velocity models that correspond to the velocities of propagation from seismic basement to surface for the two split shear-wave modes (fast and slow) incident from below. The input for the computed responses is the acceleration observed around 70 meter depth in the borehole. The low frequency noise arriving in the earlier part and also in the later part (portions out of the shear-wave window) of the synthetic accelerograms is verified to be due to neglecting the 2-dimensional structural effects of the subsurface. Notice that the observed peak acceleration lies between the two computed ones corresponding to the two extreme velocity models. Also mark that the shape of the computed frequency spectrum for S2X:Rot, which is the fast direction in the shallowest part of the near-surface medium, matches better with the observed frequency spectrum, suggesting a greater influence of the earlier arriving shear mode on the ground motion.

through the shallow surface layers with different velocities, then their individual responses at the surface would be quite different from each other. If we neglect the birefringence, computed response might be considerably different from the response of each of the two differing velocity structures for shear wave.

We compared the computed responses with an actual observation made in an adjacent borehole that has basically the same geology. In Figure 52, (a) is the observed accelerogram, and(b) and(c) are the responses at surface, computed after assigning anisotropic velocity to the subsoil layers as shown in Figures 50(a) and 50(b), respectively, We have checked through 2-D calculation here that the large amplitudes in the computed accelerograms visible before the peak shear-wave arrival (i.e., between 0 and 2 sec) and later are noises generated due to neglecting the lateral heterogeneity. At first sight, it is, however, apparent that the calculated response in Figure 52(c) matches somewhat better with the observation than the calculated response in Figure 52(b); the peak amplitudes are close, the immediately later parts of the waveforms (between 4 and 6 sec) are also more similar. The computed, peak spectral amplitudes are both not close to the observation, though for higher frequencies (period 0.1~0.4 sec) the response in Figure 52(c)is more similar to the observed one. The velocity distribution in Figure 52(c) corresponds to the fast velocity for the depth range from 39 meter to the surface, and we find a better matching between the response computed for it and the observed accelerogram. This suggests the possibility that the observed ground motion is affected more by the early-arriving fast-split shear wave than the later arriving one(s). More careful analysis using fast and slow velocity structures at various sites, as well as for various input motions, should define more clearly the effects of considering (or ignoring) the vertical shear-wave birefringence in near-surface formations on site-response calculations.

11 Conclusions and final remarks

We have attempted to present the important results of our field-oriented research on delineation of anisotropy in the near-surface formations and the shear-wave birefringence. Though shear-wave birefringence has invited significant attention of the earth scientists since early times, there are very few attempts so far to evaluate systematically the occurrence of birefringence in the very shallow wethering zone (i.e., within several tens of meters generally) that is of interest to the engineers. To provide the necessary information on the background research in this field, we have started with a brief review of some of the basic concepts on anisotropy and on the recent progresses made in the field of observation of shear-wave velocity anisotropy in various scales in the earth. We have then outlined the basic strategy of our own broad research, which comprises of development of hardwares and field acquisition technique, developing processing algorithm and interpreting the observations by incorporating other independent field-observed parameters, numerical computation of wavefield in anisotoropic media in the scale of our field observations, and evaluation of the important implications of the observed shear-wave birefringene for engineering problems. We summarize below the outcomes of research that have been discussed in this paper.

(1) We have developed efficient data acquisition systems for engineering prospecting of shear-wave birefringence in shallow surface formations. One primary tool for our field experiment is a specially designed sonde system, called "Borehole Shuttle", which is a multipurpose probe that can be clamped strongly against the borehole wall for receiving good-quality, high-frequency seismic waves. The sonde can work in narrow holes which is common in shallow, engineering surveys. The azimuth of the downhole receiver (orientation of the horizontal components) can be predetermined with the help of a magnetometer and a rotary unit. We have also employed high-resolution engineering seismographs for data recording.

(2) We have proposed a field acquisition technique for receiving high quality data. Shear waves have been generated by plank-hammering from two orthogonal sources placed near the borehole-mouth, and 3-component seismograms have been obtained at regular depth intervals within the borehole. During data reception the horizontal components of the geophones were oriented to constant azimuth at all depths. The data sampling rate used in our experiments varies between 50 and 500 μsec/sample. The interval of depth sampling in boreholes ranges between 0.5 and 4 meters.

(3) We have developed an efficient data processing algorithm to decouple the predominant shear-wave energy between the two horizontal components. The efficiency of this energy-minimization technique has been verified on VSP datasets. The algorithm does not necessitate a number of assumptions that are made in other existing techniques for processing shear-wave data, e.g., orthogonality between the two split shear waves, or invariance of the orientation of vertical birefringence within a given layer of considerable thickness, etc. Our results of processing show clear improvement in the shape of the waveform and better alignment of the phase arrival-time. From the rotations needed at each depth for decoupling the predominant energy between the two horizontal components, we can derive reliably the depth distribution of the polarization azimuth of the vertically propagating shear waves.

(4) We have presented in this paper the data and results of 4 different VSP experiments, carried out carefully at varying site conditions in Japan and the US, 2 each at hard rock site and at soft soil site. We have succeeded to identify clear effects of the medium anisotropy on field seismograms. In particular, two experiments (Field Experiments 1 and 4) have produced significant results showing clear expressions of anisotropy-induced birefringence or splitting on the shear-wave seismograms obtained in fractured, hard rocks and in soft, sandy soils.

(5) For the very short distances of propagation as in our experiments, and with the realistically achievable rates of data sampling and depth sampling, the depth distribution of polarization azimuth of the predominant shear-wave phases at various depths can generally be derived much more stably and much more accurately than the distribution of the magnitude of the velocity difference between the split shear-wave phases.

(6) In hard rocks, the derived polarization azimuth exhibits a clear variation in depth that is correlatable to the depth variation of the strike of the subvertical cracks, even in scales of a few meters. In soft subsoils, the deduced polarization azimuths often exhibit significant changes with depth, that can be correlated well with changes in depositional age, depositional environment, and in-situ stress. The independent results from two shear-wave sources confirm our observations.

(7) The magnitude of the birefringence is relatively difficult to observe and evaluate correctly. In hard fractured gneiss and granite, the birefringence can generally be about 10～15%. In soft subsoils we have obtained the very interesting result that the degree of birefringence can be very high (>20%) at certain depths, and this high birefringence is correlatable to sharp changes in the depositional sequence (age, environment, hydraulic permeability) and in-situ condition within the sediments.

(8) From correlation with other independent observations, we have interpreted our observed shear-wave birefringence in hard rocks (e.g., gneiss, granite, shale, limestone) by the presence of anisotropic internal structures (e.g., cracks, fractures, etc.). For soft subsoils, we have attributed the observed birefringence to the grain and pore texture related to depositional environment, age, and/or hydraulic permeability, as well as to anisotropic horizontal stress.

(9) The results of our numerical computation confirm that the vertical shear-wave birefringence should be visible even in the short scale of engineering explorations. The variation

of the effective rigidity or stiffness of the medium in the horizonal plane does affect the velocity of a vertically propagating shear wave. The high degree of vertical birefringence observed in field at certain locations in the shallow depths thus indicates considerable anisotropy in the horizontal plane in the effective rigidity or the shear modulus.

(10) The shear-wave birefringence that we have observed in shallow, underground formations has significant implications for the problems of engineering interest, which we have discussed. Six important problems have been identified, where the impact or use of the field-observed shear-wave birefringence is appreciable. They are, measuring large-scale mechanical and hydraulic properties, estimating the distribution of cracks and fractures in hard rocks, better estimating the shear-wave velocity structure in order to characterize the near-surface, evaluating the dynamic deformation characteristics of soft soil, anticipating the distribution of anisotropic horizontal stress in ground, and calculating the site response for an impending earthquake. Using the two different velocity structures for shear wave obtained by evaluating the vertical birefringence from actual field data, we have computed the seismic site responses; it is found that the effect of incorporating the birefringence is large.

We are convinced that anisotropy and anisotropy-induced vertical shear-wave birefringence are common occurrences in shallow, subsurface formations. They are surely important to the engineers. We predict the emergence of multiple new fields where the importance of treating the shallow underground as birefringent for shear wave would be seriously recognized. In addition, the observed birefringence can be used as a unique tool to determine various important subsurface information that cannot otherwise be easily obtained, e.g., in-situ stress anisotropy or in-situ fracture distribution. It is realized that the implications of the observed shear-wave birefringence are more significant for soft subsoils, where they have so far been ignored in all practical applications. There are, however, a number of improvements that are to be recommended for the future, e.g., availability of a more stable and more efficient hardware platform, particularly with high frequency sources (surface and downhole), both the source and the receiver placed at a few meter separation in the borehole within a common housing, higher rates for data sampling and depth sampling, etc. Secondly, we need to understand much better the mechanism of occurrence of the observed birefringence, as our interpretations cannot be significantly improved without this knowledge. We also need in-situ stress data in many fields, results of constrained physical modeling, examination of cores and soil samples to distinguish the contribution of internal structures and pore/grain texture, etc. Last but not the least, an increasing number of field measurements carried out under diverse and realistic conditions would greatly contribute to our understanding.

12 Acknowledgments

We thank Shimizu Corporation and Mitsui Mining & Smelting Co. Ltd. for allowing us to experiment at their work site and availing the core samples. We thank the Hydro Generation & Transmission Engineering Dept. of Tokyo Electric Power Co. for allowing us to work at their site and to use the strong motion data. Western Kentucky Petroleum is acknowledged for permitting us to use its field.

References

Alford, R. M. (1986): Shear data in the presence of azimuthal anisotropy: Dilley, Texas, Expanded Abstracts, 56th Ann. Int. Mtg. Soc. Expl. Geophys., 476~479.

Amadei, B. and Goodman, R. E. (1981): A 3-D constitutive relation for fractured rock masses, in Studies in Applied Mechanics, Part 5B, Mechanics for structured media: Elsevier International Symposium on the Mechanical Behavior of Structural Media,

Ottawa, 249～268.
Anderson, D. L., Minster, B. and Cole, D. (1974): The effect of oriened cracks on seismic velocities, J. Geophys. Res., 79, 4011～1015.
Anderson, D. L. and Dziewonski, A. M. (1982): Upper mantle anisotropy: Evidence from free oscillations, Geophys. J. R. Astron. Soc., 69, 383～404.
Anderson, D. L. and Regan, J. (1983): Upper mantle anisotropy and the oceanic lithosphere, Geophys. Res. Lett., 10, 841～844.
Ando, M. and Ishikawa, Y. (1982): Observations of shear wave velocity polarization anisotropy beneath Honshu, Japan: two masses with different polarizations in the upper mantle, J. Phys. Earth, 30, 191～192.
Ando, M., Ishikawa, Y. and Yamazaki, F. (1983): Shear wave polarization in the upper mantle beneath Honshu, Japan, J. Geophys. Res., 88, 5850～5864.
Ando, M. (1984) : ScS polarization anisotropy around the Pacific Ocean, J. Phys. Earth, 32, 179～196.
Ansel, V. and Nataf, H. C. (1989): Anisotropy beneath 9 stations of the GEOSCOPE broadband network as deduced from shear-wave splitting, Geophys. Res. Lett., 16, 409～412.
Atkinson, B. K. (1984): Subcritical crack growth in geological materials, J. Geophys. Res., 89, 4077～4114.
Auld, B. A. (1973): Acoustic fields and waves in solids, Volume 1: John Wiley and Sons, New York.
Bamford, D. (1977): P_n velocity anisotropy in a continental upper mantle, Gephys. J. R. Astron. Soc., 49, 29～48.
Bamford, D., Jentsch, M. and Prodehl, C. (1979): P_n anisotropy studies in northern Britain and the eastern and western United States, Geophys. J. R. Astron. Soc., 57, 397～429.
Battey, M. H. (1972): Minerology for students, Longman Group Limited.
Becker, D. F., Bishop, G. L., Clayton, K. N., Peterson, D. N., Rendleman, C. A. and Shah, P. M. (1990): Shear-wave anisotropy at Marcelina creek: SEG workshop: Vector Wave Field Seismology Update, San Francisco.
Beghoul, N. and Barazangi, M. (1990): Azimuthal anisotropy of velocity in the mantle lid beneath the Basin and Range Province, Nature, 348, 536～538.
Bhagavantam, S. (1966): Crystal symmetry and physical properties: Academic Press.
Bonner, B. (1974): Shear-wave birefringence in dilating granite, Geophys. Res. Lett., 1, 217～220.
Booth, D. C., Crampin, S., Evans, R. and Roberts, G. (1985): Shear-wave polarization near the North Anatolian Fault—I. Evidence for anisotropy-induced shear-wave splitting, Geophys. J. R. Astron. Soc., 83, 61～73.
Booth, D. C., Crampin, S., Lovell, J. H. and Chiu, J.-M. (1990): Temporal changes in shear wave splitting during an earthquake in Arkansas, J. Geophys. Res., 95, 11151～11164.
Bouchon, M. and Aki, K. (1977): Discrete wavenumber representation of seismic source wave fields, Bull. Seism. Soc. Am., 67, 259～277.
Bowman, J. R. and Ando, M. (1987): Shear-wave splitting in the upper mantle wedge above the Tonga subduction zone, Geophys. J. R. Astrom. Soc., 88, 25～41.
Brace, W. K. (1965): Relation of elastic properties of rocks to fabric, J. Geophys. Res.,7 0, 5657～5667.
Campden, D. A., Crampin, S., Majer, E. L. and McEvilly, T. V. (1990): Modelling the Geysers VSP: a progress report, The Leading Edge, 9, 36～39.

Christensen, N. I.(1984): The magnitude, symmetry and origin of upper mantle anisotropy based on fabric analyses of ultramafic tectonics, Geophys. J. R. Astron. Soc., 76, 89～112.

Christensen, N. I. and Ramananantoandro, R. (1971): Elastic moduli and anisotropy of dunite to 10 Kilobars, J. Geophys. Res., 76, 4404～4010.

Corrigan, D., Justice, M. G. and Neitzel, E. B. (1986): Estimate of shear-wave anisotropy using multicomponent seismic data, Expanded Abstracts, 56th Ann. Int. Mtg. Soc. Expl. Geophys., 389～391.

Cox, V. D., Rizer, W. D., Anno, P. D. and Queen, J. H. (1989): An integrated study of seismic anisotropy and the fracture system in the Spraberry Sandstone, Prembrook field, Upton and Reagen Counties, TX: SEG research workshop on recording and processing vector wave field data, Technical Abstracts, 65.

Crampin, S. (1978): Seismic wave propagation through a cracked solid: polarization as a possible dilatancy diagnostic, Geophys. J. R. Astron. Soc., 53, 467～496.

Crampin, S., Evans, R., Ucer, B., Doyle, M., Davis, J. P., Yegorkina, G. V. and Miller, A. (1980): Observations of dilatancy-induced polarization anomalies and earthquake prediction, Nature, 286, 874～877.

Crampin, S. (1981): A review of wave motion in anisotropic and cracked elastic-media, Wave Motion, 3, 343～391.

Crampin, S. (1984a): An introduction to wave propagation in anisotropic media, Geophys. J. R. Astron, Soc., 76, 17～28.

Crampin, S. (1984b): Effective elastic-constants for wave propagation in cracked solids, Geophys. J. R. Astron. Soc., 76, 135～145.

Crampin, S., Evans, R. and Atkinson, B. K. (1984): Earthquake prediction: A new physical basis, Geophys. J. R. Astron. Soc., 76, 147～156.

Crampin, S. (1987): Geological and industrial implications of extensive dilatancy anisotropy, Nature, 328, 491～496.

Crampin, S. (1990). Alignment of near-surface inclusions and appropriate crack geometries for geothermal hot-dry rock experiments, Geophys. Prosp., 38, 621～631.

Crampin, S., Booth, D. C., Evans, R., Peacock, S. and Fletcher. J. B. (1990). Changes in shear wave splitting at Anza near the time of the North Palm Springs earthquake, J. Geophys. Res., 95, 11197～11212.

Crampin, S. and Lovell, J. H. (1991): A decade of shear-wave splitting in the Earth's crust: what does it mean ? what use can we make of it ? and what should we do next?, Geophys. J. R. Astron. Soc., 107, 387～407.

Dale, T. N. (1923): The commercial granites of New England, I. U. S. Geol. Surv. Bull., 738, 1～97.

Dana, E. S. and Ford, W. E. (1947): A textbook of mineralogy, John Wiley and Sons, Now York.

Davis, T. L. and Lewis, C. (1990): Reservoir characterization by 3-D, 3-C seismic imaging, Silo field Wyoming, The Leading Edge, 9, 22～25.

Douglass, P. M. and Voight, B. (1969): Anisotropy of granites: A reflection of microscopic fabric, Geotechnique, 19, 376～398.

Estey, L. H. and Douglas, B. J. (1986): Upper mantle anisotropy: a preliminary model, J. Geophys. Res., 91, 11393～11406.

Evans, R. (1984): Effects of the free surface on shear wavetrains, Geophys. J. R. Astron. Soc, 76, 165～172.

Forsyth, D. W. (1975): The early structural evolution and anisotropy of the oceanic upper-mantle, Geophys. J. R. Astron. Soc., 43, 103～162.

Frasier, C. W. and Winterstein, D. F. (1986): Analysis of conventional and converted mode reflections at Putah Sink, California, using three component data, Expanded Abstracts, 56th Ann. Int. Mtg. Soc. Expl. Geophys., 396～400.
Fryer, G. J. and Frazer, L. N. (1984): Seismic waves in stratified anisotropy media, Geophys. J. R. Astron. Soc., 78, 691～710.
Fuchs, K. (1977): Seismic anisotropy of the subcrustal lithosphere as evidence for dynamical processes in the upper mantle, Geophys. J. R. Astron, Soc., 49, 167～179.
Fukao, Y. (1984): Evidence from core-reflected shear waves for anisotropy in the Earth's mantle, Nature, 309, 695～698.
Gledhill, K. R. (1990): A shear wave polarization study in the Wellington region, New Zealand, Geophys. Res. Lett., 17, 1319～1322.
Gledhill, K. R. (1991): Evidence for shallow and pervasive seismic anisotropy in the Wellington region, New Zealand, J. Geophys. Res., 96, 21503～21516.
Ghose, R. and Takahashi, T. (1991): Multiazimuthal seismic reception in borehole: Implications on field delineation of seismic anisotropy, Expanded Abstracts, 61st Ann. Int. Mtg. Soc. Expl. Geophys., 34～37.
Gueguen, Y. and Nicolas, A. (1980): Deformation of mantle rocks, Annu. Rev. Earth Planet Sci., 8, 119～144.
Gupta, I. N. (1973a): Seismic velocities in rock subjected to axial loading up to shear fracture, J. Geophys. Res., 78, 6936～6942.
Gupta, I. N. (1973b): Premonitory variations in S-wave velocity anisotropy before earthquakes in Nevada, Science, 182, 1129～1132.
Hardin, B. O. and Richart, F. E. Jr. (1963): Elastic wave velocities in granular soils: Journal of the Soil Mechanics and Foundation Division, Proc. Am. Soc. Civ. Eng., 89, SM1, 33～65.
Hardin, B. O. and Drnevich, V. P. (1972): Shear modulus and damping in soil; design, equations and curves, Journal of the Soil Mechanics and Foundation Division, Proc. Am. Soc. Civ. Eng., 98, SM7, 667～692.
Helbig, K. (1956): Die Ausbreitung elasticher Wellen in anisotropen Medien: Geophys. Prosp., 4, 70～81.
Hess, H. H. (1964): Seismic anisotropy of the upper most mantle under oceans, Nature, 203, 629～631.
Hoenig, A. (1979): Elastic moduli of a non-randomly cracked body, Int. J. Solids Struct., 15, 137～154.
Hudson, J. A. (1981): Wave speeds and attenuation of elastic waves in material containing cracks, Geophys. J. R. Astron. Soc., 64, 133～150.
Imai, T. and Tonouchi, K. (1982): Correlation of N-value with S-wave velocity, Proc. of 2nd Europ. Sympo. on Penetration Testing, 67～72.
Johnston, D. H. (1986): Detection of fracture-induced velocity anisotropy, Expanded Abstracts, 56th Ann. Int. Mtg. Soc. Expl. Geophys., 464～466.
Jolly, R. N. (1956): Investigations of shear waves, Geophysics, 21, 905～938.
Kaneshima, S. and Ando, M. (1986): Shear-wave splitting above small earthquakes in the upper crust (in Japanese), Abstr. Seismol. Soc. Jpn., 2, 215.
Kaneshima, S., Ando, M. and Crampin, S. (1987): Shear-wave splitting above small earthquakes in the Kinki district of Japan, Phys. Earth Planet. Inter., 445, 45～58.
Kaneshima, S., Ando, N., and Kimura, S. (1988a): Evidence from shear-wave splitting for the restriction of seismic anisotropy to the upper crust, Nature, 335, 627～629.
Kaneshima, S., Ito, H. and Sugihara, M. (1988b): Shear-wave splitting observed above small earthquakes in a geothermal area of Japan, Geophys. J. R. Astron. Soc., 94,

339～411.

Kaneshima, S. and Ando, M. (1989): An analysis of split shear waves observed above crustal and uppermost mantle earthquakes beneath Shikoku, Japan: Implications in effective depth extent of seismic anisotropy, J. Geophys. Res., 94, 14077～14092.

Kaneshima, S., Maeda, N. and Ando, M. (1990); Evidence for the splitting of shear-waves from waveform and focal mechanism analyses, Phys. Earth Planet. Inter., 61, 238～252.

Kaneshima, S. (1990): Origin of crustal anisotropy: shear-wave splitting studies in Japan, J. Geophys. Res., 95, 11121～11133.

Kaneshima, S. and Silver, P. G. (1990): Shear-wave splitting of teleseismic S, ScS, and SKS waves, EOS Trans. AGU, 71, 1443.

Kaneshima, S. and Silver, P. G. (1992): A search for source side mantle anisotropy, Geophys. Res. Lett., 19, 1049～1052.

Karato, S-I. (1992): On the Lehmann discontinuity, Geophys. Res. Lett., 19, 2255～2258.

Keen, C. E. and Barrett, D. L. (1971): A measurement of seismic anisotropy in the northeast Pacific, Can. J. Earth Sci., 8, 1056～1076.

Kennett, B. L. N. (1983): Seismic wave propagation in stratified media, Cambridge University Press, Cambridge.

Kind, R., Kosarev, G. L., Makeyeva, L. I. and Vinnik, L. P. (1985): Observations of laterally inhomogeneous anisotropy in the continental lithosphere, Nature, 318, 358～361.

Kudo, Y., Hashimoto, K., Sano, O. and Nakagawa, K. (1987): Relation between physical anisotropy and microstructures of granitic rock in Japan, in Proc. 6th Congress Int. Soc. Rock Mech., Eds. G. Herget and S. Vongpaisal, 429～432, A. A. Balakema. Rotterdam, The Netherlands.

Leary, P. C., Crampin, S. and McEvilly, T. V. (1990): Seismic fracture anisotropy in the Earth's crust: An overview, J. Geophys. Res., 95, 11105～11114.

Lee, S. H. H., Stokoe, K. H. Ⅱ. and Roesset, J. M. (1986): Influence of stress state on small-strain body waves propagating along principal stress directions, Expanded Abstracts, 56th Ann. Int. Mtg. Soc. Expl. Geophys., 131～134.

Lefeuvre, F., Cliet, C. and Nicoletis, L. (1989) Shear-wave birefringence measurement and detection in the Paris basin, Expanded Abstracts, 59th Ann. Int. Mtg. Soc. Expl. Geophys., 786～790.

Lefeuvre, F., Turpening, R., Caravana, C., Born, A. and Nicoletis, L. (1993): Vertical open fractures and shear-wave velocities derived from VSPs, full waveform acoustic logs, and televiewer data, Geophysics, 58, 818～834.

Lewis, C. (1989): Three-dimensional multicomponent imaging of reservoir heterogeneity, Silo field, Wyoming, Ph. D. Thesis, Colorado School of Mines, T-3700.

Lewis, C., Davis, T. L. and Vuillermoz, C. (1991): Three-dimensional multicomponent imaging of reservoir heterogeneity, Silo field, Wyoming, Geophysics, 56, 2048～2056.

Li, X-Y and Crampin, S.(1993): Transform techniques for processing shear-wave anisotropy in four-component seismic data, Geophysics, 58, 240～256.

Liu, E., Crampin, S. and Queen, J. H. (1991): Fracture detection using crosshole surveys and reverse vertical seismic profiles at the Conoco Borehole Test Facility, Oklahoma, Geophys. J. Int., 107, 449～463.

Love, A. E. H. (1944): A treatise on the mathematical theory of elasticity, Dover Publications.

Lynn, H. B. and Thomsen, L. (1986): Reflection shear-wave data along the principal axis of azimuthal anisotropy, Expanded Abstracts, 56th Ann. Int. Mtg. Soc. Expl. Geophys.,

473～476.
Lynn, H. B. (1991): Field measurements of azimuthal anisotropy: First 60 meters, San Francisco Bay area, CA, and estimation of the horizontal stresses' ratio from VS1/VS2, Geophysics, 56, 822～832.
Majer, E. L., McEvilly T. V., Eastwood, F. S. and Myer, L. R. (1988): Fracture detection using P wave and S wave vertical seismic profiling at The Geyser, Geophysics, 53, 76～84.
Mandal, B. (1988): Computation of the complete wavefield in anisotropic media, Reservoir Delineation Consortium, ERL, MIT, 2-1-2-31.
Mandal, B. and Toksöz, M. N. (1990): Computation of complete waveforms in general anisotropic media－results from an explosion source in an anisotropic medium, Geophys. J. Int., 103, 33～45.
Martin, M. A. and Davis, T. L. (1987): Shear-wave birefringence: a new tool for evaluating fractured reservoirs, The Leading Edge, 6, No. 10, 22～28.
McKenzie, D. (1979): Finite deformation during fluid flow, Geophys. J. R. Astron. Soc., 58, 689～715.
Mikumo, T., Wada, H. and Koizumi, N. (1988): Seismotectonics of the Hida region, central Honshu, Japan, Tectonophysics, 147, 95～119.
Montagner, J. P. (1985): Seismic anisotropy of the Pacific inferred from long-period surface wave dispersion, Phys. Earth Planet. Inter., 38, 28～50.
Montagner, J. P. and Nataf. H. C. (1986): On the inversion of the azimuthal anisotropy of surface waves, J. Geophys. Res., 91, 511～520.
Montagner, J. P. and Tanimoto, T. (1990): Global anisotropy in the upper mantle inferred from the regionalization of phase velocities, J. Geophys. Res., 95, 4797～4819.
Mueller, M. C. (1991): Prediction of lateral variability in fracture intensity using multi-component shear-wave surface seismic as a precursor to horizontal drilling in the Austin Chalk, Geophy. J. Int., 107, 409～415.
Nataf, H. C., Nakanishi, I, and Anderson, D. L. (1984): Anisotropy and shear-velocity heterogeneities in the upper mantle, Geophys. Res. Lett., 11, 109～112.
Nataf, H. C., Nakanishi, I. and Anderson, D. L. (1986): Measurements of mantle wave velocities and inversion for lateral heterogeneities and anisotropy, Part Ⅲ, Inversion, J. Geophys. Res., 91, 7261～7307.
Naville, C. (1986): Detection of anisotropy using shear-wave splitting in VSP surveys: requirements and applications, Expanded Abstracts, 56th Ann. Int. Mtg. Soc. Expl. Geophys., 391～394.
Nelson, R. (1987): Distribution and character of fractures in sedimentary basins and their importance for hydrocarbon reservoirs, Expanded Abstracts, 57th Ann, Int. Mtg. Soc. Expl. Geophys., 854.
Newmann, F. (1885): Vorlesungen über die Theorie der Elasticitat, Leipzig.
Nicolas, A. and Christensen, N. I. (1987): Formation of anisotropy in upper mantle peridotites: a review, in Composition, Structure and Dynamics of the Lithosphere-Asthenosphere System, Geodyn. Ser., vol. 16, eds. K. Fuchs and C. Froidevaux, 11-123, AGU, Washington, D. C.
Nicolas, A. and Poirier, J. P. (1976): Crystalline plasticity and solid state flow in metamorphic rocks, John Wiley, New York.
Nicoletis, L., Client, C. and Lefeuvre, F. (1988): Shear-wave splitting measurements from multishot VSP data, Expanded Abstracts, 58th Ann. Int. Mtg. Soc. Expl. Geophys., 527～530.
Nishimura, C. E. and Forsyth, D. W. (1985): Anomalous Love-wave phase velocities in

the Pacific: sequential pure-path and spherical harmonic inversion, Geophys. J. R. Astron. Soc., 81, 389~407.

Nishimura, C. E. and Forsyth, D. W. (1988): Rayleigh wave phase velocities in the Pacific with implications for azimuthal anisotropy and lateral heterogeneities, Geophys. J. R. Astron. Soc., 94, 479~501.

Nishimura, C. E. and Forsyth, D. W. (1989): The anisotropic structure of the upper mantle in the Pacific, Geophys. J., 96, 203~229.

Nozawa, T., Kawata, K. and Kawai, K. (1975): Geology of the Hida-Furukawa district (in Japanese), Quadrangle Ser., Kanazawa (10) 43, Geol. Surv. Jpn., Tsukuba.

Nur, A. and Simmons, G. (1969): Stress-induced velocity anisotropy in rock, J. Geophys. Res., 74, 6667~6674.

Nur, A. (1971): Effects of stress on velocity anisotropy in rocks with cracks, J. Geophys. Res., 76, 2022~2034.

Nur, A. (1972): Dilatancy, pore fluids, and premonitory variations of t_s/t_p travel times, Bull. Seism. Soc. Am., 62, 1217~1222.

Nuttli, O. (1961): The effect of the Earth's surface on the S-wave particle motion, Bull. Seism. Soc. Am., 51, 237~246.

Ogura, K., Uchiyama, S., Ohhashi, T. and Saito, H. (1988): Study of continuous measurement of suspension P-S logging, Expanded Abstracts, 58th Ann. Int. Mtg. Soc. Expl. Geophys., 43~46.

Ogura, K., Ohhhashi, T. and Saito, H. (1989): Technique of multipurpose locking sonde in a small drill hole, Expanded Abstracts, 59th Ann, Int. Mtg. Soc. Expl. Geophys., 67~69.

Ohanian, V. and Beckham, W. E. (1992): Depth-variant fracture orientation for multicomponent VSP, Expanded Abstracts, 62nd Ann. Int. Mtg. Soc. Expl. Geophys., 177~180.

Ohhashi, T. and Ogura, K. (1991): The vibration characteristics of the clamping tool for 4~8 inch borehole (in Japanese), Expanded Abstracts, 84th Mtg. Soc. Expl. Geophys. Japan, 46~49.

Ohya, S., Taya, M. and Shichiku, M. (1980): Using pressure meter to measure earth pressure at rest and undrained shear strength (in Japanese with English abstract), Annual Rep., OYO Corp., 2, 87~105.

Postma, G. W. (1955): Wave propagation in a stratified medium, Geophysics, 20, 780~806.

Peacock, S., Crampin, S., Booth, D. C. and Fletcher, J. B. (1988): Shear-wave splitting in the Anza seismic gap, Southern California: temporal variations as possible precursors, J. Geophys. Res., 93, 3339~3356.

Peng, S. and Johnson, A. M. (1972): Crack growth and faulting in cylindrical specimens of Chelmsford granite, Int. J. Rock Mech. Min. Sci., 9, 37~86.

Plumb, W. J., Engelder, T. and Yale, D. (1984): Near-surface in situ stress, 3, Correlation with microcrack fabric within the New Hampshire granites, J. Geophys. Res., 89, 9350~9364.

Raitt, R. W., Shor., G. G., Francis, T. J. G. and Morris, G. B. (1969): Anisotropy of the Pacific upper mantle, J. Geophys. Res., 74, 3095~3109.

Redpath, B. B., Edwards, R. B., Hale, R. J. and Kintzer, F. C. (1982) Development of field techniques to measure damping values for near-surface rocks and soils, NSF grant PFR-7900192.

Redpath, B. B. and Lee, R. C. (1986): In-situ measurements of shear-wave attenuation at a strong-motion recording site: sponsored by the USGS Contract No. 14-08-001-21823. Prepared by URS/John A. Blume and Associates, Engineers, 150 Fourth St., San Francisco, CA 94103.

Regan, J. and Anderson, D. L. (1984): Anisotropic models of the upper mantle, Phys. Earth Planet. Inter., 35, 227～263.

Research Group for Active Faults, Japan (1980): Active faults in Japan, The University of Tokyo Press, Tokyo.

Ribe, N. M. (1989) A continuum theory for lattice preferred orientation, Geophys. J., 97, 199～207.

Ribe, N. M. (1992): On the relation between seismic anisotropy and finite strain, J. Geophys. Res., 97, 8737～8747.

Ribe, N. M. and Yu, Y. (1991): A theory for plastic deformation and textural evolution of olivine polycrystals, J. Geophys. Res., 96. 8325～8335.

Roberts, G. and Crampin, S. (1986): Shear-wave polarizations in a hot-dry rock geothermal reservoir: anisotropic effects of fractures, Int. J. Rock Mech. Min. Sci., 23, 291～302.

Roesler, S. K. (1979): Anisotropic shear modulus due to stress anisotropy, J. Geotech. Eng. Div., Proc. of the Am. Soc. Civ. Eng., 105, GT7 871880.

Sachpazi, M. and Hirn, A. (1991): Shear-wave anisotropy across the geothermal field of Milos, Aegean volcanic arc, Geophys. J. Int., 107, 673～685.

Saito, H., Takahashi, T., Imayoshi, T. and Sakashita, S. (1991): High resolution crosshole seismic tomography at the Buckhorn test facility in Illinois, USA, Expanded Abstracts, 53rd EAEG Meeting, Florence, Italy.

Sano, O., Kudo, Y., Mizuta, Y. and Nakagawa, K. (1988): Deformation and fracture process of granitic rocks as an anisotropic body (in Japanese with English abstract), Proc. Jap. Soc. Civ. Eng., 400, 179～188.

Savage, M. K., Shih, X. R., Meyer, R. P. and Aster, R. C. (1989): Shear-wave anisotropy of active tectonic regions via automated S-wave polarization analysis, Tectonophysics, 165, 279～292.

Savage, M. K., Peppin, W. A. and Vetter, U. R. (1990): Shear wave anisotropy and stress direction in and near Long Valley Caldera, California, 1979～1988, J. Geophys. Res., 95, 11165～11177.

Schnabel, P. B., Lysmer, J. and Seed, H. B. (1972): SHAKE — a computer program for earthquake response analysis of horizontally layered sites, Earthquake Engineering Research Center, Univ. of Calif., Berkeley, Report: EERC 72-12.

Schoenberg, M. (1980): Elastic wave behavior across linear slip interfaces, J. Acoust. Soc. Am., 68, 1516～1521.

Schoenberg, M. (1983): Reflection of elastic waves from periodically stratified media with interfacial slip, Geophys. Prosp., 31, 265～292.

Scholz, C. H., Sykes, L. R. and Aggarwal, Y. P. (1973): Earthquake prediction; A physical basis, Science, 181, 803～810.

Scholz, C. H. and Koczynski, T. A. (1979): Dilatancy ansiotropy and the response of rock to large cyclic loads, J. Geophys. Res., 84, 5525～5534.

Shanov, S. (1990): Tectonic stress fields in Northeast Bulgaria, Geologica Balcanica, 20.4, 37～47.

Shearer, P. M. and Orcutt, J. A. (1986): Compressional and shear wave anisotropy in the oceanic lithosphere — the Ngendei seismic refraction experiment, Geophys. J. R. Astron. Soc., 87, 967～1003.

Shih, X. R., Meyer, R. P. and Schneider, J. F. (1989): An automated analytical method to determine shear wave splitting, Tectonophysics, 165, 271～278.

Shih, X. R. and Meyer, R. P. (1990): Observations of shear wave splitting from natural events: South moat of Long Valley Caldera, California, June 29 to August 12, 1982,

J. Geophys. Res., 95, 11135~11142.
Shimamura, H. and Asada, T. (1983): Velocity anisotropy extending over the entire depth of the oceanic lithosphere, in Final Report of the International Geodynamics Program, Geodynamics Series (Working Group 1), ed. Hilde, T. W. C., AGU, Washington, D. C.
Shimamura, H. (1984): Anisotropy in the oceanic lithosphere in the Northwest Pacific basin, Geophys. J. R. Astron. Soc., 76, 253~260.
Silver, P. G. and Chan, W. W. (1988): Implications for continental structure and evolution from seismic anisotropy, Nature, 335, 34~39.
Silver, P. G. and Chan, W. W. (1991): Shear wave splitting and subcontinental mantle deformation, J. Geophys. Res., 96, 16429~16454.
Simmons, G. and Wang, H. (1971): Single crystal elastic constants and calculated aggregate properties, in Handbook, The MIT Press, Cambridge.
Sprunt, E. S. and Brace, W. F. (1974): Direct observation of microactivities in crystalline rocks, Int. J. Rock Mech. Min. Sci. Geomech. Abstr., 11, 139~150.
Squires, S. G., Kim, C. D. Y. and Kim, D. Y. (1989): Interpretation of total wave-field data over Lost Hills field, Kern County, California, Geophysics, 54, 1420~1429.
Takahashi, T., Saito, H. and Shima, H. (1991): Field study on geophysical imaging techniques at the Buckhorn test facility in Illinois, Expanded Abstracts, 61st Ann. Int. Mtg. Soc. Expl. Geophys., 460~463.
Tanimoto, T. and Anderson, D. L. (1985): Lateral heterogeneity and azimuthal anisotropy of the upper mantle: Love and Rayleigh waves 100~250s, J. Geophys. Res., 90, 1842~1858.
Thomsen, L. (1988): Reflection seismology over azimuthally anisotropy media, Geophysics, 53, 304~313.
Tilmann, S. E. and Bennet, H. F. (1973): Ultrasonic shear wave birefringence as a test of homogeneous elastic anisotropy, J. Geophys. Res., 78, 7623~7629.
Todd, T., Simmons, G. and Balridge, W. S. (1973): Acoustic double refraction in low-porosity rocks, Bull. Seism. Soc. Am., 63, 2007~2020.
Verma, R. K. (1960): Elasticity of some high density crystals, J. Geophys. Res., 65, 757~766.
Vetter, U. and Minster, J. B. (1981): P_n velocity anisotropy in southern California, Bull. Seism. Soc. Am., 71, 1511~1530.
Vinnik, L. P., Kosarev, G. L. and Makeyeva. L. I. (1984): Anizotropiya litosfery po nablyudeviyam voln SKS and SKKS, Dokl. Akad. Nauk USSR, 278, 1335~1339.
Vázquez-Contreras, A., Booth, D. C., Zuniga, F. R., Chesnokov, E., Crampin, S. and Meissner, R. (1993): Seismic anisotropy in the Guerrero Gap, Mexico: preliminary results, Geophys. Res. Lett., 20, 69~72.
Waterman, P. C. and Teutonico, L. J. (1957): Ultrasonic double refraction in single crystals, J. Appl. Phys., 28, 266~270.
White, J. E. and Sengbush, R. I. (1953): Velocity measurements in near-surface formations, Geophysics, 18, 54~69.
White, J. E. (1965): Seismic Wave: Radiation, Transmission and Attenuation, McGraw-Hill Inc., New York.
Willis, H. A., Rethford, G. L. and Bielanski, E. (1986): Azimuthal anisotropy; occurrence and effect on shear-wave data quality, Expanded Abstracts, 56th Ann. Int. Mtg. Soc. Expl. Geophys., 479~481.
Winterstein, D. F. (1990): Velocity anisotropy terminology for geophysicists, Geophysics, 55, 1070~1088.
Winterstein, D. F. and Meadows, M. A. (1991a): Shear-wave polarizations and subsurface

stress directions at Lost Hills field, Geophysics, 56, 1331～1348.
Winterstein, D. F. and Meadows, M. A. (1991b): Changes in shear-wave polarization azimuth with depth in Cymric and Railroad Gap oil fields, Geophysics, 56, 1349～1364.
Yamazaki et al. (1992): Focal mechanism analyses of aftershocks of the 1984 Western Nagano Prefecture Earthquake, J. Phys. Earth, 40, 327～341.
Yokota, K., Imai, T. and Konno, M. (1981): Dynamic deformation characteristics of soils determined by laboratory tests, Annual Rep. OYO Corp., 3, 13～37.
Zollo, A. and Bernard, P. (1989). S-wave polarization inversion of the 15 October 1979, 23: 19 Imperial Valley aftershock: evidence for anisotropy and a simple source mechanism, Geophys. Res. Lett., 16, 1047～1050.

浅部地盤構造における弾性異方性とS波のスプリッティング
—— VSP 法によるその検出と地盤工学問題へのアプローチ ——

ラナジット ゴーシュ・長田正樹

要 旨

本報文は，筆者らが行ってきた実験的研究の現段階までの結果をまとめたものである。この研究は，地盤を伝わるS波の特徴を詳しく調べることによって，浅部地盤構造の示す弾性異方性がS波の伝播に及ぼす影響を定量的に明らかにし，その結果から異方性の度合が評価できるとすれば，従来の調査手法では得られなかった地盤情報を引き出せるのではないかと考えたことから始めたものである。

異方性地盤中の地震波の伝播に関する地球物理学的研究は以前から行われていたが，地盤工学に関連する物理探査においては，従来，弾性異方性という考え方は，ほとんど取り上げられていなかった。したがって，まず，異方性と地震波伝播の概念と，その地球物理学的研究の現状を簡単に紹介する（2章および3章)。つぎに，筆者らの研究の進め方についての基本的な考え方とそれに関連した測定法（測定装置，測定手段など）および解析法について述べる（4～8章)。9章は，日本国内の3箇所およびアメリカ合衆国内の1箇所において行った野外実験の結果である。これらの実験箇所の地質は，変成岩，古生代の堆積岩および新生代の未固結土質地盤と異なる地盤であったが，顕著なS波スプリッティングが観測されることを示す。10章においては，これらの観測されたスプリッテリング現象の原因について若干の検討を行い，いくつかの重要で基本的な観測結果が，異方性を示す地盤モデルにおける理論地震記象によって，定性的に説明できることを示す。また，併せて，地盤工学のいくつかの問題に対して，異方性を示す地盤中を伝播する地震波の果たし得るであろう応用についても簡単に触れる。11章はまとめに当てられている。ここでは，地盤の弾性異方性と地震波の伝播の研究が緒についたばかりであり，実際的な利用については，今後の研究の蓄積に待つところが多いものの，技術的な可能性に富んだものであることが述べられる。

地震探査は，地盤を線形で等方的な弾性体として扱うことで，地盤工学の実際に対し有用な技術を提供してきた。一方，鉱物学や実験岩石力学の分野では，岩石の弾性定数が方向によって異なるという性質（弾性異方性）は，よく知られた事実である。もし，このような弾性異方性が，地盤中の地震波の伝播に影響を与えるほどの規模で存在するものであれば，地震波伝播に対する異方性の影響が観測され，その程度や原因についても検討できるようになると考えられる。理論的には，地震波伝播に

対する異方性の影響は，P波よりもS波に顕著である。等方完全弾性体を伝播するS波は，その偏波の方向にかかわらず（SH, SV ともに）同一の速度で伝わる。しかし，異方性媒質の場合，S波の偏波の方向によって，異なる速度を持つことになる。異方性を示す媒質の典型的な例は，扁平なクラックが，卓越した方向に整列している岩盤である。このとき，クラックの走行方向に振動するS波（S_{fast}）は，クラックの走行に直交する方向に振動するS波（S_{slow}）よりも，速く伝わることになる（S波のスプリッテリング：Shear-wave splitting, Shear-wave birefringence 図—1参照）。

このような地盤の異方性が地震波の伝播に与える影響については，かねてより理論的な研究が多くなされてきたが，近年の観測技術の進展に伴って，その検出例が相次いで報告され，現実に観測・解釈可能な現象として認められるようになった。特に，石油などの炭化水素資源を対象とする資源探査の分野では，異方性の程度が資源の埋存可能性を示す指標となるとの考えから，1980年代後半以降盛んに研究されるようになり，実際の探鉱に利用することが試みられている。しかしながら，異方性の影響が現われる程度は極めて微小であるので，探査のスケールの小さな地盤工学の分野では，その検出自体が困難と考えられ，研究例も極めて少なかった。

物理探査の特徴は，現象や対象に応じ，測定方法や解析方法を比較的自由に選択できる点にある。筆者らは，この特徴を生かし，異方性を示す地盤中のS波の伝播特性（S波異方性*），すなわち，‘スプリットしたS波の振動方向が，計測地の地質状況に応じて，深度方向にどのように変化するか’という点に着目した手法を提案する。

測定方法は，従来のPS 検層や浅層反射法での経験に基づいて，ボーリング孔近傍の地表で板叩き震源によりS波を発生させ，ボーリング孔内で直交3成分（上下動1成分，水平動2成分）の受振器で鉛直に伝わるS波波形を観測する，VSP 法（鉛直地震探査法；Vertical Seismic Profiling）を採用した。この方法においては，S波はほぼ水平面内で振動しており，S波異方性を検出するのに有利であるという利点がある。ここで採用した測定法が従来から行われている方法と異なる点は，互いに直交する2基の地表震源（S1震源とS2震源）を配置したこと，ならびに，孔内受振器としては，ゾンデの向きを内蔵の方位計によって監視しながら回転することができ，しかも，受振器をボーリング孔壁に強く圧着できる装置（ボアホールシャトルシステム）を採用したことである（図—4参照）。

この方法によれば，各測定深度毎に，受振器を移動・回転・固定し，そして起振するという手順を繰り返すことになる。毎回の測定（深度）毎に，その方位を一定に保持することによって，受振器の感度を一定に保つことができた（例えば，常に起振方向から45度の方向に受振器を向かせる）。収録波形例を図—11に示す。これらの記録から，S波の初動部分の卓越振動方向を，図—7に示すような流れに沿った波形の回転処理を行なって求めている。この解析法では，従来の解析法に含まれていた理論上の仮定条件を緩め，より現実に沿った解析ができるようになるとともに，結果として，スプリットした波形が抽出されることにより，波形自体および位相の並びが改善され，速度の決定精度も向上したといえる。もしも，記録上S波波形に異方性の影響が現われなければ，常に，卓越振動方向は一定（例えば45度）の方向を示すはずであるが，求められた振動方向が深度毎に有意で，かつ，系統的な変化を示す場合には，地盤の異方性の存在を強く支持する証拠となる。しかも，各深度毎の変化分は，その区間の地盤の影響を受けたものとなる（図—5参照）。したがって，深度方向の異方性の変化が評価できることになる。なお，一般には，S波異方性の程度は，2つの速度比（S_{fast}/S_{slow}）で評価されているが，地盤工学の分野では，地震波の伝播距離が短いために，特に S_{slow} の見積りに不確定さを免れることができない。したがって，この報文においては，ある深度区間の S_{fast} および S_{slow} それぞれの平均速度を求め，その差によってS波異方性の程度を推定することとした。

現場実験は，1989年から1993年にかけて，地質条件の異なる4地点で行われた。第1地点は，岐阜県北部の非常に硬質で緻密な変成岩から成る岩盤，第2地点は，アメリカ合衆国イリノイ州の小油田地帯に分布する古生代の堆積岩類，第3地点は，埼玉県南部の洪積世堆積層，第4地点は，東京都南部の沖積世軟弱地盤を対象にしたものである（測定諸元については，表—1に示す）。

---

*弾性異方性を示す媒質中をS波が伝わる際に，一般に，S波は2つの位相に分裂（Split）する。この分裂したS波位相を，それぞれ S_{fast} および S_{slow} とすれば，これらにはつぎのような性質がある。

(a) S_{fast} と S_{slow} は同じ方向に進行するが，互いに異なった振動方向を示す

(b) S_{fast} は S_{slow} よりも速く伝わる

このような異方性媒質中におけるS波の伝播特性を，S波異方性と呼ぶことにする。

第1地点は，岩盤のP波速度が約6 km/sec，S波速度が約3 km/secという極めて良質な片麻岩と花崗岩から成っている。この地点における実験結果としては，

(a) 約20%を越える速度異方性が見られること（図—17）

(b) 卓越偏波方向は深度方向に系統的な変化を示すこと（図—18）

(c) しかも卓越偏波方向は，図—8に見られるようなクラック・割れ目などの走行と極めて強い相関を示すこと（図—22）

(d) 片麻岩から花崗岩への岩相の変化（したがって割れ目系の方向も変化している）に伴って，その変化に応じて，卓越偏波方向も変化していること（図—10および図—22）

などが挙げられる。

第2地点は，氷河砕屑物の下位に古生代の石灰岩（ケオクク・バーリントン石灰岩），頁岩（ニューアルバニー層群），石灰岩（カンカキー層），頁岩（マコーケタ層群）が続く堆積盆地の一角に位置している（図—23および図—24）。ここでは，深度79mから139m（ケオクク・バーリントン石灰岩），162mから204m（ニューアルバニー層群およびカンカキー石灰岩）の二つの区間に分けて測定を行った。速度の異方性は概ね10%ないしはそれ以下であり，一連の実験の中では速度の異方性の程度は低いものとなっている。卓越振動方向に関しては，上部では南北方向に振動するS波がより速く到達し，下部ではその方向が東へ15度ないし30度回転した状態となっている（図—29）。なお，P波走時トモグラフィの結果でも，頁岩層において，P波速度に最大10%程度の異方性が存在することが指摘されている。

第3地点は，主に洪積世の砂とシルトの水平な互層から成っている。この地点においては，深度22mから32mの間に，N値が急激に低下しているゾーンが存在している。この区間はシルトと粘土の層であり，このように，物性値および土質が他の部分と異なっているにもかかわらず，S波の振動方向は顕著な深度変化を示さず，ほぼ一定であるという結果が得られた（図—34）。

第4地点においては，埋め立て地盤の下位に，軟弱な沖積層（有楽町層 Yuc），さらに下位に，洪積層（東京礫層 btg，砂質土を主体とする東京層 Toおよび江戸川層 Eds）が分布する（図—36）。この地点では，

(a) より速く伝わるS波（S_{fast}）の卓越振動方向は，ほぼ N30° Eとなっているが，深度39m以深の江戸川層（Eds）では，E—W方向へと回転している（図—44）

(b) 速度異方性は，深度12mから18mの範囲で特に大きく，20%以上になっている（図—42）

(c) 通常行われているPS検層で求められるS波速度は，S_{fast} と S_{slow} の両者の速度の中間的な値を示す

(d) 試験孔の近傍での孔内水平載荷試験（LLT）の結果は，東京礫層（btg）と江戸川層（Eds）において大きな初期応力値を示しており（図—43），堆積過程の環境およびそのメカニズムが，有楽町層（Yuc）や東京層群（To）と異なっていることを示している。この応力の分布傾向とS波異方性の変化傾向はよく対応する（図—45）

などの結果が得られた。

4つの実験結果のうち，特に第1地点と第4地点におけるS波異方性の現われ方は，その原因を考える上で重要である。片麻岩のような硬質で緻密な岩盤において，S波の振動方向がクラックなどの微小な構造の卓越方向と工学的スケールにおいてもよい相関を示す事実は，S波異方性の説明によく用いられるクラックモデルが，S波スプリッティングの主要な原因として採用されることの妥当性を示している。

図—46は，扁平率0.0001という鉛直で薄いクラックが，体積比にして1%だけ岩盤中に整列・分布している状況（震源方向から15度の方向に並ぶ）をモデル化したものであるが，筆者らの観測と同じような深度範囲（10～25m）における理論記象は，図—47に示すように，純粋にSH（SV）震源の場合でも，直交するSV（SH）成分に有意な信号が現われる。すなわち，クラックの走行方向にもエネルギーが配分されている（S波スプリッティングが起きている）ことを示している。

より軟弱な土質地盤では，原因を1つに特定することは困難であるが，堆積環境（河成／海成，粒度，地下水の流れ，水平応力）により土粒子や空隙の配列に方向性がある場合に，顕著なS波異方性を示すようになるものと考えられる。もしも，このような配列の方向性があるとすれば，巨視的な弾性定数にも方向による強弱があるはずである。

鉛直に伝播するS波の場合，弾性マトリックスのすべり成分 $C_{1313}(=C_{2323})$ をわずかに変化させると，有効剛性率は大きく変化することになる（図—48および表—3参照）。このような有効剛性率の変化の地震波伝播への影響は，理論波形に明らかである（図—49）。この例は，もし弾性定数の1つの成分が2%だけ減少すると（地盤

が弱くなると），S波の速度は10%以上減少することを示している。このような計算結果は，岩盤のみならず，第4地点のような軟弱な地盤においても，S波異方性が現われ得る理由を，定性的ではあるが，示唆している。

以上のような原因によってS波異方性が観測されるものとすれば，ここで提案した手法は，地盤工学の様々な問題に地震探査の面から新たな情報を提供する技術になる可能性がある。例えば，岩盤の割れ目の卓越方向とS波の偏波方向が対応することは，岩盤中の割れ目の問題（分布，モニタリング），あるいは透水性の問題にこの手法が適用できる可能性を示している。今回提案した測定・解析法は，従来のPS検層から求められる速度値の確からしさを高めると同時に，地盤が本来示すはずの速度値の幅（上限と下限）を与える。土質地盤における異方性は，地盤の変形問題や地震応答問題に新たな情報を提供することになる（地震応答解析への利用を試みた例を図—50～図—52に示す）。

筆者らは，本報文の中で，地盤工学の分野において，従来困難と考えられていたS波のスプリッティングという現象の検出が，実際に可能であること，また，この現象は，地質条件が異なる程度の差はあるとしても，一般的に観測可能な形で存在すること，しかもS波異方性の深度分布という考えは，実際の工学的問題へ有用な情報を提供できる可能性があること，などを示した。しかしながら，現状は，漸くS波異方性の持つ有用性に気が付いたという段階にあり，今後，更に実用的な技術として発展させるためには，多くの課題が残されていることも事実である。例えば，他の物理的・工学的諸量と対比した異方性の検出・解釈事例の蓄積が不可欠であることはもちろんのこと，そのほかに，より簡便に，かつ，高密度の計測をするための測定・解析システムの改良，より分解能と確度を高めるための高周波S波震源（地表・孔内）の開発，さらに，浅部地盤における異方性の原因についての基礎的かつ系統的な研究，などが必要であると考えられる。

本研究を実施するにあたって，実験地の提供をはじめとし，数々の便宜を計って頂いた三井金属鉱業株式会社，Western Kenturkey Petroleum，東京電力株式会社および清水建設株式会社の各位に感謝の意を表す次第である。